



저작자표시-비영리-변경금지 2.0 대한민국

이용자는 아래의 조건을 따르는 경우에 한하여 자유롭게

- 이 저작물을 복제, 배포, 전송, 전시, 공연 및 방송할 수 있습니다.

다음과 같은 조건을 따라야 합니다:



저작자표시. 귀하는 원저작자를 표시하여야 합니다.



비영리. 귀하는 이 저작물을 영리 목적으로 이용할 수 없습니다.



변경금지. 귀하는 이 저작물을 개작, 변형 또는 가공할 수 없습니다.

- 귀하는, 이 저작물의 재이용이나 배포의 경우, 이 저작물에 적용된 이용허락조건을 명확하게 나타내어야 합니다.
- 저작권자로부터 별도의 허가를 받으면 이러한 조건들은 적용되지 않습니다.

저작권법에 따른 이용자의 권리는 위의 내용에 의하여 영향을 받지 않습니다.

이것은 [이용허락규약\(Legal Code\)](#)을 이해하기 쉽게 요약한 것입니다.

[Disclaimer](#)

공학박사 학위논문

**Study on Chirality Evolution during  
Systematic Control of Seed-mediated  
Chiral Nanoparticle Synthesis**

용액 기반 카이랄 나노입자 합성법의 체계적  
조절을 통한 카이랄성 발현에 대한 연구

2021년 2월

서울대학교 대학원

재료공학부

조 남 현



# Study on Chirality Evolution during Systematic Control of Seed-mediated Chiral Nanoparticle Synthesis

지도 교수 남 기 태

이 논문을 공학박사 학위논문으로 제출함

2021년 2월

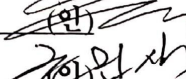
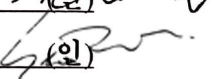
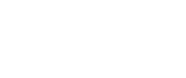
서울대학교 대학원

재료공학부

조 남 헌

조남헌의 박사 학위논문을 인준함

2021년 2월

위원장	_____	도준상	_____	(인) 
부위원장	_____	남기태	_____	(인) 
위원	_____	권민상	_____	(인) 
위원	_____	서지원	_____	(인) 
위원	_____	한정우	_____	(인) 



## **Abstract**

# **Study on Chirality Evolution during Systematic Control of Seed-mediated Chiral Nanoparticle Synthesis**

Nam Heon Cho

Department of Materials Science and Engineering

The Graduate School

Seoul National University

Control of chirality at nanoscale in inorganic materials holds much potential in scientific and engineering perspective. Chirality is a geometric property, mirror images of structure being non-superimposable to each other, is prevalently found in biological system. Manifesting this geometric property in inorganic metal nanomaterials could induce fascinating physical phenomena which was difficult to be found in symmetric nanomaterials. While there exists various method to construct chiral nanomaterials, aqueous seed-mediated synthesis of chiral nanoparticle holds significant advantages; i) facile large-scale production in environmental-friendly method, ii) nanoscale control of chiral features while possessing truly three-dimensional structures, and iii) strong chiroptic response at visible wavelength. In order to meet the demand of versatile potential applications of chiral nanomaterials, fundamental understanding of the seed-mediated based chiral nanomaterial synthesis and establishment of design

principle for expansion of synthesis method is crucial. The devised seed-mediated based chiral nanoparticle synthesis method utilizes the enantioselective interaction between chiral molecule and chiral metal surface. Through this research, we focus to understand underlying mechanism and influential factors of chirality evolution and conduct systematic enhancement of chiroptic response and synthetic principle for successful expansion of synthesis method has been established.

For optical applications of chiral nanomaterials, enhancing absolute chiroptical response intensity has significant merit. In order to enhance chiroptic response of synthesized chiral gold nanoparticle, 432 helicoid, it is crucial to understand and assess the full potential of current synthesis method. In this regard, quantitative assessment of synthetic quality of current synthesis system and nanoparticle has been conducted through single nanoparticle level dark field scattering analysis. While the current chiroptic response of 432 helicoid is exceptional among reported structures, the chiroptic response is currently observed by the solution ensemble stage, which is average chiroptic response of nanoparticles with morphology, size, and CPL irradiation angle variation. This average optical response could not fully represent the maximum potential of 432 helicoid nanoparticles and requires single nanoparticle level optical analysis. Single nanoparticle scattering analysis data was compared to solution based analysis and we were able to conclude that full potential of 432 helicoid chiroptic response is diminished by averaging of well-defined chiral nanoparticles and deformed nanoparticles. Therefore, we have learned that in order to selectively enhance chiroptic response of 432 helicoid, we need to improve the uniformity of chiral gold nanoparticle.

For systematic control of chirality evolution and to secure uniformity of synthesized nanoparticles, it is crucial to understand the kinetic parameter for chirality evolution and detailed growth mechanism. Kinetic parameter showed

how individual reagents involved in chiral nanoparticle synthesis influence the chirality evolution. Time-variant mechanistic study of 432 helicoid growth shows how the optical chirality and morphological chirality is evolved as reaction proceeds. In detailed, there exists two regimes of chiral growth, lateral growth regime and vertical growth regime. As each step promotes different type of chirality evolution, the required synthetic condition is clearly different. Therefore, instead of applying only initial control of chiral growth environment, we have systematically differentiated two growth steps with different synthetic conditions for uniform chirality evolution. This multi-chirality evolution step achieves higher uniformity of synthesized nanoparticle with enhance chiroptic response of 432 helicoid III. The origin of chiroptic response enhancement has been attributed to increase in chiral gap uniformity by quantitative morphology analysis and optical analysis.

For more general application of chiral nanomaterials, not limited to optical applications, versatility of possible chiral nanostructures and expansion of synthesis method to alternative material is crucial. In this regard, basic understanding for efficient and controlled expansion of devised aqueous seed-mediated chiral gold nanoparticle synthesis method has been established. Expansion of synthesis method has been conducted in two large directions: i) extension of chiral inducing biomolecule from amino-acid or short peptides to longer sequence programmable oligomer, ii) use of alternative material for non-plasmonic applications.

In the sense of programmable long oligomer for nanoparticle morphology control, DNA molecule has clear advantages. DNA nucleobase sequence could easily and economically be programmed and each programmed nucleobases of DNA has different interaction with gold surface. In order to find the effect of ssDNA oligomer on chirality evolution, thymine oligomer has been added to 432

helicoid II synthesis, conventionally using glutathione molecule as chirality inducer. Thymine oligomer assisted 432 helicoid II showed significant increase of chiroptic response while thymine itself did not induce any chirality evolution. Chirality evolution using only the ssDNA oligomer has also been tested and synthesis of chiral gold nanoparticle using Adenine sequence showed chirality evolution while other nucleobases did not show any chiral development. In order to understand this adenine specific chirality evolution, enantiospecific binding affinity of nucleobase and gold surface has been simulated. To understand how DNA sequence affect chirality evolution, sequence length and pattern has been altered to find the general rule of thumb for using ssDNA as chirality inducer.

For non-plasmonic applications of chiral nanomaterials such as catalysis or sensing, utilization different noble metal source during established synthesis method has been demonstrated. Due to the ease of direct application in current synthetic system, palladium has been used as the alternative metal source. Synthesized chiral palladium nanoparticles show spiral structures protruding outward on each six faces of cubic outer boundaries. Spiral structure's rotation direction is determined by the chirality of input cysteine molecule where chiral palladium nanoparticle showed increase in ratio of clockwise or counter-clockwise spiral structure depending on the chirality of cysteine molecule.

We believe this fundamental understanding of chirality evolution process during aqueous seed-mediated chiral nanoparticle synthesis method could become the ground-stone for more dynamic and unique chiral nanomaterials synthesis.

**Keywords: Chiral nanomaterials, Seed-mediated synthesis, Organic-inorganic chiral interaction, DNA nanoparticle, Nano-morphology control**

**Student Number: 2017-36204**

# Contents

<b>Chapter 1. Introduction .....</b>	<b>1</b>
1.1 Chirality in Nature .....	1
1.2 Importance of Chiral Nanostructures.....	8
1.3 Top-down Fabrication of Chiral Nanostructures.....	13
1.4 Chiral Assembly of Nanoparticles .....	16
1.5 Induced Chirality from Chiral Molecules .....	21
1.6 Bibliography .....	26
<b>Chapter 2. Aqueous based Seed-mediated Synthesis of Chiral Nanoparticle.....</b>	<b>38</b>
2.1 Surface Free Energy and Mechanistic Understanding of Shape-controlled Nanoparticle Synthesis.....	38
2.2 Capping Agent and Organic Additives .....	43
2.3 Reducing Agent and Its Interplay with Capping Agent...	49
2.4 Seed-mediated Synthesis of Shape Controlled Nanomaterials.....	53
2.5 Amino acid and Peptide Induced Chiral Nanoparticle ....	57
2.6 Objective of Thesis .....	62
2.7 Bibliography .....	66
<b>Chapter 3. Experimental Procedures.....</b>	<b>75</b>

3.1	Synthesis of Chiral gold Nanoparticles.....	75
3.2	DNA induced Chiral Gold Nanoparticle Synthesis .....	77
3.3	Chiral Palladium Nanoparticle Synthesis .....	78
3.4	Characterization of Chiral Nanostructures.....	79
3.5	Bibliography .....	81
<b>Chapter 4. Single-NP Dark-Field Scattering Analysis of 432 Helicoid Nanoparticles .....</b>		<b>83</b>
4.1	Introduction.....	83
4.2	Chiral Scatterometry Measurement .....	85
4.3	Comparison of Single-Nanoparticle Chiral Scatterometry Spectra with Ensemble Measurement .....	88
4.4	Matching of Scattering Spectra with Morphology.....	97
4.5	Conclusion.....	102
4.6	Bibliography .....	104
<b>Chapter 5. Multi-Chirality Evolution Step for Uniform Chiral Gap Structures.....</b>		<b>109</b>
5.1	Introduction.....	109
5.2	Effect of Synthetic Parameters on Chirality Evolution .	113
5.3	Time-Variant Analysis of Chirality Evolution.....	118
5.4	Multi-Chirality Evolution Step.....	121
5.5	Quantification of Synthetic Uniformity .....	125

5.6	Conclusion .....	129
5.7	Bibliography .....	130
<b>Chapter 6. Expansion of Chiral Inducing Agent...</b>		<b>134</b>
6.1	Introduction.....	134
6.2	Gold-DNA Surface Interaction.....	137
6.3	DNA directed Nanoparticle Synthesis .....	140
6.4	Effect of ssDNA Oligomer on Chirality Evolution during 432 Helicoid II Synthesis.....	143
6.5	Single-Stranded DNA induced Chiral Nanoparticle.....	146
6.6	Enantiospecific Interaction of Nucleobases and Gold Chiral Surface.....	150
6.7	Sequence Pattern Dependent Chirality Evolution .....	153
6.8	Surface Chemistry: CTAB vs Adenine .....	156
6.9	Conclusion .....	159
6.10	Bibliography.....	161
<b>Chapter 7. Expansion of Material Selection for Seed- mediated Chiral Nanoparticle Synthesis.....</b>		<b>169</b>
7.1	Introduction.....	169
7.2	Synthesis of Chiral Palladium Nanoparticle .....	171
7.3	Structural Analysis of Chiral Palladium Nanoparticle ..	174
7.4	Temporal Evolution of Chiral Palladium Nanoparticle .....	179

7.5	Conclusion.....	181
7.6	Bibliography .....	182
<b>Chapter 8.</b>	<b>Concluding Remarks.....</b>	<b>187</b>

# List of Figures

Figure 1. 1 Myo1D induced twisted larval body (left) and scheme of myo1D chiral activity across multiple organization scales (right).....	1
Figure 1. 2 Generation of sinistral and dextral <i>L. stagnalis</i> embryos and their adult snails.....	2
Figure 1. 3 Natural quartz crystals with left- and right-handed morphology.....	3
Figure 1. 4 The chiral atomic arrangement of the trigonal $\alpha$ -HgS crystal. ....	4
Figure 1. 5 SEM images of chiral calcite microcrystal precipitated in the presence of L- or D-tartaric acid. (Top Layer) SEM images of chiral vaterite microcrystal precipitated in the presence of L- or D-aspartic acid. (Bottom Layer) .....	6
Figure 1. 6 Schematic illustration plasmonic nanoparticles excited by the electric field of incident light with wave-vector. The collective movements of electrons are resonant at optical frequencies. ....	9
Figure 1. 7 Different optical properties of colloidal nanoparticles which covers a wide range of the electromagnetic spectrum depending on the material, dimension, and shape.....	10
Figure 1. 8 Schematic illustration plasmonic chiral nanodiscs excited by the circularly polarized light to show different energy state. This energy state induce absorption difference between two structures and this difference is circular dichroism .....	11
Figure 1. 9 Enantioselective binding of l- and d-cysteine on chiral Au(17 11	

9) <sup>S</sup> surface. The white arrows denote the N–C <sub>α</sub> vectors which pointed different orientations depending on the chirality of cysteine.....	12
Figure 1. 10 E-beam lithographed three-dimensional chiral oligomers. Scale bar of the overview is 500 nm and for the insets is 100 nm. ....	13
Figure 1. 11 SEM images of chiral unit cell composed of gold split-ring-resonators. Scale bars are 400 nm .....	14
Figure 1. 12 Top(left) and Side(right) view of gold-helix metamaterials fabricated by direct-laser writing. ....	15
Figure 1. 13 Gold nanorods oligomers twisted by cysteine. CD signal with nanorod scheme and TEM image shows change in spectra respect to twist angle. ....	16
Figure 1. 14 TEM images and model of chiral nanoparticle assemblies template via C18-(PEPAuM ox) <sub>2</sub> superstructures with helical ribbon geometry. ....	18
Figure 1. 15 Schematic models and TEM images of enantiomeric plasmonic pyramid assemblies. ....	19
Figure 1. 16 Left- and right-handed Au helices based on a DNA 24-helix bundle. Achiral gold nanoparticles are assembled around the bundle in a helical order to create chiral structures.....	20
Figure 1. 17 Chiroptic response of plasmonic nanoparticles conjugated with biomolecules a) Molecule induced chiroptic response of plasmonic gold island. ....	22

Figure 1. 18 helical peptide conjugated silver nanocubes and their CD signals ...	23
Figure 1. 19 Chiral configuration of atoms by chiral ligand-metal interaction a) Left- and Right-handed chiral Au <sub>38</sub> (SR) <sub>24</sub> cluster.....	24
Figure 1. 20 Two enantiomers of Au <sub>28</sub> (TBBT) <sub>20</sub> and its corresponding CD spectra. ....	25
Figure 2. 1 Low-index planes in a face-centered-cubic(fcc) metal and number of bonds per surface unit cell ( $N_B$ ) that have to be broken in creating a pair of new surfaces. The red dashed box represents the surface unit cell for each crystallographic plane.....	39
Figure 2. 2 Schematic illustration showing (a) two growth processes (b) total free energy plot depending on the structure .....	40
Figure 2. 3 Schematic image explaining the effect of capping agents on the surface energy and final nanoparticle morphology. ....	44
Figure 2. 4 Growth procedure of nanoparticles with morphology controlled by introduction of benzenethiol based modifiers.....	45
Figure 2. 5 Morphological characterization of the concave rhombicdodecahedron (RD). (a) large-area SEM image of the concave RD. (b-c) High- magnification SEM images of a single nanoparticle with models projecting along (b) [110] and (c) [111]. ....	47
Figure 2. 6 SEM images of gold nanoparticles with varying AA concentration from 0.3 mM to 4.4 mM of AA and fixing CTAB concentration at 15	

mM.....	50
Figure 2. 7 SEM micrographs of gold nanoparticles with varying the concentrations of CTAB and AA, ranging from 9 mM to 71 mM of AA and from 15 mM to 45 mM of CTAB.....	51
Figure 2. 8 Schematic of seed-mediated nanoparticle synthesis with deposition and diffusion kinetic control for nanoparticle exposed facet and morphology control.....	54
Figure 2. 9 Synthesis of high-index nanoparticles using low-index seed nanoparticles by reaction kinetic and surface stabilization control...	55
Figure 2. 10 Inorganic surface chirality of kink sites on high-index facets a) schematic surface chirality which chirality is determined by the rotation direction of their low-index components on the kink sites b) distribution of chiral high-index surface on {321} bound hexoctahedron nanoparticle.....	57
Figure 2. 11 a) Structure model of the observed hemifullerene-decorated steps along $[3\bar{3}4\bar{1}]$ and $[3\bar{3}4]$ when M enantiomers decorate R kinks, and P enantiomers decorate S kinks. b) and simulated enantioselective interaction on chiral gold surface which chiral molecule shows different orientation depending on the surface chirality.....	58
Figure 2. 12 Schematic diagram of chiral nanoparticle synthesis and chirality evolution through introduced chiral molecules.....	59
Figure 2. 13 Representative Scanning Electron Microscopy (SEM) images of chiral gold nanoparticles synthesized with L- and D- Cysteine.....	60

Figure 2. 14 Morphology library of 432 Helicoid Series synthesized with varying seed morphology and chiral inducing molecules. ....	61
Figure 2. 15 Comparison of dissymmetric factor among reported chiral nanomaterials and 432 Helicoid nanoparticles. <sup>42,46-53</sup> .....	61
Figure 4. 1 Schematic illustration of single chiral plasmonic NPs showing the left-handed, achiral, and right-handed structure and the optical transmission setup to measure single nanoparticle chiroptical responses. ....	85
Figure 4. 2 Representative SEM images showing four L-handed, achiral, and D-handed single chiral gold nanoparticle.(scale bar = 200nm) .....	87
Figure 4. 3 Scattering spectra of randomly picked single nanoparticles each column indicating L-handed, achiral, and D-handed nanoparticles. Collected spectra from LCP is indicated in solid line and RCP light illuminated spectra is indicated in dashed line. ....	88
Figure 4. 4 Differential scattering spectra of 3 x 26 sing nanoparticles in forward (solid line) and backward (dashed line) illumination directions. ....	91
Figure 4. 5 g-factor spectra for all 3 x 26 single nanoparticles. Top row shows differential scattering based g-factor graph while the bottom row indicate the averaged scattering based g-factor (left) and the absorption based g-factor measured in solution state. In both measurement technique, same batch synthesized chiral and achiral nanoparticles have been used.....	94

Figure 4. 6 Single nanoparticle g-factor spectra as well as the corresponding SEM images of six selected L-handed and D-handed nanoparticles. The SEM images are blurry as nanoparticle has been embedded in the liquid glass polymer layer for constant refractive index during the optical measurement. The top layer of polymer layer has been etched by the focused-ion-beam (FIB). (Scale bar = 200nm).....	97
Figure 4. 7 g-factor of total 26 single L-handed helicoid nanoparticles and some of the correlated SEM images.....	100
Figure 4. 8 g-factor of total 26 single D-handed helicoid nanoparticles and some of the correlated SEM images.....	101
Figure 5. 1 Schematic description of enhancement of chiroptic response through multi-chirality-evolution step in 432 helicoid III synthesis.....	112
Figure 5. 2 Dissymmetric factor diagram with respect to change in synthetic parameters during a conventional single chiral growth step of 432 helicoid III synthesis. The effective chirality evolution region is highlighted in pale pink. A) Change in dissymmetric factor with respect to change in reducing agent concentration and surfactant capping agent concentration. B) Change in dissymmetric factor with respect to change in Au precursor concentration and chiral peptide concentration. (scale bar = 100nm).....	113
Figure 5. 3 Extended chiral morphology diagram respect to change in Ascorbic acid and CTAB concentration during 432 helicoid III synthesis. ...	114

Figure 5. 4 Extended chiral morphology diagram respect to change in gold precursor and GSH concentration during 432 helicoid III synthesis .....	116
Figure 5. 5 Time-variant CD measurement of 432 helicoid III nanoparticle during its growth process. Chirality progressively increases with shift of resonance to larger wavelength. For this in-situ time-variant CD measurement, the synthesis was conducted in a quartz cuvette while time-interval CD measurement was conducted. The synthesis condition has been kept constant as conventional synthesis method.....	118
Figure 5. 6 Time-variant study of conventional single chirality evolution step 432 helicoid synthesis. A) Temporal change in dissymmetric factor of 432 helicoid III. Each recorded dissymmetric factor has been recorded with maximum g-factor intensity regardless of peak positions. Schematic description of the lateral growth and vertical growth directions from the {100} perspective. B) SEM images of temporal chiral structure evolution of 432 helicoid III. (Scale bar = 100nm)	119
Figure 5. 7 Schematic synthesis steps of devised multi-chirality-evolution step of 432 helicoid III. Steps are segmented to control the synthesis of chiral seed nanoparticle from octahedron seed nanoparticles, followed by uniform growth of 432 helicoid III from synthesized chiral seed nanoparticles.....	121
Figure 5. 8 Chiroptic response and SEM images of chiral seed nanoparticles. A) Chiroptic response of octahedral seed nanoparticles and intermediate chiral seed nanoparticles. B) Corresponding SEM images of octahedral seed nanoparticles chiral seed nanoparticles.....	122

Figure 5. 9 (a) Low-magnification SEM image of newly synthesized 432 helicoid III nanoparticles. (b) High-magnification SEM image of a 432 helicoid III nanoparticle. The representative chiral motif is well preserved with cubical outer boundaries. (c) Particle edge length distribution data of SEM image analysis..... 126

Figure 5. 10 Graphical modelling and size distributions of 432 helicoid III. a) Graphical modelling of 432 helicoid III with high uniformity viewed from direction. Geometrical parameters of chiral components in uniform 432 helicoid III model are indicated. Effective edge length distribution results of 100 particles synthesized via (b) single-step method and (c) multi-chirality-evolution step method..... 127

Figure 5. 11 g-Factor spectrum of previous single-step 432 helicoid III (black) and synthesized multi-chirality-evolution step 432 helicoid III (red). The fwhm of each spectrum is indicated with the doublesided arrow in respective spectrum colors..... 128

Figure 6. 1 Structures of DNA which contains Phosphate group, sugar group, and nitrogenous base group. Each nitrogenous bases are Adenine, Guanine, Cytosine, and Thymine which differs in its molecular structures. .... 135

Figure 6. 2 Comparison of the binding affinity of halide ions and nucleotides on gold nanoparticles. the measurement has been conducted through colorimetric and Raman assay. .... 137

Figure 6. 3 DNA conformation and surface density control by change in length of

anchoring block. Increase in the anchoring block induced lower density of DNA on gold nanoparticles. ....	138
Figure 6. 4 Morphology development ability of nucleotide oligomers for gold nanoparticles starting from spherical seed morphology. ....	140
Figure 6. 5 DNA nucleobases directed nanoparticle morphology control from low-index cubic nano-seed under co-reduction of gold and palladium. .	141
Figure 6. 6 DNA driven morphology control of concave cubic palladium seed nanoparticle. ....	142
Figure 6. 7 Experimental schematic of Thymine oligomer assisted 432 helicoid II synthesis method. ....	143
Figure 6. 8 Chiroptic response and corresponding SEM images of of 432 helicoid II, 432 helicoid II with T20 introduced, and nanoparticle synthesized using only T20mer. ....	144
Figure 6. 9 T20 oligomer insertion time control during 432 helicoid II nanoparticle synthesis. Depending on the insertion time, chiroptic response change has been changed. ....	145
Figure 6. 10 Chiroptic response of DNA induced chiral nanoparticle. G-factor diagram of a) Adenine-20mer induced nanoparticle, b) Cytosine-20mer induced nanoparticle, c) Thymine-20mer induced nanoparticle, and d) Guanine-20mer induced nanoparticles. ....	146
Figure 6. 11 SEM images of DNA induced chiral nanoparticles. a) low-magnification SEM images of nanoparticles showing uniform structures. b) High-magnification SEM images of DNA induced	

chiral nanoparticle with its chiral rotation highlighted with red dots and lines. c) schematic image of synthesized DNA induced chiral nanoparticle. ....	147
Figure 6. 12 Time-variant chiroptic response and morphology analysis of DNA induced chiral gold nanoparticle. ....	148
Figure 6. 13 DFT simulation of nucleobase interaction with chiral gold surface. a) generated chiral high-index gold surface, b) each nucleobase introduced to the unit cell of high-index chiral surface, and c) energy calculation upon introduction of nucleobase to unit cells. ....	150
Figure 6. 14 Interaction of chiral gold surface and Adenine respect to increase in number of Adenine. a) Energetically stable orientation of Adenine and b) schematic of hydrogen bonding formation between neighboring Adenine .....	151
Figure 6. 15 Energetically stable orientation and adsorption energy calculation respect to increase in nucleobase number introduced to the system in the case of a) Cytosine and b) Guanine .....	152
Figure 6. 16 Change in chiroptic response respect to change in Adenine oligomer sequence length. Peak 1 and Peak 2 notify each distinct chiroptic peaks while each arrows denote the tendency respect to increase in Adenine oligomer length. ....	153
Figure 6. 17 Change in sequence pattern of Adenine and Cytosine based 12-mer oligomer.....	154
Figure 6. 18 Chiroptic response diagram respect to CTAB and A50mer oligomer concentration during chiral nanoparticle synthesis. ....	156

Figure 6. 19 G-factor diagram of CTAB vs Adenine concentration during DNA induced chiral nanoparticle synthesis. Each red boxes indicate the highest g-factor regardless of peak positions at each CTAB concentrations. .... 157

Figure 7. 1 SEM images of palladium nanoparticle synthesized by pH control. pH was adjusted to 1.7 with acid and 4.5 using base, while no additive shows pH around 3.1. Ascorbic acid was controlled as High AA having 12 times higher concentrations than low AA. .... 171

Figure 7. 2 SEM image of chiral palladium nanoparticle controlled by cysteine molecule. As shown, the spiral chiral features show either clockwise or counter-clockwise rotation. The direction of rotation has been determined by the input chirality of the molecule introduced during the growth process. .... 174

Figure 7. 3 Change in morphology of chiral palladium nanoparticle synthesis respect to change in cysteine concentration in the growth solution. From images of a to f, increasing cysteine concentration was applied with c showing the optimum concentration of 1000 nM. .... 176

Figure 7. 4 Morphology diagram of CTAB vs cysteine concentration. The concentration range mentioned on each axis refers to the final concentration of each reagent. Besides surfactant concentration and the cysteine concentration, all other synthetic conditions have been kept constant. .... 178

Figure 7. 5 Time variant morphology analysis of chiral palladium synthesis. For

the statistical analysis, multiple nanoparticles have been analyzed and the average number of turns have been calculated to show progressive growth of chiral features..... 179



# Chapter 1. Introduction

## 1.1 Chirality in Nature

Nature has a very sophisticated but highly efficient strategy for the evolution of chirality, and understanding this is important for the successful control of chirality in artificial chiral metamaterial synthesis. May provide lessons learned. In biology, the complex process of chirality formation involves a combination of small molecular chirality, collectively exhibiting higher-order chirality.<sup>1-7</sup> In other words, the chiral center of the molecule can provide a macroscopic starting point for chirality generation as a single chiral molecule could function as a central component of chiral macromolecules. Therefore, chiral encoders of various length scales can be used to induce structural asymmetry in living organisms.<sup>8</sup> A distinctive example of this hierarchical chirality present in biology is the asymmetry of *Drosophila*, as shown in Figure 1.1.<sup>9</sup> Molecular motor myosin 1D produces overall chirality from the cellular level to organs and organism itself,

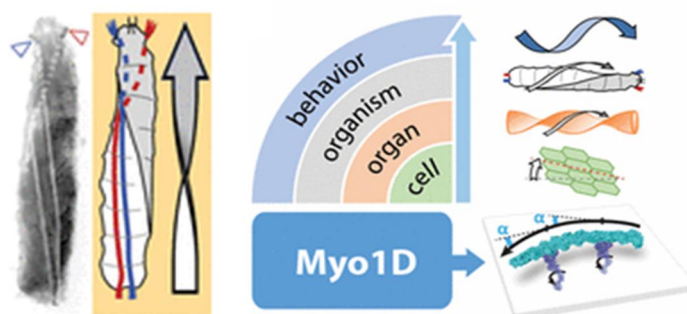


Figure 1. 1 Myo1D induced twisted larval body (left) and scheme of myo1D chiral activity across multiple organization scales (right).

eventually dictating the asymmetric behavior to demonstrate the gradual evolution of chirality in biology. The chiral interaction between myosin 1D and f-actin mediates a counterclockwise circular gliding of actin filaments, inducing a directional twist of cells, organelles, organisms as a whole, and even their behavior. Similar hierarchical chirality in nature is easily found in plant tendrils, exhibiting chirality from small sugar molecules to microfibrils and ultimately to macroscopic spiral structures.<sup>10</sup>

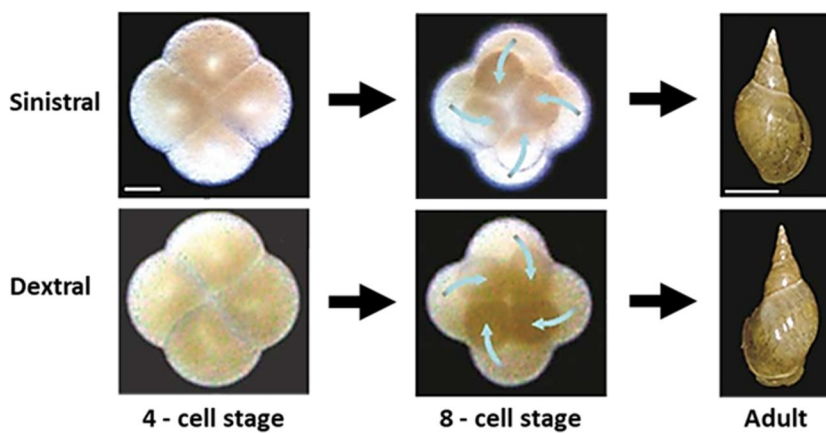


Figure 1. 2 Generation of sinistral and dextral *L. stagnalis* embryos and their adult snails.

This gradual manifestation of chirality in biological system can also be found in growth of shells of snails and gastropods from early embryonic stages.<sup>11,12</sup> Cytoskeletal structure growth of spindles are shown in figure 1.2.<sup>12</sup> The skeletal development stages from 4-cell to 8-cell shows the difference between being sinistral or dextral when a quartet of micromeres is formed. The handedness of adult snails is determined by this embryo stage directionality, which sinistral embryos show anticlockwise rotation of micromeres, dextral embryos show clockwise rotation. From these representative examples present in biological system, we could obtain valuable lessons. Firstly, systematical and hierarchical

assembly of chiral components could become macroscopic chirality. It indicates that basic components of biological systems such as organic molecules function as crucial building blocks for chiral structures in various size scales. Additionally, role of organic molecules or biomolecules is not limited to chiral building blocks but could provide a role as a chirality encoder during the development of chirality. This clearly shows that organic molecules and biomolecules can be utilized to induce progressive evolution of chirality.

### **Intrinsic chiral inorganics**

Most inorganic materials show high degree of structural symmetry, intrinsic chiral structures could be found in various scales.<sup>13-17</sup> Representative examples of the intrinsic chiral inorganics is the  $\alpha$ -quartz observed by Bragg in 1914.<sup>18</sup> The corner-linked SiO<sub>4</sub> tetrahedra of  $\alpha$ -quartz are arranged in a helical ordering along the c-axis and the structural configuration decides the handedness of crystal structure.<sup>18,19</sup> The three-dimensional chiral structure is constructed from chiral arrangements of quartz surfaces which the exposed faces serves as the chiral component. The (100), (101), and (011) faces of quartz surfaces are designated as

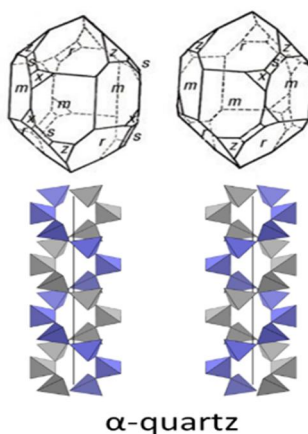


Figure 1. 3 Natural quartz crystals with left- and right-handed morphology.

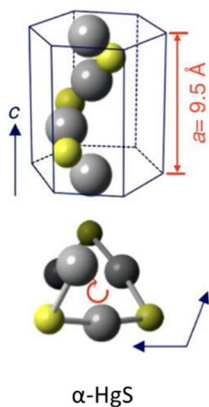


Figure 1. 4 The chiral atomic arrangement of the trigonal  $\alpha$  -HgS crystal.

m, r, and z in figure 1.3.<sup>20</sup> Part of the (111) and (511) faces, denoted as x and s, exist with (100), (101), and (011) faces surrounding to serve as the crucial aspect of left- and right- handed asymmetry formation.

Additional example of intrinsic chiral inorganic is cinnabar which is also known as mercury sulfide,  $\alpha$ -HgS. Cinnabar is often utilized to refine elemental mercury for various applications. Hexagonal unit cells of  $\alpha$ -HgS is shown in figure 1.4.<sup>21</sup> Along the c axis, Hg and S atoms are sequentially arranged to form long helical arrangement, while opposite chirality of  $\alpha$ -HgS possess opposite arrangement of Hg and S atoms. This spiral crystal structures of  $\alpha$ -HgS holds much similarities with that of quartz crystals that left- handed and right-handed forms are specifically constructed from helical atomic components orientations. Successful synthesis of chiral mercury sulfide from the achiral phase of mercury sulfide using opposite enantiomers of chiral penicillamine molecules was experimentally demonstrated by Markovich and co-workers<sup>22</sup> The chiral surfactant molecule used to induce chirality during the transformation of achiral phase mercury sulfide to chiral mercury sulfide demonstrated the viability of intrinsic crystal morphology control to chiral configurations for various enantioselective applications.

## **Chirality transfer from organic to inorganic**

Nature has already established a very efficient strategy for chirality evolution which could provide fundamental understanding for systematic control and generation of artificial chiral structures. Therefore, it is important to specifically understand the basic principle and examples of bio-molecule to inorganic chirality transfer.

In the process of bio-mineralization, many inorganic materials are formed in fairly well-controlled manners despite the complex chiral features in the biological system. Calcium carbonate ( $\text{CaCO}_3$ ) crystal is a representative case of an efficient and well controlled chirality transfer process. Surface chirality of calcite crystals known from various studies to serve a critical role in demonstrating organic molecule induced chirality transfer.<sup>3,16,17,23-27</sup> Various calcite crystal structures are previously reported from enantioselective interactions between chiral molecules and chiral calcite crystal surfaces. With the selective interaction with amino-acids and peptides and surface chirality, various three-dimensional structures of the calcite crystal have been reported. By selectively manipulating the interfacial energy between the chiral surface and the chiral molecule, various chirality transferred structures have been revealed. For example, with the introduction of L-tartaric acid, calcite grows in to the left-hand structure, but in the presence of the L-malic acid or L-aspartic acid, the right-hand structure are fabricated.<sup>24</sup> Furthermore, calcite crystal chirality has been modulated by the handedness of introduced chiral molecules during the precipitation process. When the both enantiomers of molecules such as, pure L- or D-tartaric acids exist in the environment during the precipitation process induce molecular chirality dependent directional growth of calcite crystals with mirror symmetry as shown in top layer

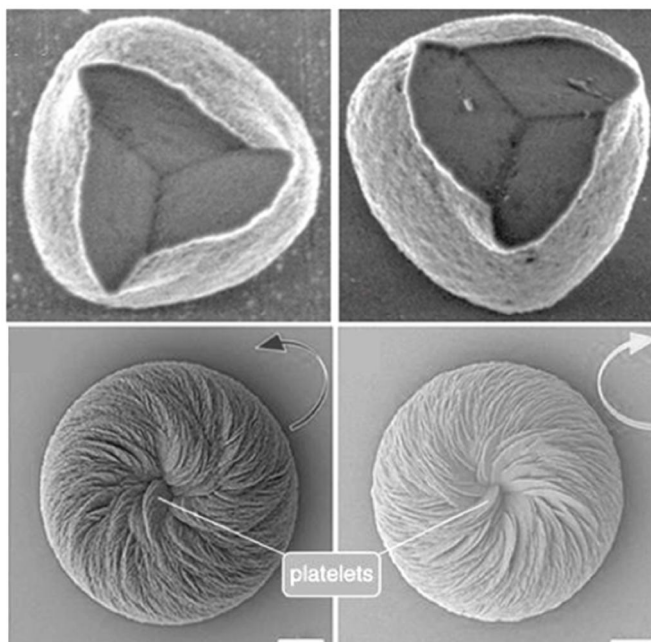


Figure 1. 5 SEM images of chiral calcite microcrystal precipitated in the presence of L- or D-tartaric acid. (Top Layer) SEM images of chiral vaterite microcrystal precipitated in the presence of L- or D-aspartic acid. (Bottom Layer)

of figure 1.5.<sup>24</sup> The final morphology of calcite crystals when tartaric acids are present is a seashell-shaped helical morphology. Input of opposite chirality of two enantiomers of the tartaric acids can induce opposite chiral crystals with mirror symmetry.

Additional example of chirality transfer between organic to inorganic material is vaterite. Vaterite is a polymorph of calcium carbonate which is known to form a hierarchically chiral structure induced by chiral biomolecules in biological systems.<sup>26</sup> Vaterite crystals, similar with the calcite crystals, possess surface chirality at specific enantiomorphic facets. Bottom layer of figure 5 shows the toroid vaterite crystals prepared with using L- and D-aspartic acid.<sup>27</sup> The chirality dependent interaction of the chiral vaterite surface with aspartic acid

induces an asymmetric growth of the crystal. This asymmetric growth induces the final asymmetric and chiral toroids structures. As a result, L-aspartic acid forms the clockwise rotation of CaCO<sub>3</sub> toroid, while the opposite handed molecule, D-aspartic acid, induces anti-clockwise rotating of CaCO<sub>3</sub> structures. These flexible and selective modulation of chirality in inorganic materials using chiral organic molecules indicate the further expansion of chirality control in other nanomaterials.

## 1.2 Importance of Chiral Nanostructures

As mentioned in the previous sections, the terminology of chirality is defined as a purely geometrical property referring to non-superimposable mirror images of an object with the original structure. This geometric property is not only limited to a certain area but it is prevalent in scientific fields such as chemistry, physics, astronomy and also in industrial sectors such as pharmaceutical, chemical, medicine, and display materials.<sup>25,28-32</sup> In the past few decades, the understanding and interest in chiral inorganic nanomaterials has been tremendously expanded its spectrum in terms of material, structure, and applications. Following section discuss some of the major field of chiral nanomaterials research and interest to emphasize the importance of chiral nanomaterials research.

Apart from the above mentioned geometrical properties, chirality can show some distinct physical properties, especially optical properties. We often observe that geometry of structures dictate the fundamental properties of materials. Symmetries are also one of fundamental geometric properties for a physical system as they strongly influence the electronic structures, crystallographic surface, chemical bonds, and optical responsivity. Among these, chiral structures are known to show different response to right- or left-handed circularly polarized light. (RCP and LCP) This chirality dependent light-matter interaction induce a different absorption of RCP and LCP light, which is called as circular dichroism (CD).

Using this selective absorption of RCP or LCP, it is possible to obtain the structural, kinetic, and thermodynamic information of macromolecules.<sup>33-35</sup> However, chiral optical response of most biomolecules or other naturally existing chiral medium generally show very weak optical response. It is possible to analyze the chirality by using high concentrations or large volumes of analyte but this adds

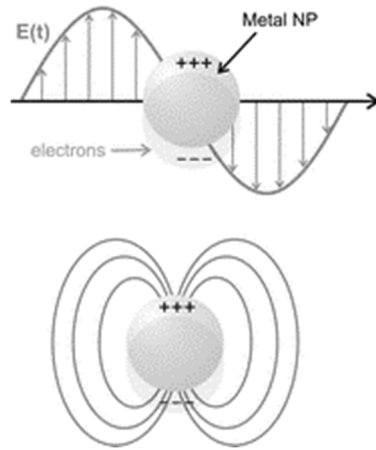


Figure 1. 6 Schematic illustration plasmonic nanoparticles excited by the electric field of incident light with wave-vector. The collective movements of electrons are resonant at optical frequencies.

complexity to many systems. In this context, utilizing plasmonic properties of metallic nanoparticles overcomes many of these issues. The plasmonic resonances of metallic particles are originated from a large number of quasi-free conduction electrons as shown in Figure 1.6. This harmonic oscillation of quasi-free electrons concentrates far-field radiation into subwavelength volumes which indicates extremely strong light-matter interaction at nano-scale plasmonic structures. This movement of electric field induced by electron density is strongly related with its structures and intrinsic material property as shown in figure 1.7.<sup>36</sup> Different shape and material induce different optical response which is shown in the color generation of nanoparticle solutions.

When this chiral plasmonic structures are introduced by circularly polarized light, chiral plasmonic nanostructures show chiral selective absorption, scattering or transmission properties. The reason is as shown in the schematic of figure 1.8.<sup>37</sup> As shown, the tip of the circular disc with open end shows different

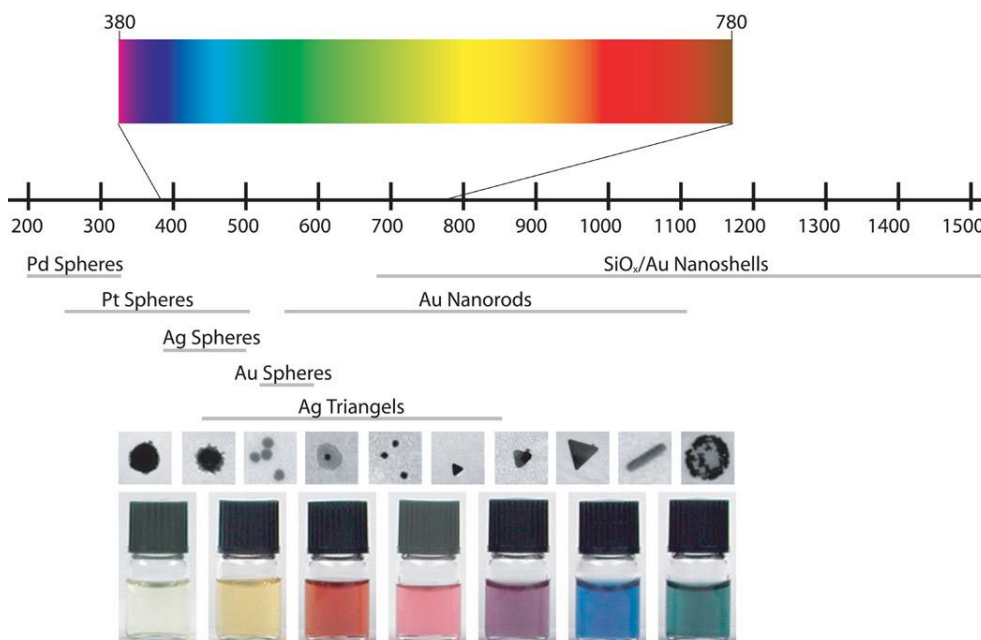


Figure 1. 7 Different optical properties of colloidal nanoparticles which covers a wide range of the electromagnetic spectrum depending on the material, dimension, and shape.

sign of polarized state respect to chirality of the structure upon the illumination of circularly polarized light. This sign of polarized state induces energy difference which is shown in the absorption spectrum as the circular dichroism. Considering that plasmonic structures show much stronger optical responses as stated above and could well be modulated by changing intrinsic chiral nanostructures or neighboring environment. For these reasons, chiral plasmonic structures are known to show wide usage with its enhanced optical response for applications such as polarization control, a negative refractive index, and chiral sensing.<sup>25,28–32</sup>

Aside from the plasmonic applications, chiral surfaces and chiral geometry existing in chiral nanomaterials could be utilized. Interest in chirality control is continuously growing in the chemistry and pharmaceutical industry. The

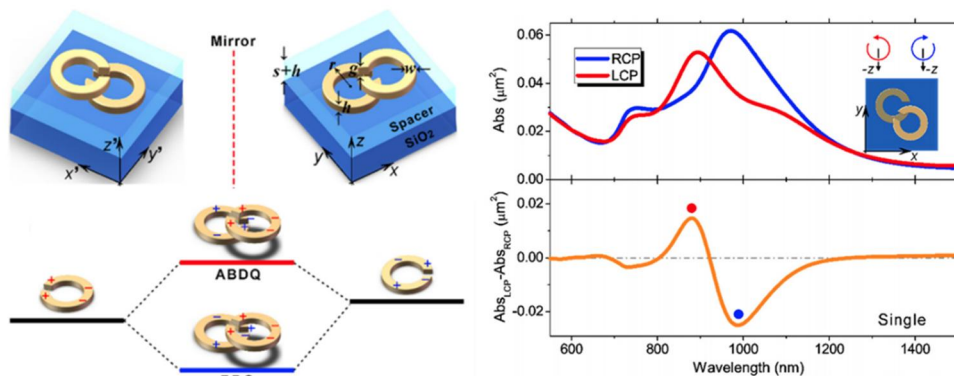


Figure 1. 8 Schematic illustration plasmonic chiral nanodiscs excited by the circularly polarized light to show different energy state. This energy state induces absorption difference between two structures and this difference is circular dichroism

reason for this requirement of chiral chemicals and drug is that living organisms are built from chiral molecules. As chiral molecules enter the biological system, enantiospecific interaction of chiral molecules and bio organisms bring about different results. For the simple example of this is *L*-limonene and *D*-limonene where respect to the chirality of the molecule, one molecule is perceived as lemon smell but the opposite chirality is perceived as orange smell. More severe example of this is the well-known case of thalidomide. Thalidomide has been used as the sleeping supplement for the pregnant women in 1960s. While the *R*-Thalidomide served the intended function as the drug, the *S*-Thalidomide in the racemic product caused birth defects to the born babies.<sup>38</sup> Therefore, selectively synthesizing pure enantiomers as the product is a significant issue in chemical and pharmaceutical industry. In this sense, chiral nanostructures could provide a well-established heterogeneous system. Chiral surface could be generated from the atomic level and many examples of enantioselective interaction between chiral atomic surfaces and chiral molecules with a representative example in figure 1.9.<sup>39</sup> These chirality

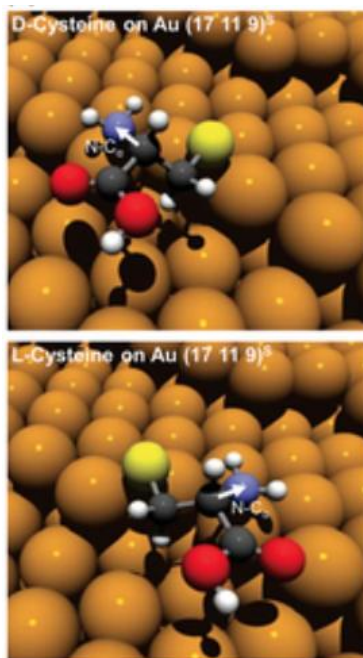


Figure 1. 9 Enantioselective binding of l- and d-cysteine on chiral Au(111)<sup>S</sup> surface. The white arrows denote the N–C<sub>α</sub> vectors which pointed different orientations depending on the chirality of cysteine

dependent interaction make difference in binding behavior between catalyst and molecule, which direction of catalytic reaction could be greatly altered with small energy difference or molecular orientation difference.

Introduced potential field of chiral nanomaterials application fields are greatly dependent on the generated chiral structures. Therefore, it is critical to understand general methods to construct these chiral nanomaterials. In the following section in the introduction chapter, we would like to elaborate some of the conventional chiral nanomaterials synthesis method.

### 1.3 Top-down Fabrication of Chiral Nanostructures

When considering possible methods to generate chiral nanostructures, it is possible to mainly categorize synthesis methods into two big streams of approach, top-down fabrication and bottom-up fabrication. With the significant improvement of nano-fabrication techniques such as direct laser writing and lithography, the top-down fabrication approach manifests very well organized and complex chiral nanostructures. Top-down synthesis of chiral nanostructures proceed with systematic and sequential nano-patterning which allows construction of chiral morphologies with various size and dimension scales.<sup>31,40-45</sup> Hentchshel and co-workers generated a three-dimensional chiral nanostructures using electron-beam lithography. Components of chiral structure was assembled by layer-by-layer stacking to make a chiral oligomer structures as shown in figure 1.10.<sup>41</sup> The first layer of nanostructure is an assembly of 3 nano-discs to form an L-shape and on the second layer, the fourth nano-disc is placed on top of one of the existing nano-disc to determine the handedness of the overall structure. Similarly, Decker and co-workers constructed a layer by chiral structure synthesized using electron beam lithography as shown in figure 1.11.<sup>43</sup> Sequential stacking of lithographed structure and shows twisted multi-layer nanostructure which shows chiral property.

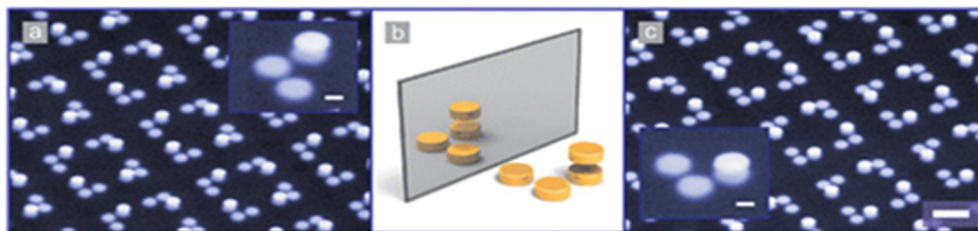


Figure 1. 10 E-beam lithographed three-dimensional chiral oligomers. Scale bar of the overview is 500 nm and for the insets is 100 nm.

Despite precision over the constructed nano-morphology by selective arrangements and orientation of the components, introduced methods show limitation on fabricating genuine 3D chiral structures. Constricted z-axis due to fabrication limitations, generation of truly three-dimensional structures are difficult. As an alternative method to construct three-dimensional chiral nanostructures, direct laser writing of chiral structures has been demonstrated as shown in figure 1.12.<sup>40</sup> Gansel and co-workers constructed helical structure using successive two-photon direct laser writing and electroplating. The constructed chiral helical structures show free-standing helical nano-morphology which the helicity of the structure are uniformly rotated around the vertical axis. There are also other top-down approaches to construct chiral nanostructures such as colloidal nanohole lithography, glancing angle deposition, and on-edge lithography.<sup>46-48</sup> These top-down fabrication methods holds much advantage in generating low-symmetry yet complex 3D nanostructures.

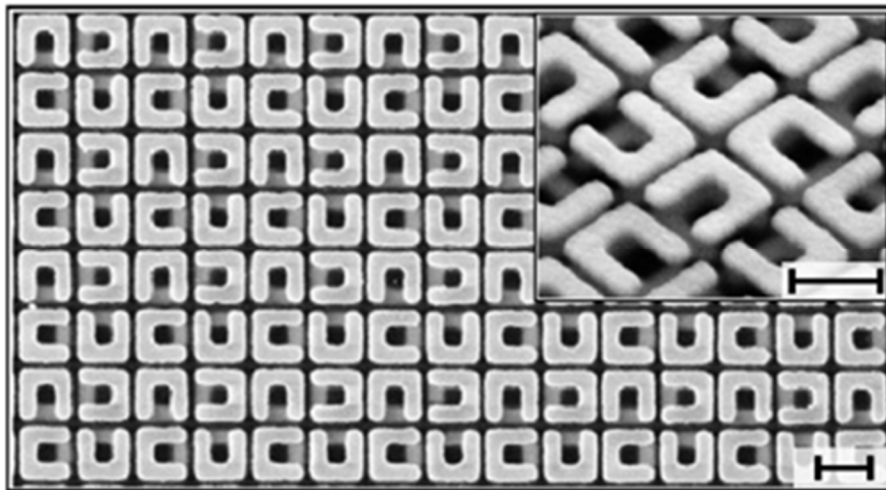


Figure 1. 11 SEM images of chiral unit cell composed of gold split-ring-resonators. Scale bars are 400 nm

While construction of three-dimensional structure through top-down method holds advantage in constructing complex structures, there also exists few intrinsic limitations of the top-down fabrication method. When the chiral nanomaterial is in a solution, the surrounding environment is in an isotropic media. However, top-down fabricated structures are always fixed on an interface which contains various types of media. Also, fabrication process is far too complex which leads to high initial preparation cost and slow processing speed. This difficulty in engineering and industrial perspective hinders the macroscopic patterning of nanostructures. Also, while there has been significant enhancement in lithography technology, the limited material pool for lithography process and relatively low spatial resolution derived from the diffraction limit are major limitations for sub-wavelength scale chiral nanomaterials for practical application.

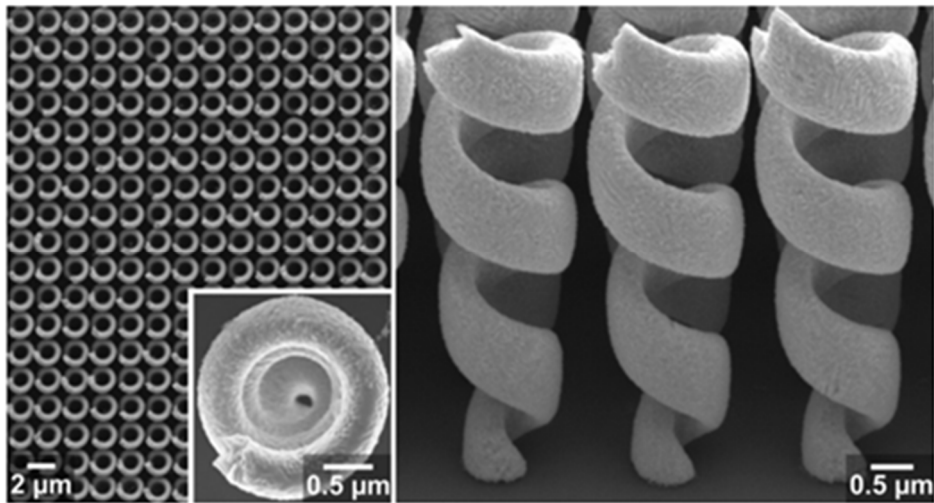


Figure 1. 12 Top(left) and Side(right) view of gold-helix metamaterials fabricated by direct-laser writing.

## 1.4 Chiral Assembly of Nanoparticles

While top-down synthesis method approaches chiral nanostructure generation from systematized fabrication process, chiral assembly of nanoparticles utilize the helical structures already existing to control orientation of nanomaterials. Assembled of nanoparticles exhibit collective chirality respect to the orientation handedness, and the resulting chiroptic properties are strictly determined by the geometrical orientations of the nanoparticles. In this regard, self-assembly of nanomaterials in a chiral manner using biomolecules provide a sophisticated approach for chiral nanostructure generation. Chiral assembly of nanoparticles are categorized into two smaller sub-section groups: biomolecules (amino acid and peptide) induced chiral assembly and DNA mediated chiral assembly nanostructures.

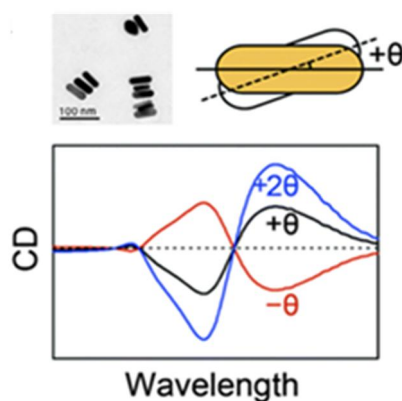


Figure 1. 13 Gold nanorods oligomers twisted by cysteine. CD signal with nanorod scheme and TEM image shows change in spectra respect to twist angle.

In the biological system, amino acid and peptides are basic building blocks. These fundamental building blocks of biological system range widely in molecular size as small amino acids forming into long peptide chains. While there exist large

size differences between biomolecules and nanoparticles, recently reported researches indicate that assembly of nanomaterials using various size of biological building blocks exhibit unique and controllable chiroptic responses.<sup>37,49,58-61,50-57</sup> Wu and coworkers observed generation of chiroptical responses from the Au nanorod orientation control to break the symmetry using cysteine molecule as shown in figure 1.13.<sup>62</sup> Au nanorod oligomer structure was collectively assembled using electrostatic interactions of citrate molecules and cysteine modified Au nanorod. In the nanorod oligomer system, cysteine and the citrate surfactant is believed to be cooperatively inducing the Au nanorods' twisted conformation. In a very similar approach using tripeptide, glutathione, end-to-end assembly of Au nanorods was demonstrated in chiral configuration. The overall chirality of the Au nanorod end-to-end assembly was directed by the molecular chirality of glutathione.

More complex peptide structures such as alpha-helical coiled structures or peptide amphiphile, has been used for chiral assembly. Wang and coworkers used a peptide sequence to generate a nanofibril structure, which is to be used as chiral template.<sup>50</sup> When Au nanoparticle solution was mixed with nanofibril, Au nanoparticles were self-assembled into a double helical structure along the nanofibril template. Peptide amphiphiles have also been used as the purpose of peptide-based scaffold for helical nanoparticle assembly. Among various researches using peptide amphiphiles, Rosi and co-workers paid attention to alkyl-chain terminated oligopeptide, C<sub>11</sub>H<sub>23</sub>-AYSSGAPPMPFF (C<sub>12</sub>-PEPAu), to systematically generate double-helix array of Au nanoparticles.<sup>49</sup> Utilization of peptide amphiphiles for chiral nanostructures synthesis created uniform nanofibers of left- and right-handed helical morphology. The nucleation and growth of the Au nanoparticles occurred simultaneously with the self-assembly of peptide respect to the chirality of peptide amphiphile. Similarly, utilizing a modified peptide structures, C<sub>12</sub>-PEPAu, a single-helical array of plasmonic

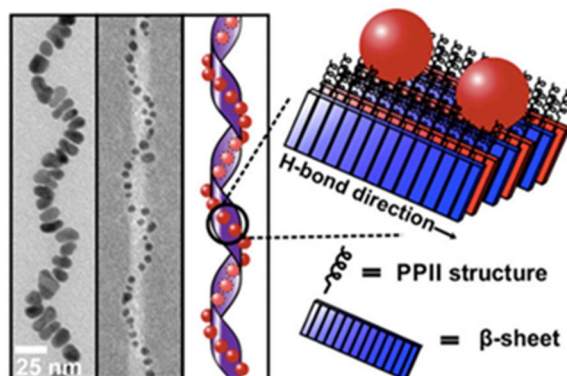


Figure 1. 14 TEM images and model of chiral nanoparticle assemblies template via C18-(PEPAuM ox)<sub>2</sub> superstructures with helical ribbon geometry.

nanoparticles with strong chiroptic response has been demonstrated as shown in figure 1.14.<sup>57</sup> By using an oxidized form of peptide amphiphile, C18-(PEPAuM-ox)<sub>2</sub>, assembly of a single-helix structure instead of a double helix was possible. Specifically, simultaneous synthesis and assembly of Au nanorod into a single helical chiral structure created strong and perfectly chiral bi-signate response in the visible wavelength region.

In the sense of controllability DNA is a very powerful tool to artificially engineer and assemble nanomaterials into complex structures. With the increase in accessibility of controlling DNA sequences, controlling DNA structures to become a scaffold for chiral nanomaterial has shine various design principles and synthesis methods.<sup>63-71</sup> Kotov and co-workers utilized DNA to induce chiral assembly structure.<sup>63</sup> Using the well-known polymerase chain reaction(PCR) in a very unusual approach, PCR process using DNA conjugated Au nanoparticles

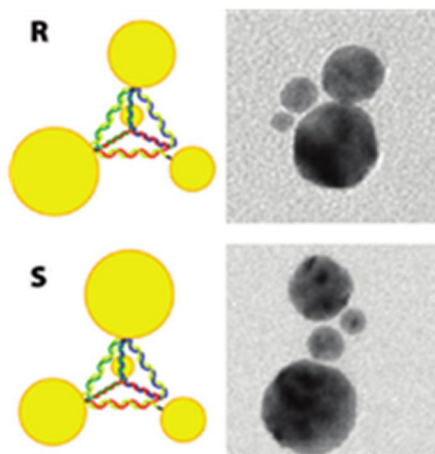


Figure 1.15 Schematic models and TEM images of enantiomeric plasmonic pyramid assemblies.

created new extensions of DNA oligomers connected by DNA as linkers. By the controlling DNA hybridization and gold nanoparticle conjugation, various chiral nanostructures including, dimers, trimers, and multi-chained gold nanoparticles were generated. The nanostructure assembly was precisely tuned through the primer density and PCR cycles. As an alternative method, Alivisatos and co-workers utilized premade single-stranded DNA sequence to build a chiral pyramid with three-dimensional structure as shown in figure 1.15.<sup>71</sup> Total of four types of DNA sequences were used to construct each planes of the pyramid and at each corner of the pyramid, Au nanoparticle with difference sizes, 5, 10, 15, and 20 nm was located. By alternating the position of 5 and 10nm sized nanoparticles at the corner of pyramid, the R and S chiral conformation of the pyramid was modulated. Instead of simply using the DNA as scaffold, DNA was also utilized as a tile or origami template to construct highly complex chiral nanostructures. The DNA origami method manifested precise morphology and assembly control which,

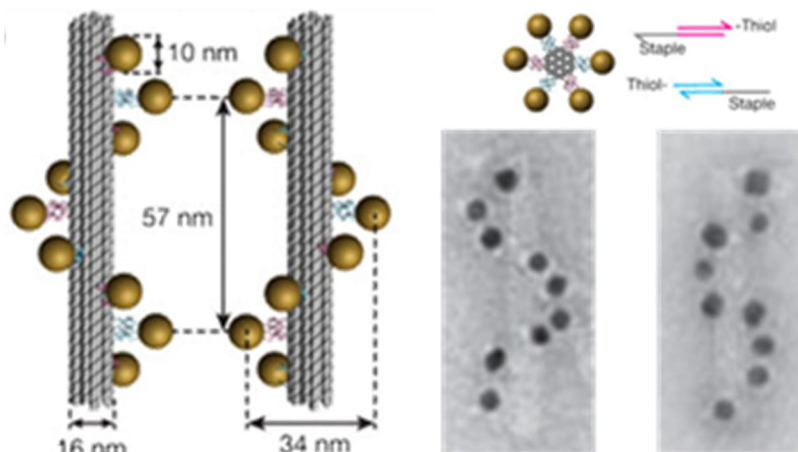


Figure 1.16 Left- and right-handed Au helices based on a DNA 24-helix bundle. Achiral gold nanoparticles are assembled around the bundle in a helical order to create chiral structures

inter-particle spacing was exceptionally well controlled with high yield. Liedl and co-workers utilized 24-helix DNA bundle with 9 decoration sites for nanoparticles to be placed, in order to construct the chiral structure as shown in figure 1.16.<sup>69</sup> The constructed DNA origami structure with plasmonic nanoparticles showed a significantly strong bisignate CD signals respect to the chirality of the structure at plasmonic resonance. More interestingly, generated chiral structure showed opposite color changing behavior under polarization-resolved transmission condition depending on the handedness of utilized structures.

## 1.5 Induced Chirality from Chiral Molecules

While the introduced examples of chiral nanostructures from chiral assembly of nanoparticles which biomolecules were used to create chiral orientation of nano components, the following subchapter will mainly focus on chiroptic responses directly induced from a single plasmonic nanostructure. When chiral biomolecules are at approximate of plasmonic metal surface, chirality of biomolecules could be induced in following two possible ways: (i) electric interference of molecules and nanoparticles resulting creation of chiral hybridized electronic states which is known as molecule induced chirality, and (ii) surface or atomic structural alteration by the adsorption of chiral ligands at the nanoparticle surfaces which is chiral atomic configuration generation.

### Molecule induced Chirality

The chirality found in molecular structures could be manifested on plasmonic nanomaterials through electronic coupling between interfaces of molecules and metal surfaces. By selectively adsorbing organic ligands or molecules to the metal surfaces, the present local electric field near the metal surfaces is influenced by molecular dipole to generate chiroptical properties such as circular dichroism (CD) and optical rotatory dispersion (ORD).<sup>72-77</sup> With the aid of localized surface plasmon resonance of plasmonic metal nanoparticles, the chiroptic response of biomolecules, which are known to be relatively weak, are significantly amplified and detectable at visible wavelength.

Representative example of induced chirality is demonstrated by Govorov and Markovich group using Au island structures. Strong circular dichroism at surface plasmon resonance was induced by introducing chiral molecules, riboflavin, in the vicinity of the metal surface without direct bonding as shown in

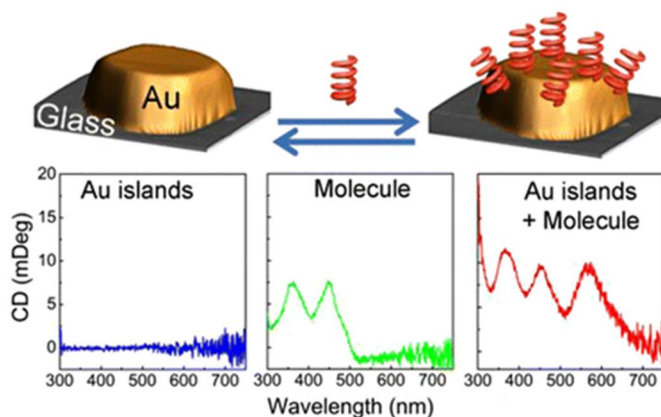


Figure 1. 17 Chiroptic response of plasmonic nanoparticles conjugated with biomolecules a) Molecule induced chiroptic response of plasmonic gold island.

figure 1.17.<sup>75</sup> The circular dichroism of biomolecules originally exists in near UV range. However, when chiral molecules were placed above a spacer group to prevent direct contact of chiral molecules with Au metal surface, achiral structure exhibited chiroptic response in the region of visible wavelength. Furthermore, Markovich group demonstrated generation of circular dichroism signals in the plasmonic resonance range using cubic silver nanoparticle and glutathione ligands.<sup>76</sup> By controlling the pH environment near nanostructure with glutathione molecule, they were able to modify optical response such as CD and absorption spectra. This change in optical response was due to the reversible oxidation of thiol group to form di-glutathione. In another cases, polyproline II-based helical peptides attachment to silver nanocubes through a cysteine linker resulted in induced circular dichroism as shown in figure 1.18.<sup>77</sup> Interestingly, two chiral peptides with the same helicity induced opposite circular dichroism responses, and difference in circular dichroism response was due to the adsorption direction of the helix ends. For the control experiment, sharpening of the edges of the silver nanocubes did not show significant changes which indicate that the chirality was directly related to the structures of chiral molecules itself.

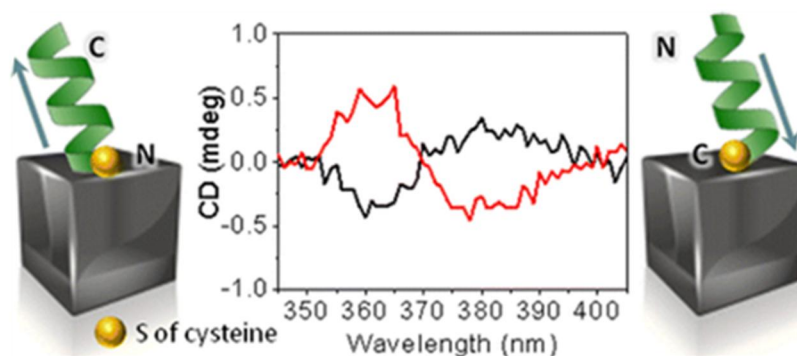


Figure 1. 18 helical peptide conjugated silver nanocubes and their CD signals

### Chiral atomic re-configuration

As the second type of molecule induced chirality, chirality could be manifested by the structural distortion of atomic configuration in metal nanoclusters. These structural distortions could be induced from atomic surface interaction with chiral molecules. Despite the fact that chirality is derived from interaction between chiral molecule and nanoparticle, the origin of chirality could be distinguished from the chiral electronic coupling. The chiroptic response in the visible range is induced from the cluster morphology. These chiral nanoclusters are interesting, especially since they possess high absorptivity and photo-stability due to intrinsic chiral structures, resulting in defined absorption spectra and circular dichroism response in the visible range.<sup>55,78,79</sup>

Wang group synthesized chiral gold nanocluster  $[\text{Au}_{20}(\text{PP3})_4]\text{Cl}_4$  by reducing gold(I)-tetrphosphine precursor in dichloromethane solvent.<sup>80</sup> The synthesized nanocluster structures have  $C_3$  symmetry with  $\text{Au}_{20}$  core being surrounded by four tetrphosphine ligands. The morphology of core  $\text{Au}_{20}$  is distorted by nearby existing ligands and generated structures can be divided into

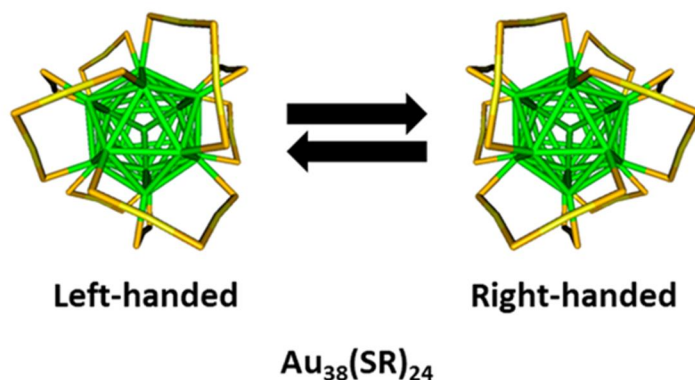


Figure 1. 19 Chiral configuration of atoms by chiral ligand-metal interaction a) Left- and Right-handed chiral  $\text{Au}_{38}(\text{SR})_{24}$  cluster.

icosahedral  $\text{Au}_{13}$  and a spiral Y-shaped  $\text{Au}_7$  unit in a chiral rotation. Bürgi and coworkers studied reorganization of surface gold atoms through thiolation on gold nanoclusters. Surface bound thiol-based chiral molecules induce the chiral rearrangement of the surface gold atoms as shown in figure 1.19.<sup>81</sup> Examination of the  $\text{Au}_{102}(\text{SR})_{44}$  and  $\text{Au}_{38}(\text{SR})_{24}$  crystal structures, generation of chirality inversion respect to input enantiomers of thiolated ligands was observed. In addition to this result, Kornberg's group analyzed chiral gold nanoclusters through powder X-ray diffraction to show the atomic distortion.<sup>82</sup> They investigated gold nanoparticles with p-mercaptobenzoic acid (p-MBA) adsorbed on the surface, and revealed that chiral rearrangement of atomic structures occurred due to the adsorption. The arrangements in the core was Marks decahedron but the surrounding atoms had irregular chiral geometries which is expected to be from p-MBA.

Tsukuda and coworkers showed that  $\text{Au}_{11}$  nanoclusters to form chiral core structure  $[\text{Au}_{11}(\text{BINAP})_4\text{X}_2]^+$  (X corresponding to Cl or Br) by adsorption of chiral phosphine ligands distorting the surface. This chiral nanocluster

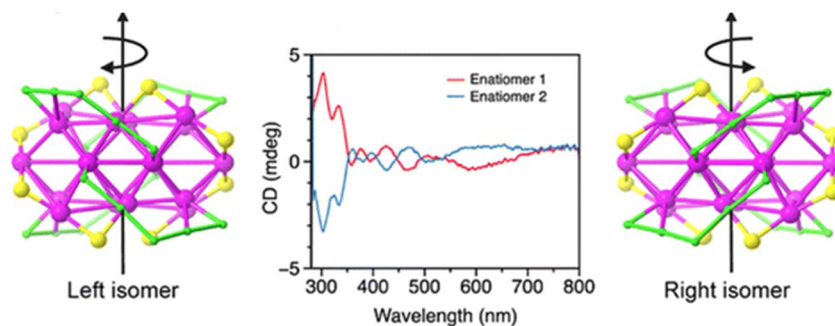


Figure 1. 20 Two enantiomers of Au<sub>28</sub>(TBBT)<sub>20</sub> and its corresponding CD spectra.

displayed a noticeable chiroptical properties in the visible range. Considering the size and configuration of Au<sub>11</sub><sup>+</sup> core, it is easily deformed since ten out of eleven atoms are located on the surface.<sup>83</sup> Thus, adsorption of the chiral phosphine ligands on the surface of the cluster induce distortion of the core structures which forms a chiral core. This chiral geometry of Au<sub>11</sub><sup>+</sup> core has been verified via the single-crystal X-ray diffraction. Similarly, Jin and coworkers, as shown in figure 1.20, they synthesized Au<sub>28</sub>(TBBT)<sub>20</sub> nanocluster and the distinguished two enantiomers using CD spectra.<sup>84</sup> The synthesized nanocluster is composed of Au<sub>20</sub> core with four dimeric staples and eight bridging thiolates. The Au<sub>20</sub> core consists of two interpenetrating Au<sub>13</sub> cuboctahedron which forms a bicuboctahedron. Furthermore, peripheral dimeric staples (-SR-Au-SR-Au-SR-) and bridging thiolates coordination show quasi-D<sub>2</sub> chiral symmetry. The overall chirality of the cluster is determined by the direction of the 2-fold rotational symmetry.

## 1.6 Bibliography

- (1) Inaki, M.; Liu, J.; Matsuno, K. Cell Chirality: Its Origin and Roles in Left-Right Asymmetric Development. *Philos. Trans. R. Soc. B Biol. Sci.* **2016**, *371* (1710). <https://doi.org/10.1098/rstb.2015.0403>.
- (2) Tee, Y. H.; Shemesh, T.; Thiagarajan, V.; Hariadi, R. F.; Anderson, K. L.; Page, C.; Volkmann, N.; Hanein, D.; Sivaramakrishnan, S.; Kozlov, M. M.; et al. Cellular Chirality Arising from the Self-Organization of the Actin Cytoskeleton. *Nat. Cell Biol.* **2015**, *17* (4), 445–457. <https://doi.org/10.1038/ncb3137>.
- (3) Jiang, W.; Yi, X.; McKee, M. D. Chiral Biomineralized Structures and Their Biomimetic Synthesis. *Mater. Horizons* **2019**, *6* (10), 1974–1990. <https://doi.org/10.1039/c9mh00431a>.
- (4) Levin, M. Left-Right Asymmetry in Embryonic Development: A Comprehensive Review. *Mech. Dev.* **2005**, *122* (1), 3–25. <https://doi.org/10.1016/j.mod.2004.08.006>.
- (5) Mason, S. F. Origins of Biomolecular Handedness. *Nature* **1984**, *311* (5981), 19–23. <https://doi.org/10.1038/311019a0>.
- (6) Brown, N. A.; Wolpert, L. The Development of Handedness in Left/Right Asymmetry. *Development* **1990**, *109* (1), 1–9.
- (7) Salam, A. The Role of Chirality in the Origin of Life. *J. Mol. Evol.* **1991**, *33*, 105–113.
- (8) Morrow, S. M.; Bissette, A. J.; Fletcher, S. P. Transmission of Chirality through Space and across Length Scales. *Nat. Nanotechnol.* **2017**, *12* (5), 410–419. <https://doi.org/10.1038/nnano.2017.62>.

- (9) Lebreton, G.; Géminard, C.; Lapraz, F.; Pyrpassopoulos, S.; Cerezo, D.; Spéder, P.; Ostap, E. M.; Noselli, S. Molecular to Organismal Chirality Is Induced by the Conserved Myosin 1D. *Science (80-. )*. **2018**, *362* (6417), 949–952. <https://doi.org/10.1126/science.aat8642>.
- (10) Wang, J. S.; Wang, G.; Feng, X. Q.; Kitamura, T.; Kang, Y. L.; Yu, S. W.; Qin, Q. H. Hierarchical Chirality Transfer in the Growth of Towel Gourd Tendrils. *Sci. Rep.* **2013**, *3*, 1–7. <https://doi.org/10.1038/srep03102>.
- (11) Maderspacher, F. Snail Chirality: The Unwinding. *Curr. Biol.* **2016**, *26* (5), R215–R217. <https://doi.org/10.1016/j.cub.2016.02.008>.
- (12) Wharton, S. J.; Basu, S. P.; Ashe, H. L. Body Handedness Is Directed by Genetically Determined Cytoskeletal Dynamics in the Early Embryo. *Curr. Biol.* **2004**, *14*, 1550–1558. <https://doi.org/10.1016/j.cub.2004.08.011>.
- (13) Mehl, M. J.; Hicks, D.; Toher, C.; Levy, O.; Hanson, R. M.; Hart, G.; Curtarolo, S. The AFLOW Library of Crystallographic Prototypes: Part 1. *Comput. Mater. Sci.* **2017**, *136*, S1–S828. <https://doi.org/10.1016/j.commatsci.2017.01.017>.
- (14) Hicks, D.; Mehl, M. J.; Gossett, E.; Toher, C.; Levy, O.; Hanson, R. M.; Hart, G.; Curtarolo, S. The AFLOW Library of Crystallographic Prototypes: Part 2. *Comput. Mater. Sci.* **2019**, *161*, S1–S1011. <https://doi.org/10.1016/j.commatsci.2018.10.043>.
- (15) Halasyamani, P. S.; Poeppelmeier, K. R. Noncentrosymmetric Oxides. *Chem. Mater.* **1998**, *10* (10), 2753–2769. <https://doi.org/10.1021/cm980140w>.
- (16) Ahn, J.; Kim, D. H.; Coquerel, G.; Kim, W. S. Chiral Symmetry Breaking and Deracemization of Sodium Chlorate in Turbulent Flow. *Cryst. Growth Des.* **2018**, *18* (1), 297–306. <https://doi.org/10.1021/acs.cgd.7b01247>.

- (17) Szurgot, M.; Szurgot, J. Chiral Symmetry Breaking in Sodium Chlorate Crystallization from Unstirred Solution. *Cryst. Res. Technol.* **1995**, *30* (7), 949–956. <https://doi.org/10.1002/crat.2170300714>.
- (18) Bragg, W. H. The X-Ray Spectra Given by Crystals of Sulphur and Quartz. *Proc. R. Soc. A Math. Phys. Eng. Sci.* **1914**, *89* (614), 575–580. <https://doi.org/10.1098/rspa.1914.0025>.
- (19) Arago, F. J. D. Mémoire Sur Une Modification Remarquable Qu'éprouvent Les Rayons Lumineux Dans Leur Passage à Travers Certains Corps Diaphanes et Sur Quelques Autres Nouveaux Phénomènes d'optique. In *Mémoires de la classe des sciences mathématiques et physiques de l'Institut Impérial de France*; Paris, 1811; Vol. I, pp 93–134.
- (20) Im, S. W.; Ahn, H.; Kim, R. M.; Cho, N. H.; Kim, H.; Lim, Y.; Lee, H.; Nam, K. T. Chiral Surface and Geometry of Metal Nanocrystals. *Adv. Mater.* **2019**, 1905758. <https://doi.org/10.1002/adma.201905758>.
- (21) Wang, P. P.; Yu, S. J.; Govorov, A. O.; Ouyang, M. Cooperative Expression of Atomic Chirality in Inorganic Nanostructures. *Nat. Commun.* **2017**, *8*. <https://doi.org/10.1038/ncomms14312>.
- (22) Ben-Moshe, A.; Govorov, A. O.; Markovich, G. Enantioselective Synthesis of Intrinsically Chiral Mercury Sulfide Nanocrystals. *Angew. Chemie - Int. Ed.* **2013**, *52* (4), 1275–1279. <https://doi.org/10.1002/anie.201207489>.
- (23) Ben-Moshe, A.; Wolf, S. G.; Sadan, M. B.; Houben, L.; Fan, Z.; Govorov, A. O.; Markovich, G. Enantioselective Control of Lattice and Shape Chirality in Inorganic Nanostructures Using Chiral Biomolecules. *Nat. Commun.* **2014**, *5*. <https://doi.org/10.1038/ncomms5302>.

- (24) Kulp, E. A.; Switzer, J. A. Electrochemical Biomineralization: The Deposition of Calcite with Chiral Morphologies. *J. Am. Chem. Soc.* **2007**, *129* (49), 15120–15121. <https://doi.org/10.1021/ja076303b>.
- (25) Hazen, R. M.; Sholl, D. S. Chiral Selection on Inorganic Crystalline Surfaces. *Nat. Mater.* **2003**, *2* (6), 367–374. <https://doi.org/10.1038/nmat879>.
- (26) Sugawara, T.; Suwa, Y.; Ohkawa, K.; Yamamoto, H. Chiral Biomineralization: Mirror-Imaged Helical Growth of Calcite with Chiral Phosphoserine Copolypeptides. *Macromol. Rapid Commun.* **2003**, *24* (14), 847–851. <https://doi.org/10.1002/marc.200350030>.
- (27) Jiang, W.; Pacella, M. S.; Athanasiadou, D.; Nelea, V.; Vali, H.; Hazen, R. M.; Gray, J. J.; McKee, M. D. Chiral Acidic Amino Acids Induce Chiral Hierarchical Structure in Calcium Carbonate. *Nat. Commun.* **2017**, *8* (1), 15066. <https://doi.org/10.1038/ncomms15066>.
- (28) Pendry, J. B. A Chiral Route to Negative Refraction. *Science* (80-. ). **2004**, *306* (5700), 1353–1355. <https://doi.org/10.1126/science.1104467>.
- (29) Hendry, E.; Carpy, T.; Johnston, J.; Popland, M.; Mikhaylovskiy, R. V.; Laphorn, A. J.; Kelly, S. M.; Barron, L. D.; Gadegaard, N.; Kadodwala, M. Ultrasensitive Detection and Characterization of Biomolecules Using Superchiral Fields. *Nat. Nanotechnol.* **2010**, *5* (11), 783–787. <https://doi.org/10.1038/nnano.2010.209>.
- (30) Zhang, S.; Zhou, J.; Park, Y.-S.; Rho, J.; Singh, R.; Nam, S.; Azad, A. K.; Chen, H.-T.; Yin, X.; Taylor, A. J.; et al. Photoinduced Handedness Switching in Terahertz Chiral Metamolecules. *Nat. Commun.* **2012**, *3* (1), 942. <https://doi.org/10.1038/ncomms1908>.
- (31) Meinzer, N.; Barnes, W. L.; Hooper, I. R. Plasmonic Meta-Atoms and

Metasurfaces. *Nat. Photonics* **2014**, *8* (12), 889–898.

<https://doi.org/10.1038/nphoton.2014.247>.

- (32) Gansel, J. K.; Thiel, M.; Rill, M. S.; Decker, M.; Bade, K.; Saile, V.; Von Freymann, G.; Linden, S.; Wegener, M. Gold Helix Photonic Metamaterial as Broadband Circular Polarizer. *Science (80-. )*. **2009**, *325* (5947), 1513–1515.  
<https://doi.org/10.1126/science.1177031>.
- (33) Zhang, H.; Zheng, X.; Kwok, R. T. K.; Wang, J.; Leung, N. L. C.; Shi, L.; Sun, J. Z.; Tang, Z.; Lam, J. W. Y.; Qin, A.; et al. In Situ Monitoring of Molecular Aggregation Using Circular Dichroism. *Nat. Commun.* **2018**, *9* (1), 4961.  
<https://doi.org/10.1038/s41467-018-07299-3>.
- (34) Greenfield, N. J. Using Circular Dichroism Spectra to Estimate Protein Secondary Structure. *Nat. Protoc.* **2006**, *1* (6), 2876–2890.  
<https://doi.org/10.1038/nprot.2006.202>.
- (35) Hoffmann, M.; Grajewski, J.; Gawronski, J. Extending the Applications of Circular Dichroism in Structure Elucidation: Aqueous Environment Breaks the Symmetry of Tartrate Dianion. *New J. Chem.* **2010**, *34* (9), 2020.  
<https://doi.org/10.1039/c0nj00072h>.
- (36) *Gold Nanoparticles: Properties, Characterization and Fabrication*; P.E.Chow, Ed.; Nova Science Publishers, Inc., 2010.
- (37) Liu, S.-D.; Liu, J.-Y.; Cao, Z.; Fan, J.-L.; Lei, D. Dynamic Tuning of Enhanced Intrinsic Circular Dichroism in Plasmonic Stereo-Metamolecule Array with Surface Lattice Resonance. *Nanophotonics* **2020**, *9* (10), 3419–3434.  
<https://doi.org/10.1515/nanoph-2020-0130>.
- (38) Tokunaga, E.; Yamamoto, T.; Ito, E.; Shibata, N. Understanding the Thalidomide

Chirality in Biological Processes by the Self-Disproportionation of Enantiomers. *Sci. Rep.* **2018**, *8* (1), 17131. <https://doi.org/10.1038/s41598-018-35457-6>.

- (39) Greber, T.; Šljivančanin, Ž.; Schillinger, R.; Wider, J.; Hammer, B. Chiral Recognition of Organic Molecules by Atomic Kinks on Surfaces. *Phys. Rev. Lett.* **2006**, *96* (5), 056103. <https://doi.org/10.1103/PhysRevLett.96.056103>.
- (40) Gansel, J. K.; Latzel, M.; Frölich, A.; Kaschke, J.; Thiel, M.; Wegener, M. Tapered Gold-Helix Metamaterials as Improved Circular Polarizers. *Appl. Phys. Lett.* **2012**, *100* (10). <https://doi.org/10.1063/1.3693181>.
- (41) Hentschel, M.; Schäferling, M.; Weiss, T.; Liu, N.; Giessen, H. Three-Dimensional Chiral Plasmonic Oligomers. *Nano Lett.* **2012**, *12* (5), 2542–2547. <https://doi.org/10.1021/nl300769x>.
- (42) Radke, A.; Gissibl, T.; Klotzbücher, T.; Braun, P. V.; Giessen, H. Three-Dimensional Bichiral Plasmonic Crystals Fabricated by Direct Laser Writing and Electroless Silver Plating. *Adv. Mater.* **2011**, *23* (27), 3018–3021. <https://doi.org/10.1002/adma.201100543>.
- (43) Decker, M.; Zhao, R.; Soukoulis, C. M.; Linden, S.; Wegener, M. Twisted Split-Ring-Resonator Photonic Metamaterial with Huge Optical Activity. *Opt. Lett.* **2010**, *35* (10), 1593. <https://doi.org/10.1364/ol.35.001593>.
- (44) Soukoulis, C. M.; Wegener, M. Past Achievements and Future Challenges in the Development of Three-Dimensional Photonic Metamaterials. *Nat. Photonics* **2011**, *5* (9), 523–530. <https://doi.org/10.1038/nphoton.2011.154>.
- (45) Valev, V. K.; Baumberg, J. J.; Sibilica, C.; Verbiest, T. Chirality and Chiroptical Effects in Plasmonic Nanostructures: Fundamentals, Recent Progress, and Outlook. *Adv. Mater.* **2013**, *25* (18), 2517–2534.

<https://doi.org/10.1002/adma.201205178>.

- (46) Dietrich, K.; Lehr, D.; Helgert, C.; Tünnermann, A.; Kley, E. B. Circular Dichroism from Chiral Nanomaterial Fabricated by On-Edge Lithography. *Adv. Mater.* **2012**, *24* (44), 321–325. <https://doi.org/10.1002/adma.201203424>.
- (47) Frank, B.; Yin, X.; Schäferling, M.; Zhao, J.; Hein, S. M.; Braun, P. V.; Giessen, H. Large-Area 3D Chiral Plasmonic Structures. *ACS Nano* **2013**, *7* (7), 6321–6329. <https://doi.org/10.1021/nn402370x>.
- (48) Hou, Y.; Li, S.; Su, Y.; Huang, X.; Liu, Y.; Huang, L.; Yu, Y.; Gao, F.; Zhang, Z.; Du, J. Design and Fabrication of Three-Dimensional Chiral Nanostructures Based on Stepwise Glancing Angle Deposition Technology. *Langmuir* **2013**, *29* (3), 867–872. <https://doi.org/10.1021/la304122f>.
- (49) Chen, C. L.; Zhang, P.; Rosi, N. L. A New Peptide-Based Method for the Design and Synthesis of Nanoparticle Superstructures: Construction of Highly Ordered Gold Nanoparticle Double Helices. *J. Am. Chem. Soc.* **2008**, *130* (41), 13555–13557. <https://doi.org/10.1021/ja805683r>.
- (50) Fu, X.; Wang, Y.; Huang, L.; Sha, Y.; Gui, L.; Lai, L.; Tang, Y. Assemblies of Metal Nanoparticles and Self-Assembled Peptide Fibrils - Formation of Double Helical and Single-Chain Arrays of Metal Nanoparticles. *Adv. Mater.* **2003**, *15* (11), 902–906. <https://doi.org/10.1002/adma.200304624>.
- (51) Lee, H.-E.; Ahn, H.-Y.; Lee, J.; Nam, K. T. Biomolecule-Enabled Chiral Assembly of Plasmonic Nanostructures. *ChemNanoMat* **2017**, *3* (10), 685–697. <https://doi.org/10.1002/cnma.201700208>.
- (52) Ma, W.; Kuang, H.; Wang, L.; Xu, L.; Chang, W. S.; Zhang, H.; Sun, M.; Zhu, Y.; Zhao, Y.; Liu, L.; et al. Chiral Plasmonics of Self-Assembled Nanorod

Dimers. *Sci. Rep.* **2013**, *3*, 1–6. <https://doi.org/10.1038/srep01934>.

- (53) Guerrero-Martínez, A.; Alonso-Gómez, J. L.; Auguié, B.; Cid, M. M.; Liz-Marzán, L. M. From Individual to Collective Chirality in Metal Nanoparticles. *Nano Today* **2011**, *6* (4), 381–400. <https://doi.org/10.1016/j.nantod.2011.06.003>.
- (54) Cheng, J.; Le Saux, G.; Gao, J.; Buffeteau, T.; Battie, Y.; Barois, P.; Ponsinet, V.; Delville, M. H.; Ersen, O.; Pouget, E.; et al. GoldHelix: Gold Nanoparticles Forming 3D Helical Superstructures with Controlled Morphology and Strong Chiroptical Property. *ACS Nano* **2017**, *11* (4), 3806–3818. <https://doi.org/10.1021/acsnano.6b08723>.
- (55) Kumar, J.; Thomas, K. G.; Liz-Marzán, L. M. Nanoscale Chirality in Metal and Semiconductor Nanoparticles. *Chem. Commun.* **2016**, *52* (85), 12555–12569. <https://doi.org/10.1039/c6cc05613j>.
- (56) Cheng, J.; Hill, E. H.; Zheng, Y.; He, T.; Liu, Y. Optically Active Plasmonic Resonance in Self-Assembled Nanostructures. *Mater. Chem. Front.* **2018**, *2* (4), 662–678. <https://doi.org/10.1039/c7qm00601b>.
- (57) Merg, A. D.; Boatz, J. C.; Mandal, A.; Zhao, G.; Mokashi-Punekar, S.; Liu, C.; Wang, X.; Zhang, P.; Van Der Wel, P. C. A.; Rosi, N. L. Peptide-Directed Assembly of Single-Helical Gold Nanoparticle Superstructures Exhibiting Intense Chiroptical Activity. *J. Am. Chem. Soc.* **2016**, *138* (41), 13655–13663. <https://doi.org/10.1021/jacs.6b07322>.
- (58) Chen, L.; Zheng, J.; Feng, J.; Qian, Q.; Zhou, Y. Reversible Modulation of Plasmonic Chiral Signals of Achiral Gold Nanorods Using a Chiral Supramolecular Template. *Chem. Commun.* **2019**, *55* (76), 11378–11381. <https://doi.org/10.1039/c9cc06050b>.

- (59) Lan, X.; Wang, Q. Self-Assembly of Chiral Plasmonic Nanostructures. *Adv. Mater.* **2016**, *28* (47), 10499–10507. <https://doi.org/10.1002/adma.201600697>.
- (60) Song, C.; Blaber, M. G.; Zhao, G.; Zhang, P.; Fry, H. C.; Schatz, G. C.; Rosi, N. L. Tailorable Plasmonic Circular Dichroism Properties of Helical Nanoparticle Superstructures. *Nano Lett.* **2013**, *13* (7), 3256–3261. <https://doi.org/10.1021/nl4013776>.
- (61) Ma, W.; Hao, C.; Sun, M.; Xu, L.; Xu, C.; Kuang, H. Tuning of Chiral Construction, Structural Diversity, Scale Transformation and Chiroptical Applications. *Mater. Horizons* **2018**, *5* (2), 141–161. <https://doi.org/10.1039/c7mh00966f>.
- (62) Hou, S.; Zhang, H.; Yan, J.; Ji, Y.; Wen, T.; Liu, W.; Hu, Z.; Wu, X. Plasmonic Circular Dichroism in Side-by-Side Oligomers of Gold Nanorods: The Influence of Chiral Molecule Location and Interparticle Distance. *Phys. Chem. Chem. Phys.* **2015**, *17* (12), 8187–8193. <https://doi.org/10.1039/c4cp06029f>.
- (63) Chen, W.; Bian, A.; Agarwal, A.; Liu, L.; Shen, H.; Wang, L.; Xu, C.; Kotov, N. A. Nanoparticle Superstructures Made by Polymerase Chain Reaction: Collective Interactions of Nanoparticles and a New Principle for Chiral Materials. *Nano Lett.* **2009**, *9* (5), 2153–2159. <https://doi.org/10.1021/nl900726s>.
- (64) Kneer, L. M.; Roller, E. M.; Besteiro, L. V.; Schreiber, R.; Govorov, A. O.; Liedl, T. Circular Dichroism of Chiral Molecules in DNA-Assembled Plasmonic Hotspots. *ACS Nano* **2018**, *12* (9), 9110–9115. <https://doi.org/10.1021/acsnano.8b03146>.
- (65) Liu, Q.; Kuzyk, A.; Endo, M.; Smalyukh, I. I. Colloidal Plasmonic DNA-Origami with Photo-Switchable Chirality in Liquid Crystals. *Opt. Lett.* **2019**, *44* (11),

2831. <https://doi.org/10.1364/ol.44.002831>.

- (66) Shen, X.; Asenjo-Garcia, A.; Liu, Q.; Jiang, Q.; García De Abajo, F. J.; Liu, N.; Ding, B. Three-Dimensional Plasmonic Chiral Tetramers Assembled by DNA Origami. *Nano Lett.* **2013**, *13* (5), 2128–2133. <https://doi.org/10.1021/nl400538y>.
- (67) Schreiber, R.; Luong, N.; Fan, Z.; Kuzyk, A.; Nickels, P. C.; Zhang, T.; Smith, D. M.; Yurke, B.; Kuang, W.; Govorov, A. O.; et al. Chiral Plasmonic DNA Nanostructures with Switchable Circular Dichroism. *Nat. Commun.* **2013**, *4* (1), 2948. <https://doi.org/10.1038/ncomms3948>.
- (68) Shemer, G.; Krichevski, O.; Markovich, G.; Molotsky, T.; Lubitz, I.; Kotlyar, A. B. Chirality of Silver Nanoparticles Synthesized on DNA. *J. Am. Chem. Soc.* **2006**, *128* (34), 11006–11007. <https://doi.org/10.1021/ja063702i>.
- (69) Kuzyk, A.; Schreiber, R.; Fan, Z.; Pardatscher, G.; Roller, E.-M.; Högele, A.; Simmel, F. C.; Govorov, A. O.; Liedl, T. DNA-Based Self-Assembly of Chiral Plasmonic Nanostructures with Tailored Optical Response. *Nature* **2012**, *483* (7389), 311–314. <https://doi.org/10.1038/nature10889>.
- (70) Shen, B.; Kostianen, M. A.; Linko, V. DNA Origami Nanophotonics and Plasmonics at Interfaces. *Langmuir* **2018**, *34* (49), 14911–14920. <https://doi.org/10.1021/acs.langmuir.8b01843>.
- (71) Mastroianni, A. J.; Claridge, S. A.; Paul Alivisatos, A. Pyramidal and Chiral Groupings of Gold Nanocrystals Assembled Using DNA Scaffolds. *J. Am. Chem. Soc.* **2009**, *131* (24), 8455–8459. <https://doi.org/10.1021/ja808570g>.
- (72) Govorov, A. O. Plasmon-Induced Circular Dichroism of a Chiral Molecule in the Vicinity of Metal Nanocrystals. Application to Various Geometries. *J. Phys. Chem. C* **2011**, *115* (16), 7914–7923. <https://doi.org/10.1021/jp1121432>.

- (73) Maoz, B. M.; Van Der Weegen, R.; Fan, Z.; Govorov, A. O.; Ellestad, G.; Berova, N.; Meijer, E. W.; Markovich, G. Plasmonic Chiroptical Response of Silver Nanoparticles Interacting with Chiral Supramolecular Assemblies. *J. Am. Chem. Soc.* **2012**, *134* (42), 17807–17813. <https://doi.org/10.1021/ja309016k>.
- (74) Abdulrahman, N. A.; Fan, Z.; Tonooka, T.; Kelly, S. M.; Gadegaard, N.; Hendry, E.; Govorov, A. O.; Kadodwala, M. Induced Chirality through Electromagnetic Coupling between Chiral Molecular Layers and Plasmonic Nanostructures. *Nano Lett.* **2012**, *12* (2), 977–983. <https://doi.org/10.1021/nl204055r>.
- (75) Maoz, B. M.; Chaikin, Y.; Tesler, A. B.; Bar Elli, O.; Fan, Z.; Govorov, A. O.; Markovich, G. Amplification of Chiroptical Activity of Chiral Biomolecules by Surface Plasmons. *Nano Lett.* **2013**, *13* (3), 1203–1209. <https://doi.org/10.1021/nl304638a>.
- (76) Di Gregorio, M. C.; Ben Moshe, A.; Tirosh, E.; Galantini, L.; Markovich, G. Chiroptical Study of Plasmon-Molecule Interaction: The Case of Interaction of Glutathione with Silver Nanocubes. *J. Phys. Chem. C* **2015**, *119* (30), 17111–17116. <https://doi.org/10.1021/acs.jpcc.5b03272>.
- (77) Levi-Belenkova, T.; Govorov, A. O.; Markovich, G. Orientation-Sensitive Peptide-Induced Plasmonic Circular Dichroism in Silver Nanocubes. *J. Phys. Chem. C* **2016**, *120* (23), 12751–12756. <https://doi.org/10.1021/acs.jpcc.6b03803>.
- (78) Knoppe, S.; Burgi, T. Chirality in Thiolate-Protected Gold Clusters. *Acc. Chem. Res.* **2014**, *47* (4), 1318–1326. <https://doi.org/10.1021/ar400295d>.
- (79) Jesús Pelayo, J.; Valencia, I.; García, A. P.; Chang, L.; López, M.; Toffoli, D.; Stener, M.; Fortunelli, A.; Garzón, I. L. Chirality in Bare and Ligand-Protected Metal Nanoclusters. *Adv. Phys. X* **2018**, *3* (1), 965–998.

<https://doi.org/10.1080/23746149.2018.1509727>.

- (80) Wan, X. K.; Yuan, S. F.; Lin, Z. W.; Wang, Q. M. A Chiral Gold Nanocluster Au<sub>20</sub> Protected by Tetradentate Phosphine Ligands. *Angew. Chemie - Int. Ed.* **2014**, *53* (11), 2923–2926. <https://doi.org/10.1002/anie.201308599>.
- (81) Knoppe, S.; Dolamic, I.; Bürgi, T. Racemization of a Chiral Nanoparticle Evidences the Flexibility of the Gold-Thiolate Interface. *J. Am. Chem. Soc.* **2012**, *134* (31), 13114–13120. <https://doi.org/10.1021/ja3053865>.
- (82) Jadzinsky, P. D.; Calero, G.; Ackerson, C. J.; Bushnell, D. A.; Kornberg, R. D. Structure of a Thiol Monolayer-Protected Gold Nanoparticle at 1.1 Å Resolution. *Science (80-. )*. **2007**, *318* (5849), 430–433. <https://doi.org/10.1126/science.1148624>.
- (83) Yanagimoto, Y.; Negishi, Y.; Fujihara, H.; Tsukuda, T. Chiroptical Activity of BINAP-Stabilized Undecagold Clusters. *J. Phys. Chem. B* **2006**, *110* (24), 11611–11614. <https://doi.org/10.1021/jp061670f>.
- (84) Zeng, C.; Li, T.; Das, A.; Rosi, N. L.; Jin, R. Chiral Structure of Thiolate-Protected 28-Gold-Atom Nanocluster Determined by X-Ray Crystallography. *J. Am. Chem. Soc.* **2013**, *135* (27), 10011–10013. <https://doi.org/10.1021/ja404058q>.
- (85) Wu, H.-L.; Tsai, H.-R.; Hung, Y.-T.; Lao, K.-U.; Liao, C.-W.; Chung, P.-J.; Huang, J.-S.; Chen, I.-C.; Huang, M. H. A Comparative Study of Gold Nanocubes, Octahedra, and Rhombic Dodecahedra as Highly Sensitive SERS Substrates. *Inorg. Chem.* **2011**, *50* (17), 8106–8111. <https://doi.org/10.1021/ic200504n>.

## Chapter 2. Aqueous based Seed-mediated Synthesis of Chiral Nanoparticle

### 2.1 Surface Free Energy and Mechanistic Understanding of Shape-controlled Nanoparticle Synthesis

In order to manipulate the morphology of nanoparticle, consideration of surface energy is the most fundamental aspect. The final morphology of nanoparticle is determined by controlling relative growth rate of each crystallographic plane. In the process controlling the relative growth rate, surface energy of specific plane plays a major role to decide the directional favorability of nanoparticle growth. The surface energies of planes are expressed by the Gibbs free energy per unit area. The total Gibbs free energy of a nanoparticle can be expressed in a very simplified form as shown in below equation.

$$dG = dG_{bulk} + \gamma dA$$

The summation of Gibbs free energy of the bulk material and the surface free energy could express the total Gibbs free energy where  $\gamma$  refers to specific surface free energy per unit area and  $A$  refers to the surface area. The specific surface free energy of crystallographic plane could be expressed as below shown relationship.

$$\gamma = \frac{1}{2} N_B \epsilon \rho_A$$

The  $N_B$  term refers to the number of broken bonds per surface unit cell,  $\epsilon$  refers to the bond strength,  $\rho_A$  refers to the number of surface atoms per unit area. In this relationship, the surface free energy ( $\gamma$ ) can be physically understood as the

increase of free energy per unit area when a new surface is created. Each crystallographic planes have different surface free energies because each material has unique intrinsic anisotropy in atomic arrangements. In the case of materials with face-centered cube (fcc) lattice, the specific surface free energy of planes shows following order:

$$\gamma_{111} < \gamma_{100} < \gamma_{110}$$

The surface energy of a specific crystallographic plane differs from each other and atomic bonds between atoms need to be broken in order for a new surface to be created. Analogically, the surface free energy represents the total cost in energy to break the bonds between atoms which is determined by the number and strength of bonds involved. As shown in Figure 2.1, respect to the exposed crystallographic plane at the incident of atom deposition, the number of newly created bonds are determined by the atomic arrangement of that plane. For the (110) plane, one additional broken bond from the subsurface (labeled as a' and b') is required because it has a role in the formation of two (110)-type surfaces. Therefore, this surface exhibit higher surface energy than other (111) or (100) surface.

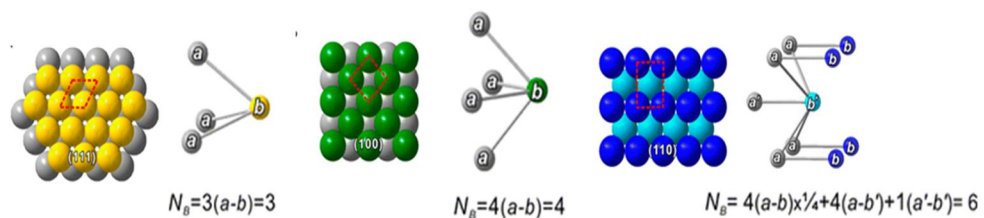


Figure 2. 1 Low-index planes in a face-centered-cubic(fcc) metal and number of bonds per surface unit cell ( $N_B$ ) that have to be broken in creating a pair of new surfaces. The red dashed box represents the surface unit cell for each crystallographic plane.

During the growth of nanoparticle, metal ion is reduced to become an atom and this atom is deposited on to the nanoparticle. This growth of a nanoparticle could be categorized into two process which determines the final morphology of nanoparticle. The first process is the deposition step which reduced metal ions deposit onto the surface of existing nanoclusters or nanoparticles. The second process is diffusion of deposited atoms which deposited atoms move around the surface of nanoparticle to find thermodynamically stable position. In the case which atom diffusion is dominating, atoms favorably migrate to the lowest surface free energy (global minimum) site to result in equilibrium shape. This type of nanoparticle growth is called thermodynamic controlled or surface free energy determined nano-morphology. However, as shown in figure 2.2, control of the surface diffusion kinetic prevents further diffusion towards global minimum but to stay at local minima, which results in relatively unstable morphologies in thermodynamic perspective. This clearly indicates that the growth pathway of nanoparticle and their final morphology could be very well be controlled by the ratio between the atom deposition rates and surface diffusion rate. For example, a cubic morphology should promote addition of atoms onto the corners of nanoparticle due to higher energy of these sites. Upon deposition of atoms, there are two possible options for adatoms: depositing at the corner site and staying there or diffusing to different sites for more thermodynamically favorable situation. By controlling this deposition kinetic and diffusion kinetic, it is possible to control the final position of atoms.

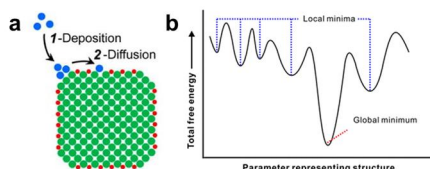


Figure 2. 2 Schematic illustration showing (a) two growth processes (b) total free energy plot depending on the structure

In more detail, the deposition kinetic is directly correlated with the rate which the newly formed metal atoms are supplied to the growth environment. This metal atom supply rate is strictly controlled by the reduction rate (V) of a metal precursor (A) by a reducing agent (B) as described in the following equation:

$$V = k[A]^x[B]^y$$

where [A] and [B] are the molar concentrations of metal precursor and reducing agent, respectively. Furthermore, exponents x and y indicate the reaction orders with respect to metal precursor and reducing agents, and k indicate the rate constant of the reduction reaction which is strongly dependent on synthesis temperature. Therefore, there are multiple variables which could affect the rate of deposition such as, type or concentration of metal precursor, type or concentration of reducing agent, and reaction temperature.

The surface diffusion kinetic could be understood in the following form where the diffusion coefficient D expressed as an Arrhenius-type equation:

$$D = D_0 \exp(-E_{diff}/RT)$$

In this relationship,  $D_0$  indicate the diffusion pre-exponential factor,  $E_{diff}$  indicate the potential energy barrier to diffusion of atoms, R indicate the ideal gas constant, and T is the absolute temperature. For the control of  $E_{diff}$ , there are multiple aspect to control this value; affinity between the surface atom and the adatom, the crystallographic plane of the surface which determines the energetic stability, the accessibility of the surface towards adatoms, and the chemical potential gradient. By carefully modulating these variables, it is possible to design and experimentally achieve the desired nano-morphology.

In this work, we intend to focus on control of chirality evolution in gold

nano-morphology, prepared by aqueous based seed-mediated methods. The scope of this thesis is controlling the nanoparticle morphology, especially chiral morphology of the nanoparticles, and how to selectively and strategically control the chiroptic properties. Therefore, in this chapter, we will review general variables involved during the aqueous based seed mediated methods, and how these factors are individually and cooperatively involved in construction of nanoparticle with chiral morphology.

## 2.2 Capping Agent and Organic Additives

### Capping Agent

Not only limited in the aqueous based nanoparticle synthesis condition but also in general chemical approach for nanoparticle synthesis, capping agent serves a critical role in controlling stability and morphology. The stability of dispersed nanoparticle is directly related with repulsive and attractive interactions between particles. The repulsive interaction between nanoparticle can be originated from charged particles electric double layer or from the steric repulsion of organic layer encapsulating nanoparticles. For shape control during chemical synthesis, molecular capping agents selectively adsorb to specific crystal planes to control exposed crystallographic plane. One of the most efficient but also a general strategy to promote shape anisotropy during nanoparticle growth is by utilization of these capping agents or additives to stabilize a particular facet.

Early chemical synthesis methods to control nano-morphology were characterized by utilizing pre-existing of self-forming fluxional structures such as micro-emulsions, micelles and vesicles, and reverse micelles that were provided to behave as reactors or templates during synthesis.<sup>1-3</sup> These so-called soft template methods are composed of various types of molecules such as liquid crystals, block copolymers, and large biological molecules. In the case where  $\text{HAuCl}_4$  or  $\text{AgNO}_3$  were used as metal ion sources, soft templating was typically conducted in aqueous environment with various types of surfactant molecules such as cetyltrimethylammonium bromide (CTAB), sodium dodecylsulfate (SDS), or bis(2-ethylhexyl) sulfosuccinate (AOT).<sup>4-6</sup> Due to their hydrophilic head group and a hydrophobic tail, surfactants naturally self-assemble into micelles in water with specific orientations such as spherical or rod like. Such generated structures induce directionality towards nanoparticle growth which metal reduction is

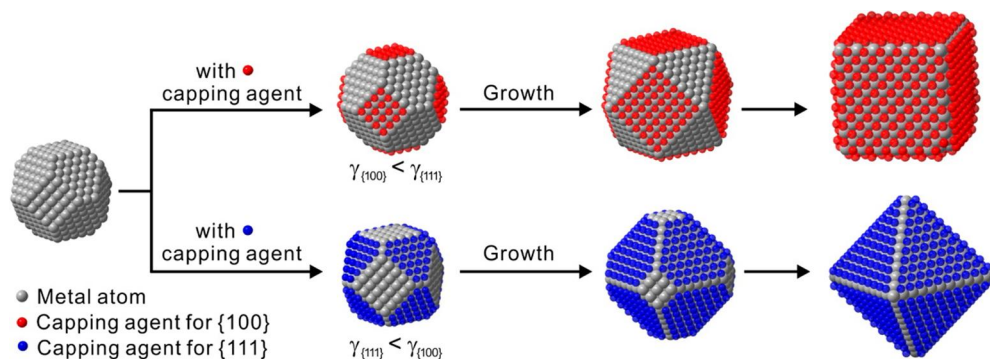


Figure 2. 3 Schematic image explaining the effect of capping agents on the surface energy and final nanoparticle morphology.

conducted in or around the spatially confined hydrophilic volume. These shapes or orientation of micelle formation is related with surfactant concentration, types of surfactants, or number of surfactants used.

Aside from soft templating for morphology control, capping agents could directly affect the nanoparticle morphology through strong interactions with nanoparticle surface. Especially, halides ( $\text{Cl}^-$ ,  $\text{Br}^-$ ,  $\text{I}^-$ ) from molecules and the surface of the NPs shows a very specific adsorption kinetic which each halide promotes different facets during nanoparticle development.<sup>3,7-11</sup> These change in affinity respect to attached halide ions on capping agent selectively attach to a specific facet to promote elongation and generation of specific surface and control overall morphology as shown in figure 2.3.<sup>7</sup> Poly(vinyl pyrrolidone) (PVP) is another well-known capping agent to control the shape of nanoparticles. Generally, PVP is added in the beginning of the synthesis and it is continuously existing during metal reduction. The PVP serves following two roles during nanoparticle shape control; it acts as a stabilizing agent to prevent aggregation of nanoparticles for uniform colloidal dispersion, and it is used as a shape-control agent to promote reduction of metal ions onto a specific crystal face to result in a very specific final

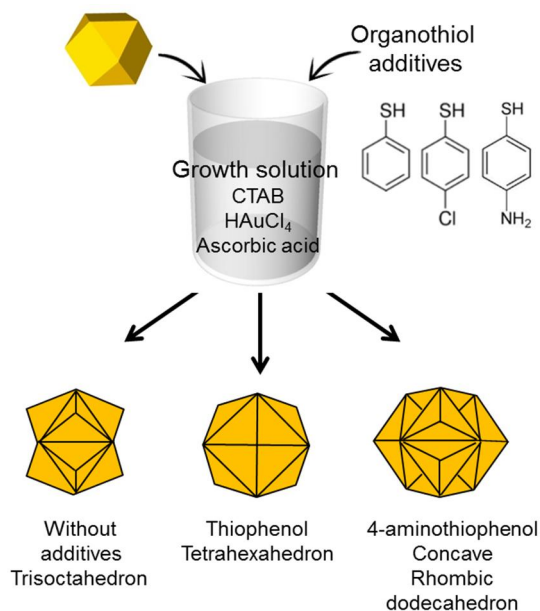


Figure 2. 4 Growth procedure of nanoparticles with morphology controlled by introduction of benzenethiol based modifiers.

nanoparticle morphology. For the fcc crystal system based noble metals, PVP has been known to preferentially bind to the  $\{111\}$  and  $\{100\}$  planes which results in stabilization of the lowest-energy crystal facets to generate structures composed of  $\{111\}$ ,  $\{100\}$ , and  $\{110\}$  planes.<sup>12-15</sup> In the case of other chemical nanoparticle synthesis method, adsorption of functional or coordinating groups for stabilization of different crystal planes of nanoparticles is not restricted to small molecules. For example, some solvents with functional or coordinating groups such as N,N-dimethylformamide (DMF) and ethylene glycol provide adsorption dependent facet and morphology control.<sup>16,17</sup>

### Additives

Aside from capping agents, organic additives also serve as an effective reagent for the shape control of nanoparticles due to their specific affinity towards

certain crystal facets. Adsorbed additives dynamically function on nanoparticle surface to reduce their surface energy and modulate growth rate of specific facets respect to that of other existing facets to ultimately determine final morphology. In order for effective application of organic additives to selectively control nanoparticle morphology, the adsorption ability and stability of the functional or coordinating groups should be well considered prior to use. Representative functional or coordinating groups on to noble metals range from small molecules to larger polymers such as hydroxyl groups,<sup>18</sup> amine groups (primary, secondary and tertiary amine groups),<sup>19,20</sup> thiol groups,<sup>21</sup> and long alkyl chains. For example, during the heterogeneous overgrowth of Palladium (Pd) on small Platinum (Pt) seed nanoparticles, addition of NO<sub>2</sub> molecule to the synthesis environment has been demonstrated. Addition of NO<sub>2</sub> selectively stabilizes the {111} facet of the Pd nano-shell with increasing ratios of NO<sub>2</sub> to which results in Pd grown nanoparticle with increased ratio of {111} to {100} surface facets. Without the addition of NO<sub>2</sub>, Pd nanocubes have been synthesized while addition of NO<sub>2</sub> and control of its concentration in the reaction environment resulted in synthesis of Pd cuboctahedra to Pd octahedral. The selective morphology directing ability is known to be originated from NO<sub>2</sub> being a strong oxidizer, which to promote selective interaction with various Pd crystal planes.<sup>22</sup>

Among organic additives, additives which contains thiol groups are especially highlighted with their exceptional affinity towards noble metal surfaces and in particular to gold (approx. 200 kJ mol<sup>-1</sup>).<sup>23,24</sup> This chemisorption on metal nanoparticle, especially gold surface is significantly strong, therefore, thiol group has been used as a tool for functionalization of gold nanostructures. These strong interaction suggests that organothiol attached on the surface of gold nanoparticle can be used in shape control. Representatively, benzenthio group as a shape controlling additive has been demonstrated to show organothiol based nanoparticle morphology.<sup>25</sup> The nanoparticle was prepared by a modified seed-mediated method

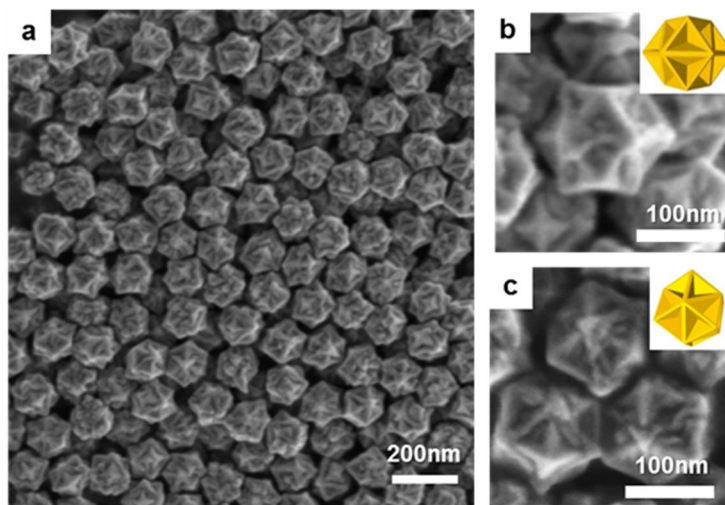


Figure 2. 5 Morphological characterization of the concave rhombicdodecahedron (RD). (a) large-area SEM image of the concave RD. (b-c) High-magnification SEM images of a single nanoparticle with models projecting along (b) [110] and (c) [111].

as described in figure 2.4. With hexadecyltrimethyl ammonium bromide (CTAB) and gold (III) chloride trihydrate ( $\text{HAuCl}_4$ ) were mixed in the growth solution to form the  $\text{AuBr}_4^-$  complex, addition of ascorbic acid reduced the complex to  $\text{Au}^+$ . To this growth condition, various types of benzenethiol molecules were added as shape modifiers and pre-synthesized seen nanoparticles were introduced. The strong Au-S bonding provided a stable anchoring for the benzenethiol molecules to direct the growth of nanoparticle while changing the type of thiol-based organic molecules resulted in different shapes of nanoparticles. Among various morphologies, 4-aminothiophenol (4-ATP) produced the most complex and intriguing structures of concave RD with multiple high-index facets as shown in figure 2.5.<sup>25</sup> This introduced example of thiol-based organic additive for nanoparticle morphology control has opened up a new paradigm for nanoparticle morphology control as it widens the available shape control agents during chemical synthesis of nanoparticles.

Non-organic additives are also used to control the nanoparticle morphology. Trace amounts of metal ions can be used to control nanoparticle morphology by often operating as a capping agent to prevent deposition on certain nanoparticle facets such as of  $\{111\}$  to  $\{100\}$ . In the polyol synthesis of Au and Pt nanostructures, final nanoparticle morphology was determined by addition of  $\text{AgNO}_3$  to the synthesis environment. Small amount of Ag impurities added, for example approximately 1:100 of  $[\text{Ag}^+]:[\text{Au}^{3+}]$  ratio, strongly affected nanoparticle morphology to yield homogenous Au nanocubes.<sup>26</sup> This foreign metal ion influence was more systematically observed during Pt nanoparticle synthesis, where increase of Ag impurity concentration in the synthesis batch resulted in completely altered nano-morphology. With minimal addition with around 1:100 of  $[\text{Ag}^+]:[\text{Pt}^{2+}]$  ratio or no addition of  $\text{Ag}^+$  ions added to the Pt polyol reaction, cubic morphology bounded completely by  $\{100\}$  facets are synthesized. However, with the increase of  $\text{Ag}^+$  ions concentrations to 1:10 or 1:3, cuboctahedral and octahedral nanoparticles were synthesized, respectively. This clearly indicates the increase of Ag during Pt nanoparticle growth promotes generation of  $\{111\}$  facets. This metal ion impurity effect indicates that during metal nanoparticle synthesis systems, foreign metal ions such as  $\text{Ag}^+$  could limit or enhance growth of particular crystallographic directions to control final morphologies.

## 2.3 Reducing Agent and Its Interplay with Capping Agent

For the controlled nanoparticle synthesis, there needs to a systematic process of converting metal ions to metal atoms. Reducing agents determines the kinetic of nanoparticle deposition which strongly affects the final nanoparticle morphology. As there exists various types of reducing agents, it is important to consider reduction strength to specific metal precursor used, concentration of reducing agent, and reaction temperature depending on the desired morphology.

As mentioned, there exist various types of reducing agents that could turn metal ions into nanoparticles. For example, change in the concentration of reducing agent, trisodium citrate, to gold, different diameter of nanoparticles was achieved.<sup>27</sup> In another example, when sodium borohydride was used for reduction of metal ions, due to its excessively strong reducing capability, a large number of nuclei are formed instantaneously as with the introduction and results in very small particle size about 2 nm. Other reducing agents such hydrazine, ascorbic acid, and hydroxylamine have also been used to prepare different sizes of spherical or morphology controlled nanoparticles in aqueous solution.<sup>28-32</sup> These reducing agents, similar to nanoparticles synthesized using trisodium citrate, showed generation of nanoparticles with larger diameter than 20 nm with high uniformity due to their relatively mild reducing strength. In some cases, poly vinyl pyrrolidone (PVP) can also be used as a reducing agent by direct abstraction of hydrogen atoms from the polymer, organic radical formed by formal process and end hydroxyl groups of PVP. Also, in some cases, sugars have been used as reducing agent to prepare nanoparticles with controllable size ranging from 45 to 380 nm.<sup>33,34</sup> Operating temperature of reducing agent is also important for nanoparticle synthesis. Liz-Marzan group reported the temperature dependent reducing ability of dimethylformamide (DMF).<sup>35</sup> When DMF was the sole source of reducing agent, DMF showed capability to reduce metal precursors. Especially,

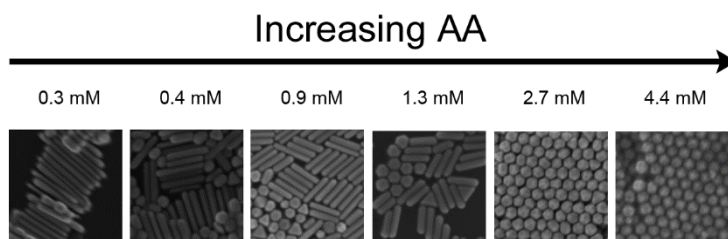


Figure 2. 6 SEM images of gold nanoparticles with varying AA concentration from 0.3 mM to 4.4 mM of AA and fixing CTAB concentration at 15 mM.

the rate of metal precursor reduction was strongly temperature dependent. From above examples, we can see that there exists variety of chemical reducing agent from citrate based reducing agents to sodium borohydride, sugars, and even to DMF.

Controlling the reduction kinetic is strongly related with the nanoparticle morphology. In the chemical synthesis of nanoparticle, the electron source to change metal precursor into nanoparticle is mainly provided from the reducing agent. Therefore, the concentration of reducing agent is directly related to the number of electrons provided to reduce the metal precursor, which affects the kinetic of atom deposition onto existing nanoparticles to ultimately provide a route for shape and size control. Control of reducing strength, through concentration or type variation, could promote anisotropic growth of nanoparticles, as selective generation of certain facets and nanoparticle morphology could be accomplished through intrinsic differences in the growth rates of the chosen reductant. For example, as shown in figure 2.6, while capping agent CTAB was fixed at concentration of 15mM, ascorbic acid concentration has been controlled from 0.3mM to 4.4mM. As shown, nanoparticle morphology was greatly altered from nano-rod formation to rhombic dodecahedral shapes.<sup>36</sup> This shape control through reducing kinetic control, collaborated with capping agent control, could expand

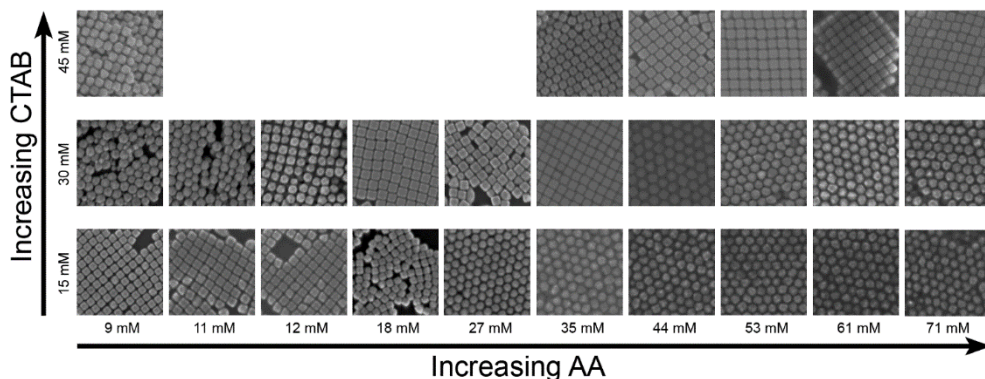


Figure 2. 7 SEM micrographs of gold nanoparticles with varying the concentrations of CTAB and AA, ranging from 9 mM to 71 mM of AA and from 15 mM to 45 mM of CTAB.

the possible morphology to much larger scales. In figure 2.7, variation of surfactant, CTAB molecule and reducing agent, ascorbic acid concentration allows construction of morphology diagram. As shown, by changing concentration of CTAB (15mM, 30mM, and 45mM) and AA (9mM, 11mM, 12mM, 18mM, 27mM, 35mM, 44mM, 53mM, 61mM, and 71mM) controls the final morphology of gold nanoparticle from cuoctahedron to cube to rhombic dodecahedron and to octahedron. For a fixed CTAB concentration, the final shape of gold nanoparticles was strongly controlled by the ascorbic acid concentration. At a fixed CTAB concentration of 15 mM and 30mM, the final shape of nanoparticle was controlled from a cuboctahedron to a cube and finally to a rhombic dodecahedron as the AA concentration increased from 3 mM to 71 mM. To understand this trend of morphology generation, the relationship between AA and CTAB should be considered. While the CTAB molecules are known to stabilize the  $\{100\}$  planes of the gold surface, increase in ascorbic acid concentration accelerates the reduction process of gold ions and promotes kinetic driven nanoparticle morphology. As shown in the morphology diagram, co-existence of CTAB and AA in the growth solution promotes specific crystallographic generation through

specific ratio between two reagents.

## **2.4 Seed-mediated Synthesis of Shape Controlled Nanomaterials**

For the general aqueous based chemical synthesis, nucleation of metal atoms is crucial for obtaining morphology controlled nanoparticles. During this process, formation and addition of small seed particles could serve as nucleation sites for metal ion reduction. This supply of deposition or growth site during nanoparticle growth can determine development of specific crystallographic plane and could drastically change the nanoparticle growth kinetics. Nanoparticle shape control and exposed facet control can be conducted under two mechanisms, homogeneous or heterogeneous nucleation. During the homogeneous nucleation process, in-situ formation of seed nano-clusters serve as seed for nanoparticle growth. This one-pot synthesis of seed and final nanoparticle is more often used as a synthetic strategy for morphology control due to their practical ease. However, in homogeneous nucleation process where one-pot synthesis of nucleation and growth, the ratio of reducing agent to precursor must be carefully modulated to prevent un-wanted secondary nucleation. Therefore, there are limited morphologies that could be generated through homogeneous synthesis method.

On the contrary, heterogeneous nucleation for nano-morphology control, pre-synthesized seed nanoparticles are introduced to the reactant mixture to effectively separate nucleation process and growth process. Therefore, heterogeneous nucleation method is especially advantageous at sophisticated morphology control since the starting seed morphology and facet is predetermined to direct the growth direction as desired. Furthermore, heterogeneous synthesis method has less dependency on the reducing condition due to seed nanoparticles being pre-synthesized and then provided to the growth solution in a separate step. This difference in reducing agent dependency is due to lower activation energy for metal reduction is when atomic deposition occurs directly on an already existing

seed nanoparticle. Therefore, shape control of nanoparticle can be considered as an overgrowth process from the injected seed nanoparticles which allows wider spectrum of shape control through providing more versatile growth conditions.

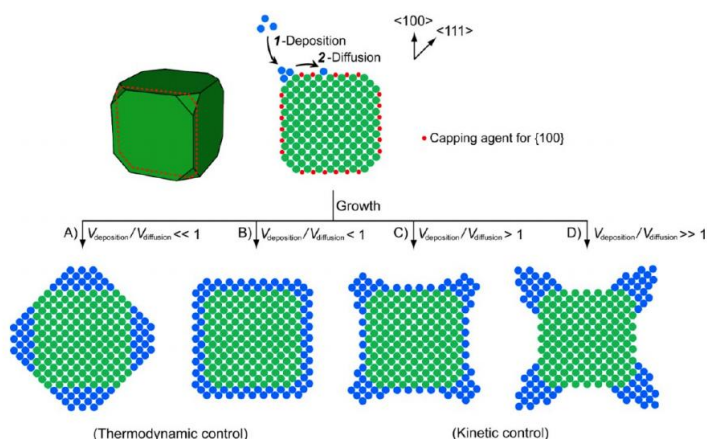


Figure 2. 8 Schematic of seed-mediated nanoparticle synthesis with deposition and diffusion kinetic control for nanoparticle exposed facet and morphology control.

This selective overgrowth process for sophisticated morphology control has been demonstrated under the method called seed-mediated method. Murphy and co-workers have experimentally demonstrated control of final nanoparticle size and shape by applying weak reducing agent to induce selective growth on pre-existing seed nanoparticle.<sup>37,38</sup> Small, 3-5nm in diameter sized Au seed nanoparticles were added to a solution containing Au precursor, CTAB capping agent, and ascorbic acid. For the selection of reducing agent, ascorbic acid was chosen as it is a relatively mild reducing agent which reduces Au(III) in growth solution only to its single oxidation state, Au (I), and not to a gold metal atom. Au(I) form of metal ion then nucleates and deposit on injected seed nanoparticle surface. This deposition step is depicted in figure 2.8, where the example deals with nanoparticle morphology control using {100} facet capping agent. Extend

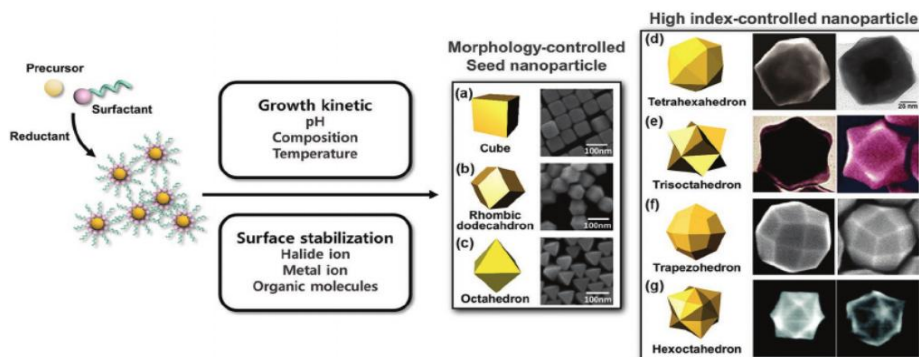


Figure 2. 9 Synthesis of high-index nanoparticles using low-index seed nanoparticles by reaction kinetic and surface stabilization control.

from this method, by carefully modulating the metal atom deposition kinetic respect to the atom diffusion kinetic occurring on top of seed nanoparticle surface, it is possible to synthesize nanoparticles with various morphologies which possess thermodynamically favorable low-index facets to kinetic driven high-index facets. This morphology directing ability of seed-mediated synthesis method could be further tuned by controlling the starting seed morphology. In the case when seed nanoparticles possess well-defined exposed facets and overall morphology, seed-mediated nanoparticle synthesis could result in final nanoparticle morphology with more sophisticated structures.

For example, as shown in figure 2.9, control of nanoparticle morphology using low-index seed nanoparticles such as cube, cuboctahedron, and octahedron are organized and shown. With control of growth kinetic (growth solution pH, reaction temperature, and reducing agent concentration) and surface stabilization agents (Halide ion, metal ion, and organic molecules), various shapes of nanoparticles with thermodynamically unstable high-index facets have been synthesized.<sup>39</sup> These results allow us to have a strong confidence that sequential seed-mediated method for nanoparticle morphology provide a well-established platform for facile nano-morphology control for metal nanoparticle synthesis.

Based on this established system, we have synthesized a 3-dimensional chiral nanoparticle through aqueous based seed-mediated method.

## 2.5 Amino acid and Peptide Induced Chiral Nanoparticle

In amino-acid and peptide induced aqueous based seed-mediated chiral nanoparticle synthesis method, generation of high-index facet is very critical. Generated high-index facets contain chiral kink sites, which their chirality is determined by the orientation of their low-index components as shown in figure 2.10 a).<sup>40,41</sup> In achiral high-index nanoparticles, equal ratio of R and S chiral high-index surface exist throughout the nanoparticle as shown in figure 2.10 b) with the case of  $\{321\}$  bound hexoctahedron nanoparticle.<sup>42</sup>

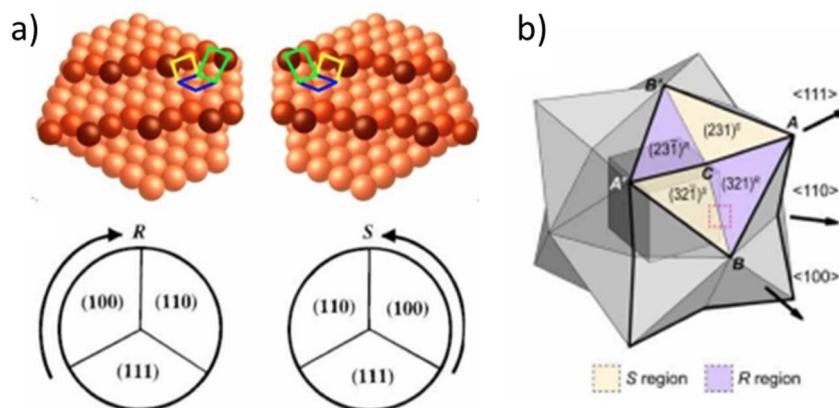


Figure 2. 10 Inorganic surface chirality of kink sites on high-index facets a) schematic surface chirality which chirality is determined by the rotation direction of their low-index components on the kink sites b) distribution of chiral high-index surface on  $\{321\}$  bound hexoctahedron nanoparticle.

Generated chiral surface with high-index surface could selectively interact with chiral molecules. This enantio-specific interaction between chiral molecule and chiral inorganic surface is key to chiral molecule induced chiral nanoparticle synthesis method. As shown in figure 2.11, molecular functional groups in biological system with L or D enantiomer form show different interaction behavior

onto different high-Miller index surfaces. Atomic level interaction between chiral inorganic surface and chiral molecule has been mathematically and theoretically understood that both recognition and generation of chiral kinks in inorganic crystal facets are integral part in developing chiral morphology.<sup>43-45</sup>

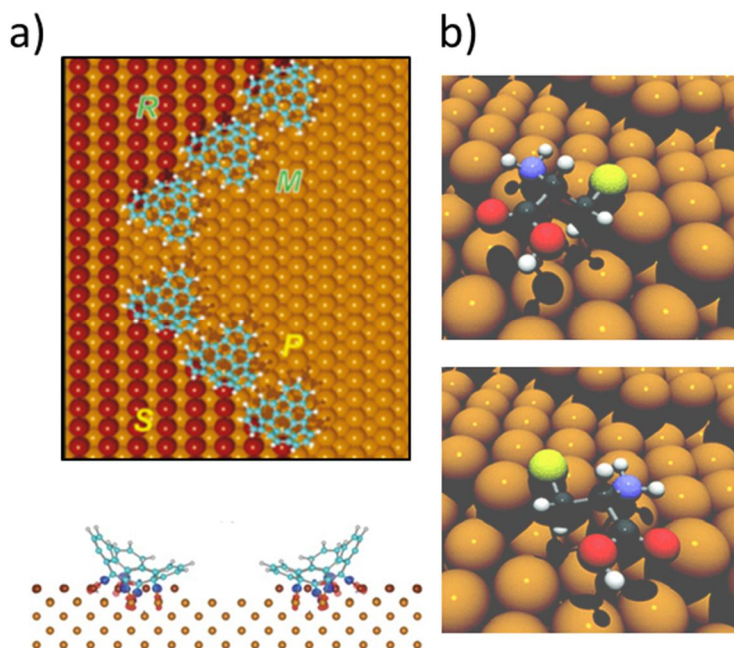


Figure 2. 11 a) Structure model of the observed hemifullerene-decorated steps along  $[3\bar{3}4]$  and  $[3\bar{3}4]$  when M enantiomers decorate R kinks, and P enantiomers decorate S kinks. b) and simulated enantioselective interaction on chiral gold surface which chiral molecule shows different orientation depending on the surface chirality.

In figure 2.12, the schematic procedure of amino-acid and peptide induced chiral nanoparticle synthesis has been presented. As shown, chiral cysteine molecule was added into the growth solution containing  $\text{HAuCl}_4$  gold precursor, CTAB capping agent, ascorbic acid reducing agent, and then 50 nm sized cubic

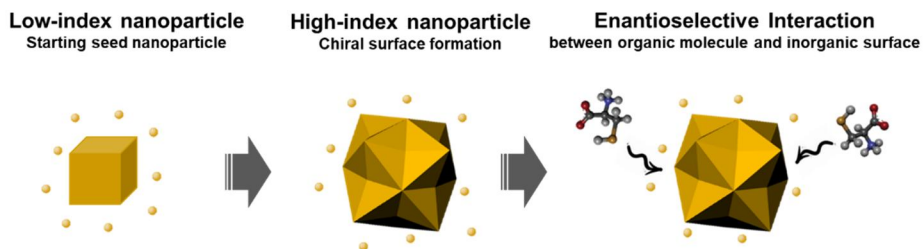


Figure 2. 12 Schematic diagram of chiral nanoparticle synthesis and chirality evolution through introduced chiral molecules.

seed nanoparticle. The reaction was conducted for two hours at room temperature. The cysteine molecule used as the chirality inducer has functional groups with dual roles where the thiol group functions as the anchoring for molecule to tightly bind onto the metal surface and amine based and carboxylic acid based functional groups interacting with metal surface to make characteristic attachment for unique directional nanoparticle growth. Chiral cysteine molecule interacts more selectively with one of the chiral surface at high-index nanoparticle which elongates this surface over the counter chiral surface for asymmetric nanoparticle growth. Through the continuous process of discussed chiral conjugation at atomistic level, it was possible to transform molecular chirality to the inorganic chirality which is exhibited by chiral nanoparticle synthesis from achiral high-index nanoparticle growth condition.

Respect to the chirality of the introduced chiral molecule, the chirality of nanoparticle has been greatly altered. Figure 2.13 shows representative Scanning Electron Microscopy (SEM) images of chiral nanoparticle produced by introduction of L- and D-cysteine. The synthesized chiral nanoparticle shows around 150 ~ 200 nm in the edge length and edges of the cubic boundary nanoparticle shows protruded chiral edges with 4 fold rotation located at each corner. Upon introduction of L-cysteine additive, left handed (LH) chiral

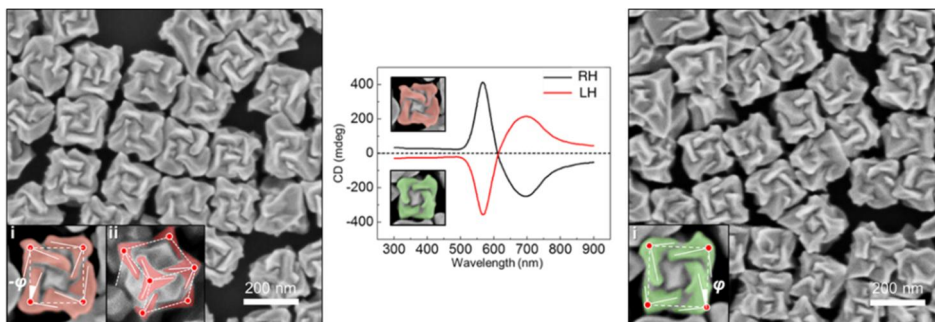


Figure 2. 13 Representative Scanning Electron Microscopy (SEM) images of chiral gold nanoparticles synthesized with L- and D- Cysteine.

structures were fabricated while the counter enantiomer, D-cysteine introduction generated right handed (RH) structures. Each chiral twisted edges show about 100 nm in length and 50 nm width which greatly influence the optical activity range due to sub- light wavelength size scale. Therefore, synthesized nanoparticle shows clear bisignate signal at visible wavelength respect to chirality of input molecule.

Based on this synthesis approach, control of starting seed morphology and the type of chiral molecule allowed synthesis of various chiral nanoparticle morphologies with unique and exceptional chiroptic response at visible wavelength. As shown in figure 2.14, by changing the seed nanoparticle from cubic seed to octahedron or cuboctahedron, and varying the chiral inducing agent type from amino acid to dipeptide and tri-peptide, 5 different chiral nanoparticles have been reported. All of synthesized nanoparticle have 4-fold, 3-fold, and 2-fold symmetry depending on the direction of view point which allowed the naming of the nanoparticles as 432 Helicoid Series. Among 432 Helicoid series, 432 Helicoid III synthesized with glutathione molecule and octahedron seed nanoparticle shows highest chiroptic response of dissymmetric factor, which indicate absolute asymmetry in chiral medium calculated through circular dichroism normalized by total light absorption, equal to 0.2. For more quantified demonstration of

exceptional chiroptic response of 423 Helicoid III, dissymmetric factor comparison chart among reported chiral nanomaterials is displayed in figure 30. <sup>42</sup> As shown, 432 Helicoid III shows highest chiroptic response at visible wavelength and even comparable optical response to some of top-down fabricated method.

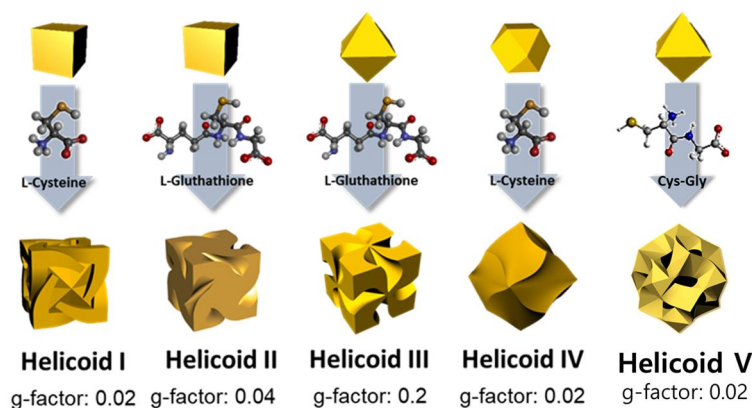


Figure 2. 14 Morphology library of 432 Helicoid Series synthesized with varying seed morphology and chiral inducing molecules.

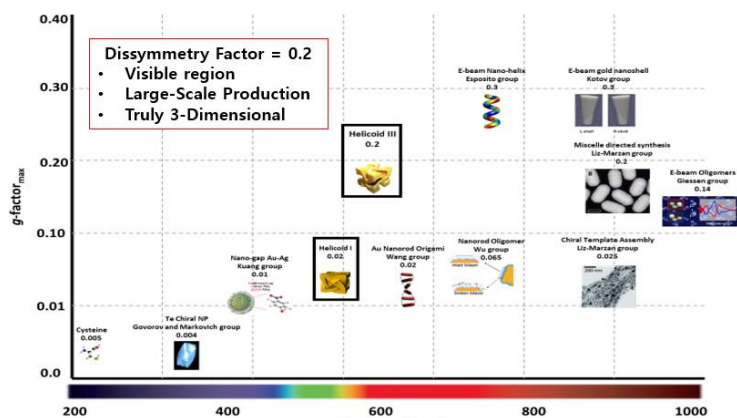


Figure 2. 15 Comparison of dissymmetric factor among reported chiral nanomaterials and 432 Helicoid nanoparticles.<sup>42,46–53</sup>

## 2.6 Objective of Thesis

The primary goal of this work is to develop fundamental understanding of the seed-mediated based chiral nanomaterial synthesis and how to further utilize this synthesis method for more versatile chiral nanomaterials to meet the needs of various potential applications. The novel seed-mediated based chiral nanoparticle synthesis method utilizes the enantioselective interaction between chiral molecule and chiral metal surface. This work focuses on understanding underlying mechanism and influential factors of this process which dictates the chirality evolution. Based on this understanding, systematic enhancement of chiroptic response and synthetic principle for successful expansion of synthesis method has been established. The thesis is categorized by two part, part I is for the systematic enhancement of chiroptic response by uniform chiral gap synthesis, and part II is expansion of synthesis method for more versatile chiral nanomaterials.

In chapter 2, synthetic principle for aqueous based seed-mediated synthesis method has been discussed with overall understanding of constituent elements for the nanoparticle synthesis. Basic theoretical background which determines the generation of low-index to high-index facets on the nanoparticle surface has been discussed. This fundamental understanding of aqueous based seed-mediated morphology control is to understand mechanism of chiral nanomaterial synthesis using seed mediated method, which utilizes the enantioselective interaction between high-index facet and chiral molecules. Also, detailed aqueous based seed-mediated chiral gold nanoparticle synthesis method is explained.

In chapter 3, detailed experimental procedures to control chirality of nanoparticles have been discussed. Also, methods to analyze the synthesized nanoparticles have been discussed in this section

In Part 1, systematic control of chirality evolution to enhance the overall

chiroptical response has been discussed. Chapter 4 discusses the quantitative assessment of synthetic quality of current synthesis system and nanoparticle. The current chiroptic response of 432 helicoid exceeds many of bottom-up synthesis method and it is very much comparable to few top-down method synthesized nanostructures. However, the chiroptic response is currently observed by the solution ensemble stage, which indicates that average chiroptic response of nanoparticles with morphology, size, and CPL irradiation angle variation. This average optical response could not fully represent the full potential of 432 helicoid nanoparticles and requires single nanoparticle level optical analysis. Therefore, single nanoparticle level dark-field scattering analysis of chiral gold nanoparticle has been conducted. We have experimentally demonstrated that 432 helicoid nanoparticle solution based optical response is indeed average of single nanoparticles. Also, based on the single nanoparticle chiroptic response, we have seen that full potential of 432 helicoid chiroptic response is diminished by averaging of well-defined chiral nanoparticles and deformed nanoparticles. Therefore, we have learned that in order to selectively enhance chiroptic response of 432 helicoid, we need to ensure uniform chiral gap development. In this sense, in chapter 5, we have conducted kinetic parameter analysis and mechanistic study to understand chemical variables for efficient chirality evolution and defined the growth regime in to two sector to justify required synthetic condition. Kinetic parameter study allowed lessons of how individual reagents involved in synthesis affects the chirality evolution. Mechanistic study of 432 helicoid growth has been analyzed by time-variant optical and morphological evolution. Two regimes of growth, lateral growth regime and vertical growth regime, requires different growth environment. Therefore, instead of controlling chirality evolution with only controlling the initial synthetic condition, we have divided the growth into two chirality evolution steps which is named as multi-chirality evolution steps. By providing required synthetic conditions for uniform chiral nanoparticle synthesis during each chirality evolution steps, final chiroptic response of 432 helicoid III has

been enhanced by 50%. The enhancement of chiroptic response has been attributed to increase in synthetic uniformity of nanoparticle by quantitative morphology analysis and optical analysis.

In Part 2, fundamental understanding of efficient and controlled expansion of devised aqueous seed-mediated chiral gold nanoparticle synthesis method has been established. Possibility and design constraints to consider for utilization of different chiral inducing agent or different noble metal has been demonstrated. Chiral nanomaterials have versatile applications in research areas such as meta-display applications, chiral sensing, or heterogeneous enantioselective catalysis. In chapter 6, chiral nanomaterial synthesis using single-stranded DNA molecule has been presented. In order for applications of chiral nanomaterials with specifically desired optical properties, it is required to efficiently modulate chiroptic responses. In this sense, moving from amino acid and peptide level chiral nanomaterial generation to sequence programmable oligomer is required. DNA molecule are easily programmable and each nucleobases of DNA has distinguishable interaction behavior with gold surface, which could potentially be utilized to enable programming of desired chiroptic properties. Therefore, effect of Thymine oligomer on chirality evolution of 432 helicoid II using glutathione molecule has been tested. thymine oligomer assisted 432 helicoid II showed enhanced chiroptic response while thymine itself did not induce any chirality. Furthermore, chirality evolution using only the ssDNA oligomer has been tested. Synthesis of chiral gold nanoparticle using Adenine sequence showed chirality evolution in wide oligomer concentration range while other nucleobases did not induce any chirality. This adenine specific chirality evolution was supported through simulation which indicated highest enantiospecific interaction between nucleobase and high-index surface. Control of sequence length on resulting chiroptic response has been experimentally demonstrated and also been supported with simulation which showed increasing enantiospecificity of adenine as number of Adenine involved in

calculation increased. In order to fully understand the effect of adenine on chirality evolution, morphology analysis, time-variant study, and surface chemistry study has been conducted. Furthermore, in order to test the viability of programmable chiral nanoparticle for versatile applications, chiral gold nanoparticle synthesis using sequence patterned with adenine and cytosine in has been demonstrated. Synthesized nanoparticles with different sequence pattern showed various chiroptic response. In chapter 7, expansion of synthesis method to different noble metal has been demonstrated. As potential field of chiral nanomaterials application is vast, extension of material spectrum for the synthesis method to non-plasmonic materials are crucial. Palladium is an ideal choice for this due to its exceptional catalytic property while synthetic system is very similar to that of gold. Chiral palladium synthesis on gold cubic seed was conducted with modified 432 helicoid I synthesis method which reducing kinetic was further reduced to induce uniform hetero-epitaxial growth of palladium on gold. Chiral palladium nanoparticles show spiral structures on each six cubic planes which spiral rotation direction is determined by the chirality of input cysteine molecule. While chiral gold nanoparticle induces high yield of uni-directional chiral nanoparticles, chiral palladium nanoparticle showed increase in ratio of clockwise or counter-clockwise spiral structure depending on the chirality of cysteine molecule. In order to observe the developmental stage of chiral palladium nanoparticle, time-variant morphology analysis has been conducted.

We believe this fundamental understanding of factors influencing chirality evolution during aqueous seed-mediated method and establishing ground rules for efficient expansion of current synthesis method, generation of more unique and dynamic chiral nanomaterials for versatile application is possible.

## 2.7 Bibliography

- (1) Kresge, C. T.; Leonowicz, M. E.; Roth, W. J.; Vartuli, J. C.; Beck, J. S. Ordered Mesoporous Molecular Sieves Synthesized by a Liquid-Crystal Template Mechanism. *Nature* **1992**, *359* (6397), 710–712. <https://doi.org/10.1038/359710a0>.
- (2) Taleb, A.; Petit, C.; Pileni, M. P. Synthesis of Highly Monodisperse Silver Nanoparticles from AOT Reverse Micelles: A Way to 2D and 3D Self-Organization. *Chem. Mater.* **1997**, *9* (4), 950–959. <https://doi.org/10.1021/cm960513y>.
- (3) Shchukin, D. G.; Sukhorukov, G. B. Nanoparticle Synthesis in Engineered Organic Nanoscale Reactors. *Adv. Mater.* **2004**, *16* (8), 671–682. <https://doi.org/10.1002/adma.200306466>.
- (4) Xie, Y.; Kocaeefe, D.; Chen, C.; Kocaeefe, Y. Review of Research on Template Methods in Preparation of Nanomaterials. *J. Nanomater.* **2016**, *2016*, 1–10. <https://doi.org/10.1155/2016/2302595>.
- (5) Liu, J.; Yang, T.; Wang, D.-W.; Lu, G. Q.; Zhao, D.; Qiao, S. Z. A Facile Soft-Template Synthesis of Mesoporous Polymeric and Carbonaceous Nanospheres. *Nat. Commun.* **2013**, *4* (1), 2798. <https://doi.org/10.1038/ncomms3798>.
- (6) Fang, J.; Zhang, L.; Li, J.; Lu, L.; Ma, C.; Cheng, S.; Li, Z.; Xiong, Q.; You, H. A General Soft-Enveloping Strategy in the Templating Synthesis of Mesoporous Metal Nanostructures. *Nat. Commun.* **2018**, *9* (1), 521. <https://doi.org/10.1038/s41467-018-02930-9>.

- (7) Xia, Y.; Xia, X.; Peng, H.-C. Shape-Controlled Synthesis of Colloidal Metal Nanocrystals: Thermodynamic versus Kinetic Products. *J. Am. Chem. Soc.* **2015**, *137* (25), 7947–7966. <https://doi.org/10.1021/jacs.5b04641>.
- (8) Kasture, M.; Sastry, M.; Prasad, B. L. V. Halide Ion Controlled Shape Dependent Gold Nanoparticle Synthesis with Tryptophan as Reducing Agent: Enhanced Fluorescent Properties and White Light Emission. *Chem. Phys. Lett.* **2010**, *484* (4–6), 271–275. <https://doi.org/10.1016/j.cplett.2009.11.052>.
- (9) Nguyen, T.-D.; Do, T.-O. Size- and Shape-Controlled Synthesis of Monodisperse Metal Oxide and Mixed Oxide Nanocrystals. In *Nanocrystal*; InTech, 2011. <https://doi.org/10.5772/17054>.
- (10) Sun, M.; Ran, G.; Fu, Q.; Xu, W. The Effect of Iodide on the Synthesis of Gold Nanoprisms. *J. Exp. Nanosci.* **2015**, *10* (17), 1309–1318. <https://doi.org/10.1080/17458080.2014.1003340>.
- (11) Zhang, J.; Wan, L.; Liu, L.; Deng, Y.; Zhong, C.; Hu, W. PdPt Bimetallic Nanoparticles Enabled by Shape Control with Halide Ions and Their Enhanced Catalytic Activities. *Nanoscale* **2016**, *8* (7), 3962–3972. <https://doi.org/10.1039/C5NR05971B>.
- (12) Koczur, K. M.; Mourdikoudis, S.; Polavarapu, L.; Skrabalak, S. E. Polyvinylpyrrolidone (PVP) in Nanoparticle Synthesis. *Dalt. Trans.* **2015**, *44* (41), 17883–17905. <https://doi.org/10.1039/C5DT02964C>.
- (13) Grzelczak, M.; Pérez-Juste, J.; Mulvaney, P.; Liz-Marzán, L. M. Shape Control in Gold Nanoparticle Synthesis. *Chem. Soc. Rev.* **2008**, *37* (9),

1783. <https://doi.org/10.1039/b711490g>.

- (14) Chen, Z.; Chang, J. W.; Balasanthiran, C.; Milner, S. T.; Rioux, R. M. Anisotropic Growth of Silver Nanoparticles Is Kinetically Controlled by Polyvinylpyrrolidone Binding. *J. Am. Chem. Soc.* **2019**, *141* (10), 4328–4337. <https://doi.org/10.1021/jacs.8b11295>.
- (15) Xia, Y.; Xiong, Y.; Lim, B.; Skrabalak, S. E. Shape-Controlled Synthesis of Metal Nanocrystals: Simple Chemistry Meets Complex Physics? *Angew. Chemie Int. Ed.* **2009**, *48* (1), 60–103. <https://doi.org/10.1002/anie.200802248>.
- (16) Chen, Y.; Gu, X.; Nie, C.-G.; Jiang, Z.-Y.; Xie, Z.-X.; Lin, C.-J. Shape Controlled Growth of Gold Nanoparticles by a Solution Synthesis. *Chem. Commun.* **2005**, No. 33, 4181. <https://doi.org/10.1039/b504911c>.
- (17) Hai, C.; Li, S.; Zhou, Y.; Zeng, J.; Ren, X.; Li, X. Roles of Ethylene Glycol Solvent and Polymers in Preparing Uniformly Distributed MgO Nanoparticles. *J. Asian Ceram. Soc.* **2017**, *5* (2), 176–182. <https://doi.org/10.1016/j.jascer.2017.04.004>.
- (18) Wang, L.; Liu, Y.; Li, W.; Jiang, X.; Ji, Y.; Wu, X.; Xu, L.; Qiu, Y.; Zhao, K.; Wei, T.; et al. Selective Targeting of Gold Nanorods at the Mitochondria of Cancer Cells: Implications for Cancer Therapy. *Nano Lett.* **2011**, *11* (2), 772–780. <https://doi.org/10.1021/nl103992v>.
- (19) Sau, T. K.; Murphy, C. J. Room Temperature, High-Yield Synthesis of Multiple Shapes of Gold Nanoparticles in Aqueous Solution. *J. Am. Chem. Soc.* **2004**, *126* (28), 8648–8649. <https://doi.org/10.1021/ja047846d>.

- (20) Yu, Chang, S.-S.; Lee, C.-L.; Wang, C. R. C. Gold Nanorods: Electrochemical Synthesis and Optical Properties. *J. Phys. Chem. B* **1997**, *101* (34), 6661–6664. <https://doi.org/10.1021/jp971656q>.
- (21) Torigoe, K.; Esumi, K. Preparation of Colloidal Gold by Photoreduction of Tetracyanoaurate(1-)-Cationic Surfactant Complexes. *Langmuir* **1992**, *8* (1), 59–63. <https://doi.org/10.1021/la00037a013>.
- (22) Xu, X.; Cortie, M. B. Shape Change and Color Gamut in Gold Nanorods, Dumbbells, and Dog Bones. *Adv. Funct. Mater.* **2006**, *16* (16), 2170–2176. <https://doi.org/10.1002/adfm.200500878>.
- (23) Spampinato, V.; Parracino, M. A.; La Spina, R.; Rossi, F.; Ceccone, G. Surface Analysis of Gold Nanoparticles Functionalized with Thiol-Modified Glucose SAMs for Biosensor Applications. *Front. Chem.* **2016**, *4*. <https://doi.org/10.3389/fchem.2016.00008>.
- (24) Xue, Y.; Li, X.; Li, H.; Zhang, W. Quantifying Thiol–Gold Interactions towards the Efficient Strength Control. *Nat. Commun.* **2014**, *5* (1), 4348. <https://doi.org/10.1038/ncomms5348>.
- (25) Lee, H.-E.; Yang, K. D.; Yoon, S. M.; Ahn, H.-Y.; Lee, Y. Y.; Chang, H.; Jeong, D. H.; Lee, Y.-S.; Kim, M. Y.; Nam, K. T. Concave Rhombic Dodecahedral Au Nanocatalyst with Multiple High-Index Facets for CO<sub>2</sub> Reduction. *ACS Nano* **2015**, *9* (8), 8384–8393. <https://doi.org/10.1021/acsnano.5b03065>.
- (26) Kim, F.; Connor, S.; Song, H.; Kuykendall, T.; Yang, P. Platonic Gold Nanocrystals. *Angew. Chemie Int. Ed.* **2004**, *43* (28), 3673–3677. <https://doi.org/10.1002/anie.200454216>.

- (27) Tyagi, H.; Kushwaha, A.; Kumar, A.; Aslam, M. A Facile PH Controlled Citrate-Based Reduction Method for Gold Nanoparticle Synthesis at Room Temperature. *Nanoscale Res. Lett.* **2016**, *11* (1), 362. <https://doi.org/10.1186/s11671-016-1576-5>.
- (28) Medvedeva, X.; Vidyakina, A.; Li, F.; Mereshchenko, A.; Klinkova, A. Reductive and Coordinative Effects of Hydrazine in Structural Transformations of Copper Hydroxide Nanoparticles. *Nanomaterials* **2019**, *9* (10), 1445. <https://doi.org/10.3390/nano9101445>.
- (29) Sun, K.; Qiu, J.; Liu, J.; Miao, Y. Preparation and Characterization of Gold Nanoparticles Using Ascorbic Acid as Reducing Agent in Reverse Micelles. *J. Mater. Sci.* **2009**, *44* (3), 754–758. <https://doi.org/10.1007/s10853-008-3162-4>.
- (30) Malassis, L.; Dreyfus, R.; Murphy, R. J.; Hough, L. A.; Donnio, B.; Murray, C. B. One-Step Green Synthesis of Gold and Silver Nanoparticles with Ascorbic Acid and Their Versatile Surface Post-Functionalization. *RSC Adv.* **2016**, *6* (39), 33092–33100. <https://doi.org/10.1039/C6RA00194G>.
- (31) Xin, J.; Yin, X.; Chen, S.; Wu, A. Synthesis of Uniform and Stable Silver Nanoparticles by a Gold Seed-Mediated Growth Approach in a Buffer System. *J. Exp. Nanosci.* **2014**, *9* (4), 382–390. <https://doi.org/10.1080/17458080.2012.662656>.
- (32) Cheng, Z.-P.; Chu, X.-Z.; Wu, X.-Q.; Xu, J.-M.; Zhong, H.; Yin, J.-Z. Controlled Synthesis of Silver Nanoplates and Nanoparticles by Reducing Silver Nitrate with Hydroxylamine Hydrochloride. *Rare Met.* **2017**, *36* (10), 799–805. <https://doi.org/10.1007/s12598-017-0949-y>.

- (33) Agudelo, W.; Montoya, Y.; Bustamante, J. Using a Non-Reducing Sugar in the Green Synthesis of Gold and Silver Nanoparticles by the Chemical Reduction Method. *DYNA* **2018**, *85* (206), 69–78.  
<https://doi.org/10.15446/dyna.v85n206.72136>.
- (34) Hemmati, S.; Retzlaff-Roberts, E.; Scott, C.; Harris, M. T. Artificial Sweeteners and Sugar Ingredients as Reducing Agent for Green Synthesis of Silver Nanoparticles. *J. Nanomater.* **2019**, *2019*, 1–16.  
<https://doi.org/10.1155/2019/9641860>.
- (35) Pastoriza-Santos, I.; Liz-Marzán, L. M. N, N -Dimethylformamide as a Reaction Medium for Metal Nanoparticle Synthesis. *Adv. Funct. Mater.* **2009**, *19* (5), 679–688. <https://doi.org/10.1002/adfm.200801566>.
- (36) Ahn, H.-Y.; Lee, H.-E.; Jin, K.; Nam, K. T. Extended Gold Nano-Morphology Diagram: Synthesis of Rhombic Dodecahedra Using CTAB and Ascorbic Acid. *J. Mater. Chem. C* **2013**, *1* (41), 6861.  
<https://doi.org/10.1039/c3tc31135j>.
- (37) Jana, N. R.; Gearheart, L.; Murphy, C. J. Evidence for Seed-Mediated Nucleation in the Chemical Reduction of Gold Salts to Gold Nanoparticles. *Chem. Mater.* **2001**, *13* (7), 2313–2322.  
<https://doi.org/10.1021/cm000662n>.
- (38) Jana, N. R.; Gearheart, L.; Murphy, C. J. Seed-Mediated Growth Approach for Shape-Controlled Synthesis of Spheroidal and Rod-like Gold Nanoparticles Using a Surfactant Template. *Adv. Mater.* **2001**, *13* (18), 1389–1393. [https://doi.org/10.1002/1521-4095\(200109\)13:18<1389::AID-ADMA1389>3.0.CO;2-F](https://doi.org/10.1002/1521-4095(200109)13:18<1389::AID-ADMA1389>3.0.CO;2-F).

- (39) Im, S. W.; Ahn, H.; Kim, R. M.; Cho, N. H.; Kim, H.; Lim, Y.; Lee, H.; Nam, K. T. Chiral Surface and Geometry of Metal Nanocrystals. *Adv. Mater.* **2020**, *32* (41), 1905758.  
<https://doi.org/10.1002/adma.201905758>.
- (40) Karagoz, B.; Payne, M.; Reinicker, A.; Kondratyuk, P.; Gellman, A. J. A Most Enantioselective Chiral Surface: Tartaric Acid on All Surfaces Vicinal to Cu(110). *Langmuir* **2019**, *35* (50), 16438–16443.  
<https://doi.org/10.1021/acs.langmuir.9b02476>.
- (41) Ahmadi, A.; Attard, G.; Feliu, J.; Rodes, A. Surface Reactivity at “Chiral” Platinum Surfaces. *Langmuir* **1999**, *15* (7), 2420–2424.  
<https://doi.org/10.1021/la9810915>.
- (42) Lee, H.-E.; Ahn, H.-Y.; Mun, J.; Lee, Y. Y.; Kim, M.; Cho, N. H.; Chang, K.; Kim, W. S.; Rho, J.; Nam, K. T. Amino-Acid- and Peptide-Directed Synthesis of Chiral Plasmonic Gold Nanoparticles. *Nature* **2018**, *556* (7701), 360–365. <https://doi.org/10.1038/s41586-018-0034-1>.
- (43) Dutta, S.; Gellman, A. J. Enantiospecific Equilibrium Adsorption and Chemistry of  $d$ - /  $l$ -proline Mixtures on Chiral and Achiral Cu Surfaces. *Chirality* **2020**, *32* (2), 200–214.  
<https://doi.org/10.1002/chir.23153>.
- (44) Yun, Y.; Gellman, A. J. Enantiospecific Adsorption of Amino Acids on Naturally Chiral Cu<sub>{3,1,17}</sub> R&S Surfaces. *Langmuir* **2015**, *31* (22), 6055–6063. <https://doi.org/10.1021/acs.langmuir.5b00707>.
- (45) Xiao, W.; Ernst, K.-H.; Palotas, K.; Zhang, Y.; Bruyer, E.; Peng, L.; Greber, T.; Hofer, W. A.; Scott, L. T.; Fasel, R. Microscopic Origin of

- Chiral Shape Induction in Achiral Crystals. *Nat. Chem.* **2016**, *8* (4), 326–330. <https://doi.org/10.1038/nchem.2449>.
- (46) Yeom, B.; Zhang, H.; Zhang, H.; Park, J. Il; Kim, K.; Govorov, A. O.; Kotov, N. A. Chiral Plasmonic Nanostructures on Achiral Nanopillars. *Nano Lett.* **2013**, *13* (11), 5277–5283. <https://doi.org/10.1021/nl402782d>.
- (47) Yan, J.; Hou, S.; Ji, Y.; Wu, X. Heat-Enhanced Symmetry Breaking in Dynamic Gold Nanorod Oligomers: The Importance of Interface Control. *Nanoscale* **2016**, *8* (19), 10030–10034. <https://doi.org/10.1039/C6NR00767H>.
- (48) Lan, X.; Lu, X.; Shen, C.; Ke, Y.; Ni, W.; Wang, Q. Au Nanorod Helical Superstructures with Designed Chirality. *J. Am. Chem. Soc.* **2015**, *137* (1), 457–462. <https://doi.org/10.1021/ja511333q>.
- (49) Ben-Moshe, A.; Wolf, S. G.; Sadan, M. B.; Houben, L.; Fan, Z.; Govorov, A. O.; Markovich, G. Enantioselective Control of Lattice and Shape Chirality in Inorganic Nanostructures Using Chiral Biomolecules. *Nat. Commun.* **2014**, *5* (1), 4302. <https://doi.org/10.1038/ncomms5302>.
- (50) Hentschel, M.; Schäferling, M.; Weiss, T.; Liu, N.; Giessen, H. Three-Dimensional Chiral Plasmonic Oligomers. *Nano Lett.* **2012**, *12* (5), 2542–2547. <https://doi.org/10.1021/nl300769x>.
- (51) Mohammadi, E.; Tsakmakidis, K. L.; Askarpour, A. N.; Dekhoda, P.; Tavakoli, A.; Altug, H. Nanophotonic Platforms for Enhanced Chiral Sensing. *ACS Photonics* **2018**, *5* (7), 2669–2675. <https://doi.org/10.1021/acsphotonics.8b00270>.
- (52) Hao, C.; Xu, L.; Ma, W.; Wu, X.; Wang, L.; Kuang, H.; Xu, C.

Photocatalysis: Unusual Circularly Polarized Photocatalytic Activity in Nanogapped Gold-Silver Chiroplasmonic Nanostructures (*Adv. Funct. Mater.* 36/2015). *Adv. Funct. Mater.* **2015**, 25 (36), 5717–5717. <https://doi.org/10.1002/adfm.201570237>.

- (53) González-Rubio, G.; Mosquera, J.; Kumar, V.; Pedraza-Tardajos, A.; Llombart, P.; Solís, D. M.; Lobato, I.; Noya, E. G.; Guerrero-Martínez, A.; Taboada, J. M.; et al. Micelle-Directed Chiral Seeded Growth on Anisotropic Gold Nanocrystals. *Science (80-. )*. **2020**, 368 (6498), 1472–1477. <https://doi.org/10.1126/science.aba0980>.

## Chapter 3. Experimental Procedures

### 3.1 Synthesis of Chiral Gold Nanoparticles

#### Chemicals

Hexadecyltrimethylammonium bromide (CTAB: 99%), sodium borohydride ( $\text{NaBH}_4$ : 99%), L-ascorbic acid (AA: 99%), and tetrachloroauric (III) trihydrate ( $\text{HAuCl}_4 \cdot 3\text{H}_2\text{O}$ : 99.9%) were purchased from Sigma-Aldrich. Also, L-Glutathione ( $\gamma$ -EC-G, 98%, Sigma-Aldrich) was obtained commercially and used without further purification. Palladium(II) chloride ( $\text{PdCl}_2$ : 99.9%) was purchased from Thermo Fisher Scientific and L- and D- Cysteine (98.0%) was purchased from TCI chemical. ssDNA oligomers were purchased from IDT and were used without further purification. All aqueous solutions were prepared using high-purity deionized water (18.2 M $\Omega$ /cm).

#### Multi-chirality-evolution for uniform chiral nanoparticle synthesis

For the use during chiral seed nanoparticle synthesis, octahedral seeds were synthesized as reported previously.<sup>1,2</sup> Before use in synthesis, octahedral seed nanoparticles were centrifuged (6708g, 150 s) twice and dispersed in aqueous CTAB (1 mM) solution. In a typical synthesis condition, a growth solution was prepared by adding 0.8 mL of 100 mM CTAB and 0.1 mL of 5 mM gold chloride trihydrate into 4 mL of deionized water to form a  $[\text{AuBr}_4]^-$  complex.  $\text{Au}^{3+}$  in the growth solution was then reduced to  $\text{Au}^+$  by the rapid injection of 0.475 mL of 50 mM AA solution. The growth of chiral nanoparticles was initiated by adding 5  $\mu\text{L}$  of 2.75 mM GSH solution and 50  $\mu\text{L}$  of octahedral seed solution into the growth solution. The growth solution was placed in a 30 °C bath for 2 h, and the violet solution gradually became pink with large scattering. The solution was centrifuged

one time (1677g, 60 s) to remove unreacted reagents and was redispersed in a 1 mM CTAB solution for further synthesis.

A growth solution was prepared by adding 0.8 mL of 100 mM CTAB and 0.1 mL of 5 mM gold chloride trihydrate into 4 mL of deionized water.  $\text{Au}^{3+}$  was reduced to  $\text{Au}^+$  by the rapid injection of 0.475 mL of 20 mM AA solution. The growth of chiral nanoparticles was initiated by adding 5  $\mu\text{L}$  of 2.75 mM GSH solution and 50  $\mu\text{L}$  of chiral seed solution into the growth solution. The growth solution was placed in a 30 °C bath for 2 h, and the pink solution gradually became blue with large scattering. The solution was centrifuged twice (1677g, 60 s) to remove unreacted reagents and was redispersed in a 1 mM CTAB solution. After synthesis, the synthesized nanoparticles were precipitated by centrifugation (1677g, 60 s). The calculated amount of the stock solution of CTAB, BDAC, and deionized water was added to make the appropriate final concentration (BDAC  $\sim$  5 mM, CTAB  $\sim$  1 mM). The solution was mixed and centrifuged (500g, 300 s). The supernatants were removed and remaining sediments were redispersed in 1 mM CTAB for further characterization.

### 3.2 DNA induced Chiral Gold Nanoparticle Synthesis

Octahedral seeds were synthesized as reported previously.<sup>1,2</sup> Before use, both types of seed nanoparticle were centrifuged (6,708g, 150 s) twice and dispersed in aqueous CTAB (1 mM) solution. In a typical synthesis, a growth solution was prepared by adding 0.8 ml of 100 mM CTAB and 0.1 ml of 10 mM gold chloride trihydrate into 3.95 ml of deionized water to form an  $[\text{AuBr}_4]^-$  complex.  $\text{Au}^{3+}$  was then reduced to  $\text{Au}^+$  by the rapid injection of 0.475 ml of 100 mM AA solution. The growth of chiral nanoparticles was initiated by adding 25  $\mu\text{l}$  of 100 $\mu\text{M}$  single-stranded DNA oligomer and 25  $\mu\text{l}$  of seed solution into the growth solution. The growth solution was placed in a 30 °C bath for 2 h, and the pink solution gradually became blue with large scattering. The solution was centrifuged twice (1,677g, 60 s) to remove unreacted reagents and was re-dispersed in a 1 mM CTAB solution for further characterization.

### 3.3 Chiral Palladium Nanoparticle Synthesis

Chiral Palladium Nanoparticle Synthesis: Palladium precursor,  $\text{H}_2\text{PdCl}_4$ , was prepared by dissolving 0.1773 g of  $\text{PdCl}_2$  in 10 mL of 0.2 M HCl and was further diluted to 100 mL with high-purity deionized water ( $18.2 \text{ M}\Omega \text{ cm}^{-1}$ ).<sup>3</sup> Gold cubic nanoparticle was synthesized as previously reported. Prior to use, seed nanoparticles were centrifuged (6708 g, 150 s) twice and dispersed in aqueous CTAB ( $1 \times 10^{-3} \text{ M}$ ) solution. The growth solution was prepared by adding 125  $\mu\text{L}$  of  $10 \times 10^{-3} \text{ M}$   $\text{H}_2\text{PdCl}_4$  into 4.4 mL of  $10 \times 10^{-3} \text{ M}$  CTAB. Then, 50  $\mu\text{L}$  of gold seed nanoparticle was added to solution. pH of the growth solution was adjusted to 1.76 with prepared 0.5 M  $\text{H}_2\text{SO}_4$  solution. Then,  $4 \times 10^{-3} \text{ M}$  equivalent L-ascorbic acid was added to the growth solution for the reduction of metal precursor. At last,  $1 \times 10^{-6} \text{ M}$  equivalent cysteine was added. The following growth solution was vortexed vigorously then left undisturbed for 3 h in a 40 °C bath. The final solution was centrifuged twice (1677 g, 60 s) to remove unreacted reagents and was re-dispersed in a  $1 \times 10^{-3} \text{ M}$  CTAB solution for further characterization.

## 3.4 Characterization of Chiral Nanostructures

### Scanning Electron Microscopy (SEM)

Scanning electron microscopy (SEM) micrographs were obtained using a Zeiss Supra 55 VP operating at 2 kV. Samples were prepared by dropping colloidal solutions onto silicon wafers. Transmission electron microscopy (TEM) micrographs and selected area electron diffraction (SAED) patterns were obtained using a JEOL JEM-3000F FEG TEM. UV/vis extinction spectra were taken using Thermo Scientific NanoDrop 2000c UV-Vis Spectrophotometer in the 220 – 840 nm wavelength region. X-Ray photoelectron spectroscopy (XPS) experiments were conducted on an ESCALAB 250 instrument equipped with an Al X-ray source and monochromator (Thermo Scientific, UK). The spectra were calibrated with respect to the C-1s binding energy (284.5 eV). The atomic percentages of gold and nitrogen were evaluated from the corresponding areas of the Au-4f<sub>7/2</sub> and N-1s peaks, respectively, as explained in the text, with peak fitting obtained using the ThermoAdvantage software. A JEM 2100F (JEOL, Tokyo, Japan) transmission electron microscope was used to acquire HR-TEM and HADDF-STEM images, operating at 200 kV. For dissection of the nanoparticle, a FEI Helios 650 FIB instrument was used.

### Measuring Uniformity of Chiral Morphology using Statistical Analysis

Individual particle images were obtained by watershed separation from the SEM image. The individual particles were converted into binary images by threshold values. All pixels in the image under the threshold were converted to black (background) and those above the threshold were converted to white (particle). The area of each particle was computed, and the effective cubic edge length was calculated based on the assumption that the particles have a cubic shape. The data were fitted into a normal distribution, and the mean and standard

deviation values were obtained.

### **Circular Dichroism Spectroscopy**

Extinction and circular dichroism (CD) spectra were obtained using a J-815 spectropolarimeter instrument (JASCO), and optical rotatory dispersion (ORD) spectra were measured using an additional ORD attachment.

Kuhn's dis-symmetry factor (g-factor) is a dimensionless quantity that is useful for quantitative comparisons of chiro-optical properties among different systems and was calculated from the measured extinction and CD values using:

$$g\text{-factor} = 2 \frac{A_L - A_R}{A_L + A_R} \propto \frac{\text{CD}}{\text{extinction}}$$

### **Sample Preparation for Single NP Dark-Field Scattering Spectroscopy**

The prepared nanoparticle solution was diluted to 10 vol % with 1 mM CTAB solution. Then, residual CTAB was removed from the diluted particle solution through centrifugation using high-purity deionized water while keeping the final volume constant. We dispensed 200  $\mu\text{L}$  of the diluted nanoparticle solution and dropped it on a marked  $1 \times 1 \text{ cm}^2$  clean glass substrate. Afterward, we spin-coated the solution at 5000 rpm for 30 s to obtain evenly spread nanoparticles with a spacing to prevent optical coupling.

### 3.5 Bibliography

- (1) Ahn, H.-Y.; Lee, H.-E.; Jin, K.; Nam, K. T. Extended Gold Nano-Morphology Diagram: Synthesis of Rhombic Dodecahedra Using CTAB and Ascorbic Acid. *J. Mater. Chem. C* **2013**, *1* (41), 6861. <https://doi.org/10.1039/c3tc31135j>.
- (2) Wu, H.-L.; Tsai, H.-R.; Hung, Y.-T.; Lao, K.-U.; Liao, C.-W.; Chung, P.-J.; Huang, J.-S.; Chen, I.-C.; Huang, M. H. A Comparative Study of Gold Nanocubes, Octahedra, and Rhombic Dodecahedra as Highly Sensitive SERS Substrates. *Inorg. Chem.* **2011**, *50* (17), 8106–8111. <https://doi.org/10.1021/ic200504n>.
- (3) Niu, W.; Li, Z.-Y.; Shi, L.; Liu, X.; Li, H.; Han, S.; Chen, J.; Xu, G. Seed-Mediated Growth of Nearly Monodisperse Palladium Nanocubes with Controllable Sizes. *Cryst. Growth Des.* **2008**, *8* (12), 4440–4444. <https://doi.org/10.1021/cg8002433>.

## Part I. Systematic Chirality Evolution Control for Enhanced Chiroptic Response

In this part of the thesis, we intend to quantitatively and statistically analyze 432 helicoid nanoparticles to assess current synthetic conditions and provide design principle for enhanced chiroptic response. Therefore, single nanoparticle level optical analysis was conducted to find the potential optical response of 432 helicoid nanoparticle and based on this result, ideal direction of research for nanoparticle synthesis with enhanced chiroptic response has been proposed. Based on the proposition, modified and optimized seed-mediated synthesis method has been presented to show enhanced chiroptic response.

## Chapter 4. Single-NP Dark-Field Scattering Analysis of 432 Helicoid Nanoparticles

### 4.1 Introduction

Chirality is a geometrical property which refers to non-superimposable images. The chiral properties receive a significant interest due to its unique interaction with polarized light. Especially, chiral structures using plasmonic materials expanded the applicability of nanophotonics to areas such as negative refractive index material and enantiomeric sensing applications. In the last decade, many profound research achievements on generation of chiral plasmonic structures have been conducted using lithography technique, glanced angle deposition, direct laser writing, and macromolecular templated method.<sup>1-17</sup> While these introduced fabrication methods enabled sophisticated nano-morphology control and resulting optical responses, efforts to simplify the complicated synthetic process and expand potential morphologies were still required. Recently, a novel aqueous based chemical synthesis method for truly three-dimensional chiral gold nanoparticle has been presented.<sup>18,19</sup> During the seed-mediated method, thiol containing peptide additives such as cysteine or glutathione molecules were used as chiral shape modifiers. The enantioselective interaction between generated chiral high-Miller-index surfaces ( $\{hkl\}$ ,  $h \neq k \neq l \neq 0$ ) and the introduced chiral molecules induced an asymmetric growth of a specific enantiomeric surface to ultimately induce asymmetry in overall nanostructures. The introduction of  $L$ -isomer of the peptide induced a clockwise rotation of chiral features while the  $D$ -isomer induced the opposite, an anticlockwise, rotation in the chiral features. Furthermore, control of initial seed morphology and the type of chiral molecule introduced allowed flexible variation of resulting nanoparticle and its chiroptic response. Among total of five types of synthesized nanoparticles, 432 helicoid III nanoparticles,

synthesized using octahedron seed nanoparticle and glutathione molecule, exhibited the highest Kuhn's dissymmetry factor (g-factor) of  $g = 0.20$  at visible wavelength. While the dissymmetric factor of  $g = 0.20$  is exceptionally high for both bottom-up and top-down synthesis method, for more practical application of chiral nanostructures, further improvement in its chiroptic response is required. To do so, at first, quantitative assessment of chiral nanoparticle and fully understanding its current and potential synthetic quality is necessary.

In the context of understanding nanoparticle, one question stood out from the beginning: What would be the ultimate limit of nanoparticle's optical property? What would be the way to maximize the chirality in plasmonic systems? More specifically, what are some of the design principles for enhanced chiroptic response? The answer to these questions are very complicated and requires careful isolation of each causes and variables. In most chiroptic measurement systems, the overall chiral response is expressed through collective effect of number of plasmonic resonances and their energetic splitting, excitation light rotation direction (LCP or RCP), incident angle, structural differences, and more. Therefore, fully understanding and experimentally demonstrating the relation between the nano-morphology and the resulting optical response are considered extremely difficult or even impossible despite its importance in nanophotonics. This is particularly true for chiral morphologies since a very small morphological differences can show significant differences in terms of chiroptic response.<sup>20-27</sup>

## 4.2 Chiral Scatterometry Measurement

Measurement of chiroptical response of the single nanoparticles has been conducted using modified dark-field microscope (Nikon Eclipse TE2000- U).<sup>[x]</sup> A detailed schematic of the optical set up is shown in figure 4.1. We prepared the nanoparticle samples onto the glass substrate and placed the sample at the sample position. By using a high-intensity laser-driven plasma white light source (Energetiq EQ-99) and constructing the polarization set up using a subsequent combination of linear polarizer (Thorlabs LPVIS100) and broadband quarter wave plate (B. Halle RAC 5.4.20), we generated circularly polarized light. The generated left circularly polarized (LCP) and right circularly polarized light (RCP) are focused via a dark-field condenser onto the individual nanoparticles. The dark-field

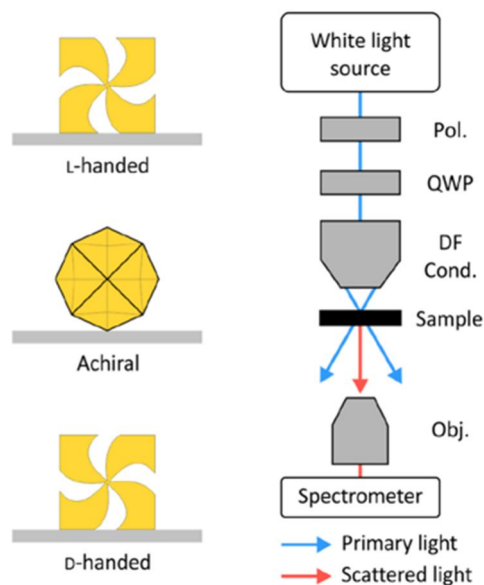


Figure 4. 1 Schematic illustration of single chiral plasmonic NPs showing the left-handed, achiral, and right-handed structure and the optical transmission setup to measure single nanoparticle chiroptical responses.

condenser possesses high numerical aperture ( $NA = 0.8\text{--}0.95$ ) which ensures that only the scattered light in the forward direction (indicated by red lines in Figure 1b) is collected by the objective (magnification  $60\times$ ). This high aperture causes the primary light (blue lines) to pass the objective. From this isolation of scattered light from the nanoparticle, resolved single NP chiral scattering spectrum with a grating spectrometer (Princeton Instruments SP2500i) in combination with a Peltier-cooled front-illuminated CCD camera (Acton PIXIS 256E).

In figure 4.2, SEM images of four representative  $L$ -handed, achiral, and  $D$ -handed single NPs are shown prior to the polymer coating. If we compare the detailed morphologies of the synthesized nanoparticles using the schematic shown in figure 4.1, we could observe that both  $L$ -handed and  $D$ -handed helicoids possess the pinwheel-like morphology. In theory, synthesized nanoparticles should show similar chiral motif which the rotational direction changes respect to the input chiral molecules as shown in the first two images in figure 4.2. However, despite a consistent generation of a chiral motif, artifacts can exist within a synthesis batch and also between each batches. In the case where there is a slight deviation of synthesis condition from the optimum synthesis conditions, resulting chiral nanoparticle morphology could be affected significantly. In this sense, a “chiral motif” in our terminology could be defined as a consistent and re-occurring structural or also spectral features which is continuously present in most single nanoparticles. Representative artifacts of nanoparticle morphologies are shown in the SEM images of the two enantiomers in Figure 4.2. Some of the nanoparticles have chiral features which possess underdeveloped curved arms (third  $L$ -handed particle) and some shows excessive growth and overdeveloped protruded chiral arms (fourth  $L$ -handed particle). Also, there exists a slight size difference between the  $L$ -handed and  $D$ -handed nanoparticles. The achiral hexoctahedron nanoparticles show significantly less structural deviations which there exists minimal observable morphology differences. In order to more comprehensively understand

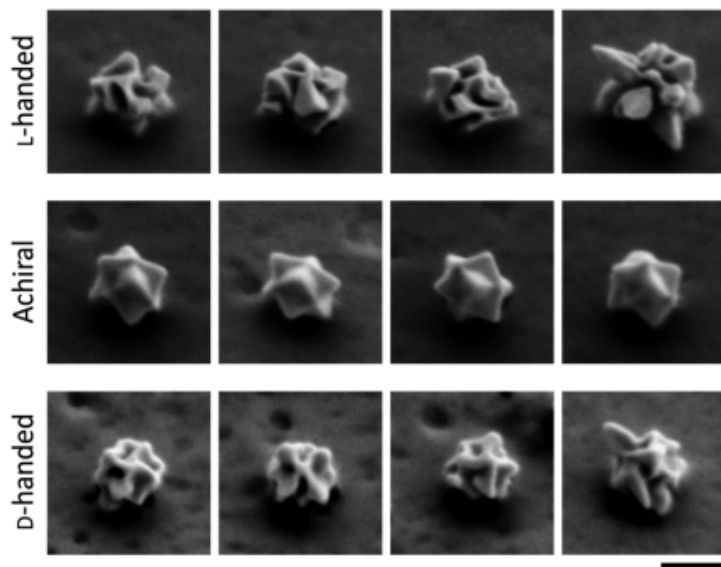


Figure 4. 2 Representative SEM images showing four L-handed, achiral, and D-handed single chiral gold nanoparticle.(scale bar = 200nm)

outcomes of the nanoparticle synthesis and a quantify the optical potential, it is critical to directly relate the nanoparticle morphology with the chiroptic response.

As mentioned, we immobilized spin-coated left-handed (L-handed), achiral, and right-handed (D-handed) nanoparticles on different substrates and embedded them into a spin-on glass. In our measurement setup, the particles will appear as bright red-colored spots due to their efficient plasmonic scattering. For each of the three cases, we have randomly picked 26 red-colored spots as locations of helicoid particles. As the particles are embedded into the spin-on glass, their position and orientation are fixed and we can locate specific particles again, allowing to re-measure the spectra as well as to measure the same spots for different illumination, for example, from the back or front side. In order to obtain reliable spectral information and a decent overview of the spectral spread, it is indispensable to have large enough sampling as well as unbiased particle selection.

### 4.3 Comparison of Single-Nanoparticle Chiral Scatterometry Spectra with Ensemble Measurement

Our study compares the chiroptical responses of 26  $L$ -handed, 26 achiral, and 26  $D$ -handed single NPs. The scattering spectra of single nanoparticles in the visible (VIS) and near-infrared (NIR) spectral range ( $\lambda = 500\text{--}1025\text{ nm}$ ) are shown in Figure 4.3 respect to the illumination of LCP (solid) and RCP (dashed) light. Each spectrum in waterfall plot are manually shifted in vertical

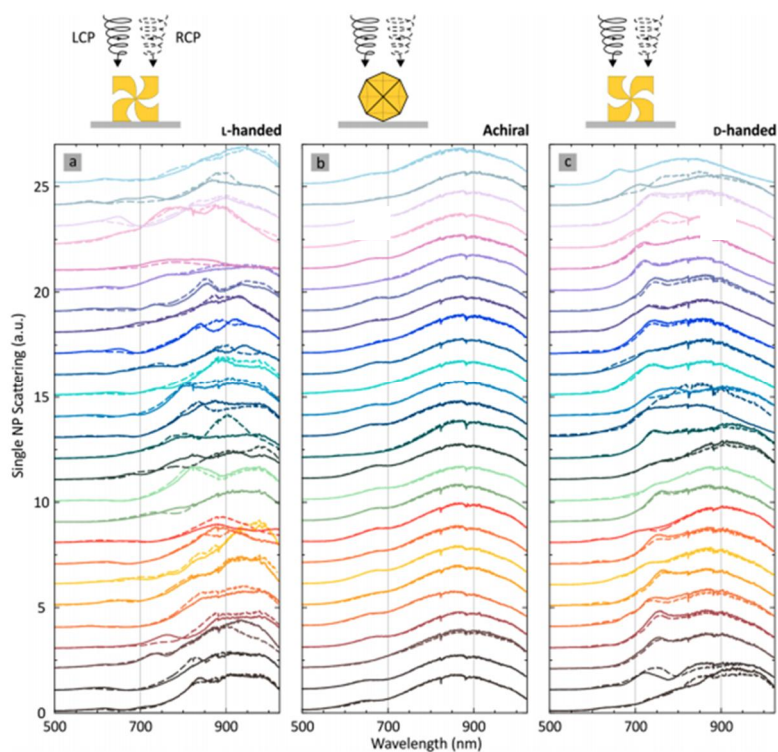


Figure 4. 3 Scattering spectra of randomly picked single nanoparticles each column indicating  $L$ -handed, achiral, and  $D$ -handed nanoparticles. Collected spectra from LCP is indicated in solid line and RCP light illuminated spectra is indicated in dashed line.

direction by 1 (the color code we used to plot the spectra for the individual particles are kept constant throughout the entire chapter). In order to allow a quantitative and clear comparison of the individual scattering spectra and observe detailed difference between spectra, following waterfall plot analysis of 3 x 26 single nanoparticles was conducted.

As the initial step, we investigated the optical responses of the achiral structures, displayed in the middle column. The main scattering spectrum for nanoparticles appear between 700 and 900nm which is similar to the that of chiral nanoparticles. This explains the reddish color display of the individual particles in the dark-field microscope. From the graph, we can observe that scattering spectra for RCP and LCP illumination are very similar to each other for all of the nanoparticles. This result holds significance in two reasons: First, it demonstrates that the synthesized nanoparticles truly show achiral morphology with high uniformity. Second, this experimentally supports and validate our measurement procedure and the set up as the achiral particles show no chiroptical response. In previous reports on single nanoparticle dark-field scattering measurement of chiral morphologies, minute morphological deviations from the ideal achiral shape showed significant chiroptical activity.<sup>25-28</sup> Therefore, the excellent uniformity and indeed non-chiral response of achiral nanoparticles is testimony to the synthesis strategy and also the measurement technique.

The left column in figure 4.3 shows the scattering spectra of the 26 L-handed single NPs. Even roughly observing the scattering spectra, RCP and LCP illuminated scattering spectra can easily be distinguished for all particles, resulting in a strong chiroptical response. Despite consistent chiral response, the exact spectral shapes and signature show a large deviation from one another. Some nanoparticles show only a single main peak while some nanoparticles possess two distinct features and some other nanoparticles show significantly reduced scattering

intensity. A very similar trend is observable in the case of <sub>D</sub>-handed single nanoparticle scattering spectra in the right column of Figure 4.3. Considering the previous mentioned slight size difference between <sub>L</sub>-handed nanoparticles and <sub>D</sub>-handed nanoparticles, <sub>D</sub>-handed nanoparticles show a narrow peak around  $\lambda = 700\text{--}750$  nm with their overall scattering spectra being shifted slightly toward smaller wavelengths. Comparing the scattering response of the <sub>L</sub>-handed and <sub>D</sub>-handed nanoparticles, in average, the chiroptical response of the <sub>L</sub>-handed shows slightly larger and deviated scattering spectra compared to that of <sub>D</sub>-handed nanoparticles.

As the next step, more detailed study of the individual chiroptical properties of the nanoparticles have been conducted. In conventional chiroptic analysis system, molecular or plasmonic nanostructures, often the chiroptical response is defined as differential absorbance for RCP and LCP incident light, called circular dichroism. However, this does not strictly limit that chiral system is only composed and defined by absorbance. For molecular systems which predominantly absorb light and show very little to no scattering of light may hold this true but for plasmonic nanostructures with larger features, this does not strictly follow. Due to its

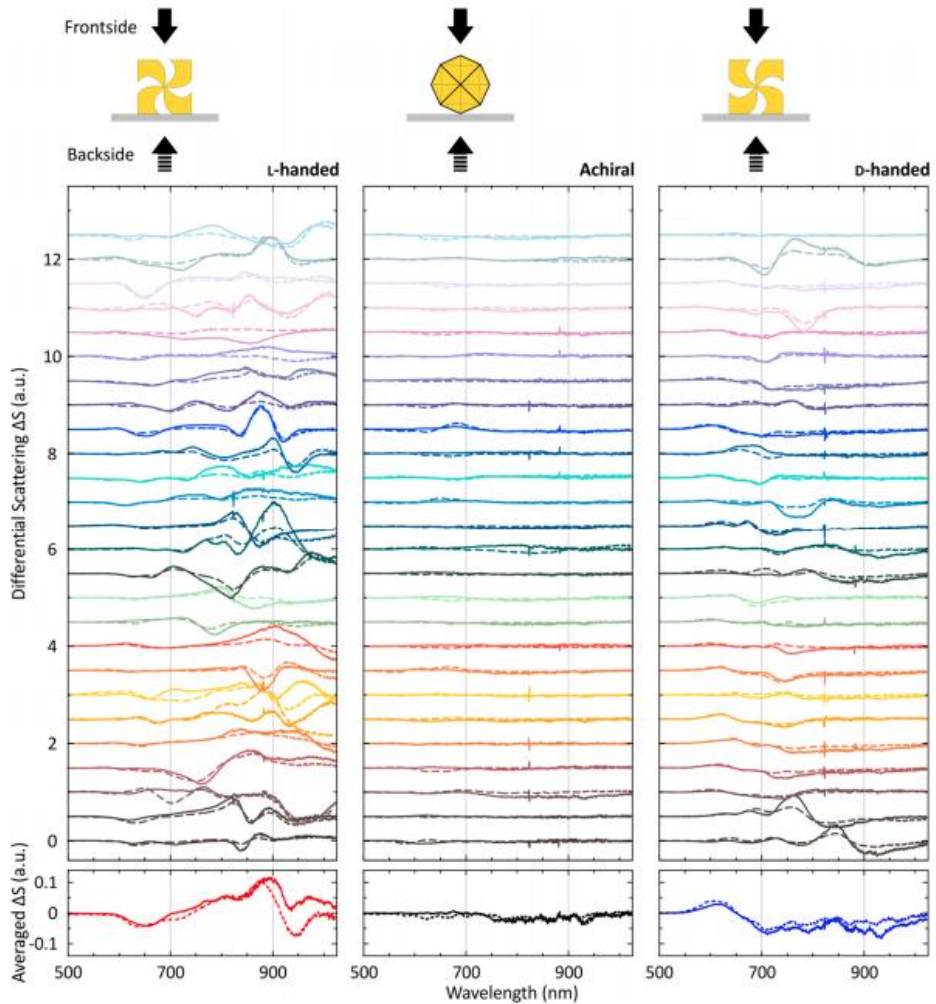


Figure 4. 4 Differential scattering spectra of 3 x 26 sing nanoparticles in forward (solid line) and backward (dashed line) illumination directions.

significantly larger structural size compared to molecules, the light scattering cross sections exceeds that of the absorption cross sections. Therefore, it has been demonstrated that chiral plasmonic systems could be expressed in both of the absorption and scattering response. These two separate optical contributions can contain different information, as spectral far-field scattering response could show

deviation and differences from the absorption response, especially for systems with pronounced interaction via resonant light scattering. In Figure 4.4, we displayed the differential scattering defined as  $\Delta S = S_{\text{RCP}} - S_{\text{LCP}}$ .

The differential scattering spectra obtained from the difference between LCP and RCP applied scattering spectra is shown in Figure 4.4. Considering that our nanostructures are intrinsically showing the high C4 symmetry, no correction for linear artifacts, such as linear birefringence, is required. The displayed differential scattering show much more pronounced and distinct chiroptical response compared to the scattering spectra shown in figure 4.3. Therefore, it is much of scientific importance for the quantitative comparison of the individual responses and the spectral chiral signature of all  $3 \times 26$  single nanoparticles. This is again conducted through use of the waterfall plot. First, we paid a close attention to the reference achiral nanoparticles which we observed a close to zero chiroptical response for all 26 particles. As previously mentioned, this control experiment ensures our optical detection method performs flawlessly while also revealing the excellent quality of the synthesized nanoparticle. Considering the fact that all panels or on same scale, it is clearly distinguishable that the small spectral features shown on the achiral nanoparticles are most likely measurement artifacts. However, mostly in measured achiral nanoparticles, it is at a scale where it is possible to fully negligible when compared to the response of the chiral nanoparticles. Another important control experiment is displayed in the dashed line. Since the nanoparticles are encapsulated and immobilized, we can flip the sample and thus revert the illumination direction. The handedness of a chiral nanoparticle is a geometric property in three-dimensional scale, therefore, it is independent of the illumination direction. However, in general, large chiral nanostructures could have different spectral response depending on the illumination directions due to retardation effects. This behavior is often observed for an elongated spiral structures illuminated along the long axis or perpendicular to the structures. However, for

exactly counter-propagating light fields, the optical response needs to be close to identical. Therefore, the reason for this control experiment is to confirm that spectral response we are observing is true chiral response as the differential scattering spectra showing reasonable agreement to each other. If it is not a genuine chiral response, due to the contributions of polarization conversion or elliptical birefringence, the spectra will show flip of sign. When comparing the differential scattering spectra for forward and backward illumination for the achiral nanoparticles, we could easily observe that spectra show little to no signal, again underlining the achirality and consistency of our nanoparticle and measurement technique. Interestingly, the optical response of one particularly nanoparticle is the 13<sup>th</sup> particle from the bottom shown in dark green. There exists a relatively strong differential scattering signal but it shows almost perfect flips sign for opposite illumination direction. This indicates that the spectral outcome is probably originated from linear birefringence.

Furthermore, we calculated the average differential scattering spectra of single nanoparticles and plotted them in the bottom of Figure 4.4. As it could be inferred from looking at all of the individual spectra, the average differential scattering spectra of the achiral

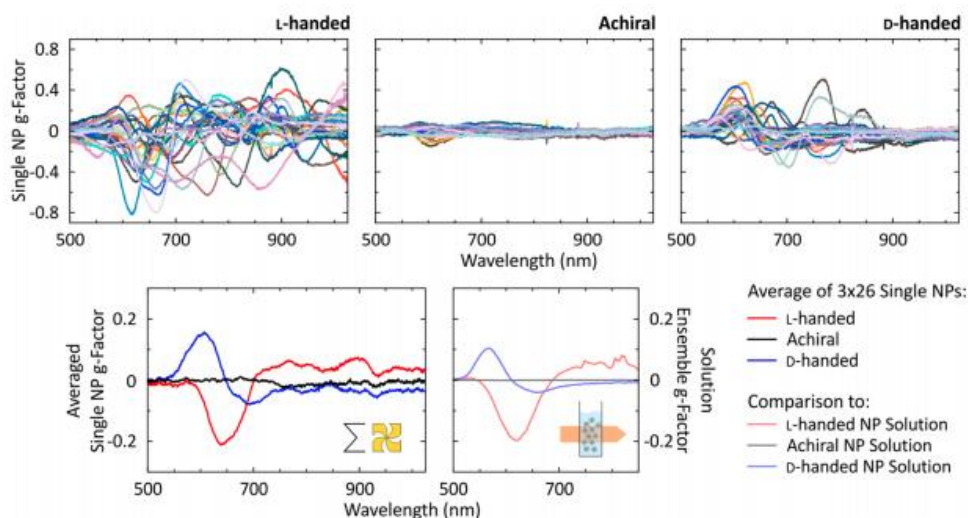


Figure 4. 5 g-factor spectra for all 3 x 26 single nanoparticles. Top row shows differential scattering based g-factor graph while the bottom row indicates the averaged scattering based g-factor (left) and the absorption based g-factor measured in solution state. In both measurement technique, same batch synthesized chiral and achiral nanoparticles have been used.

nanoparticles show close to zero over the entire spectral range and is clearly different from that of the both enantiomeric chiral nanoparticles. Both enantiomer spectra show mirror symmetry in the differential scattering while there exists a good agreement between the average spectra for the nanoparticles being measured in forward (solid) and backward direction (dashed). As in this analysis of the chiral system, we are focusing the analysis of scattering part which the direct comparison of the chiroptical response measured here to the absorption based Circular Dichroism measurements of the nanoparticles in solution requires appropriate normalization. In this context, understanding the scattering based chiral responses through asymmetry g - factor could provide a convenient and effective platform. Asymmetry factor, g-factor has been defined as following, which is similar to that of the absorption based measurement:

$$g = 2 \frac{S_{\text{RCP}} - S_{\text{LCP}}}{S_{\text{RCP}} + S_{\text{LCP}}}$$

In figure 4.5, we plotted the asymmetry factor for all  $3 \times 26$  single NPs and then the average spectra have been presented in the bottom row. In order to signify that collected optical responses from individual nanoparticles show much deviation from each other, we have plotted each set of 26 measurements in one pane. If we intend to analyze the spectra for the <sub>L</sub>-handed and <sub>D</sub>-handed nanoparticles, resulting g-factor spectra all shows deviated and very random peak positions, peak shape, and peak intensity. On the contrary, g- factors for the achiral nanoparticles show close to none chiroptic response which is in accordance with the previous discussion. Most striking result is when we perform average of individually measured, sets of  $3 \times 26$  measurements, we observe a clear and unique chiral feature in the spectra, which shows remarkable resemblance to the solution measured CD based g-factor. The averages of the <sub>L</sub>-handed and <sub>D</sub>-handed nanoparticles show good mirror symmetry. The average of achiral nanoparticle spectra as expectedly, exhibits no chiral features. Only difference between scattering based measured average g-factor and Jasco CD measured absorption based g-factor is a small spectral red shift due to a refractive index increase (from water  $n = 1.33$  to spin-on-glass  $n = 1.41$ ).

This finding holds significance in few aspects. The individual measurements contain clearly significantly more details and information when compared to the average.<sup>29,30</sup> However, as spectra from each individual structures possess many information, many modal signatures are vanished from the average of spectra while only a single dispersive feature remains. This fact allows us to as an important question: Is this optical feature is a result of an intrinsic chiral motif among all nanoparticles or is this result of a certain subset of particles showing its responses after surviving the averaging process while the other optical distinctions are canceled out? This question cannot be fully answered at this point, but could

provide a highly important lessons for improving the field of chiral nanomaterials synthesis for future applications. However, simply asking the question could allow us to point the direction for the development of nanoparticle synthesis. If the chiroptic response is indeed related to certain nanoparticles surviving the averaging process, these particles could be identified and purified for immediate increase of the overall asymmetry. This point is again signified by another important observation of the single-nanoparticle measurements. In some nanoparticles, the g-factor of a few single chiral nanoparticles significantly outperforms the maximum g-factor values of the averaged NPs and also that of the solution state measured g-factor. The nanoparticle solution used for the experiment shows the g-factor of around 0.2. However, we found that the L-handed single nanoparticles could reach g-factor of up to  $g = -0.8$ , which is 4 times larger than the solution and individual average.

## 4.4 Matching of Scattering Spectra with Morphology

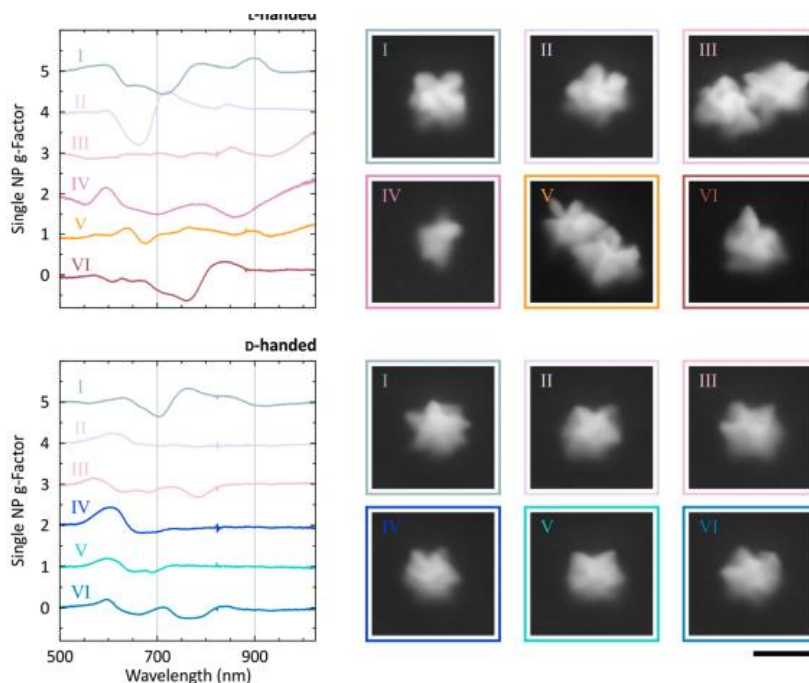


Figure 4. 6 Single nanoparticle g-factor spectra as well as the corresponding SEM images of six selected L-handed and D-handed nanoparticles. The SEM images are blurry as nanoparticle has been embedded in the liquid glass polymer layer for constant refractive index during the optical measurement. The top layer of polymer layer has been etched by the focused-ion-beam (FIB). (Scale bar = 200nm)

The difference between individual spectra but the accordance of average data to solution measurement can only be explained by morphological deviations between the synthesized individual nanoparticles. Therefore, it is of a great importance to try and analyze the morphology of the individual nanoparticles that was optically measured and directly correlate the spectra with the morphology to determine the “best” chiral morphology within the system. In the middle of this process, there exists experimental difficulties. A detailed determination of three-

dimensional morphology would only be possible through advanced TEM techniques. Furthermore, as shown in the figure 4.6, single nanoparticle g-factor spectra and the corresponding SEM images of six selected <sub>L</sub>-handed and <sub>D</sub>-handed nanoparticles has been displayed with label of I– VI. SEM images and responding chiroptic responses for each handed nanoparticles are shown in figure 4.7 and 4.8. Considering that the nanoparticles have been completely embedded in a spin-on glass layer, the SEM images are blurry and only part of the chiral features are shown. From the direct comparison, we could observe the clear differences in the g-factor spectra in between nanoparticles are caused by significant morphological differences as well as the dimensions of the nanoparticles. In order to improve the visibility of the nanostructures, we used a focused ion beam milling, equipped with a laser interferometer stage (Raith ionLine Plus) to determine the exact coordinates of the particles, and selectively etched-off the over-coating polymer layer. Selected SEM images of these particles, both handedness, are shown in Figure 4.6 and the color code for each nanoparticles match the color used in optical data.

Particles I and II possess the highest g-factor of  $g = 0.5$  and  $0.8$ . Interestingly, the main chiroptical peak positions are at the similar spectral region ( $\lambda = 600\text{--}750$  nm) as the mono-dispersive average response which is the representative optical response of the specific chiral nanoparticle. Previously reported simulation data of the 432 helicoid nanoparticles indicated a strong correlation of resulting chiroptical response and the geometrical parameters such as chiral gap depth, width, particle size, and light incidence angle. Among changing various parameters, the reported maximum asymmetry factor based on the simulation was that of around  $g \approx 0.8$  for the given pinwheel-like chiral nanostructures.<sup>18</sup> The best visible top facet ([100] viewpoint) most well represent the ideal pinwheel-like structures, which is very much similar to that of scheme shown in Figure 4.1. While increase in the number of nanoparticle analyzed would give more statistically valuable result, this finding still provides two important

lessons. First, a potential subset of particles could be responsible for the persistent chiral spectral motif visible in Figure 4.5 averaged and solution g-factor spectra. Second, the significantly larger single nanoparticle g-factor compared to other nanoparticles or the ensemble g-factor value suggests that there is immense potential for further improvement of the already outstanding chiroptical response of the 432 helicoid III. In this context, we could focus on the particles IV and VI with clearly deformed morphologies. While the visibility is quite limited, the particle IV exhibits an underdeveloped chiral arms and cavities, which is expected to cause deviation of chiroptic spectrum. Again in the Particle VI case, particle with overdeveloped chiral arms show deviation of chiroptic response respect to the average spectrum. Similar trend could be found in the analysis of <sub>D</sub>-handed nanoparticles. Therefore, key lessons to take from this result is that, while it is difficult to directly correlate specific morphological deviation to the spectral deviation, uniform development of chiral features are key to maintain and increase the overall chiroptic response.

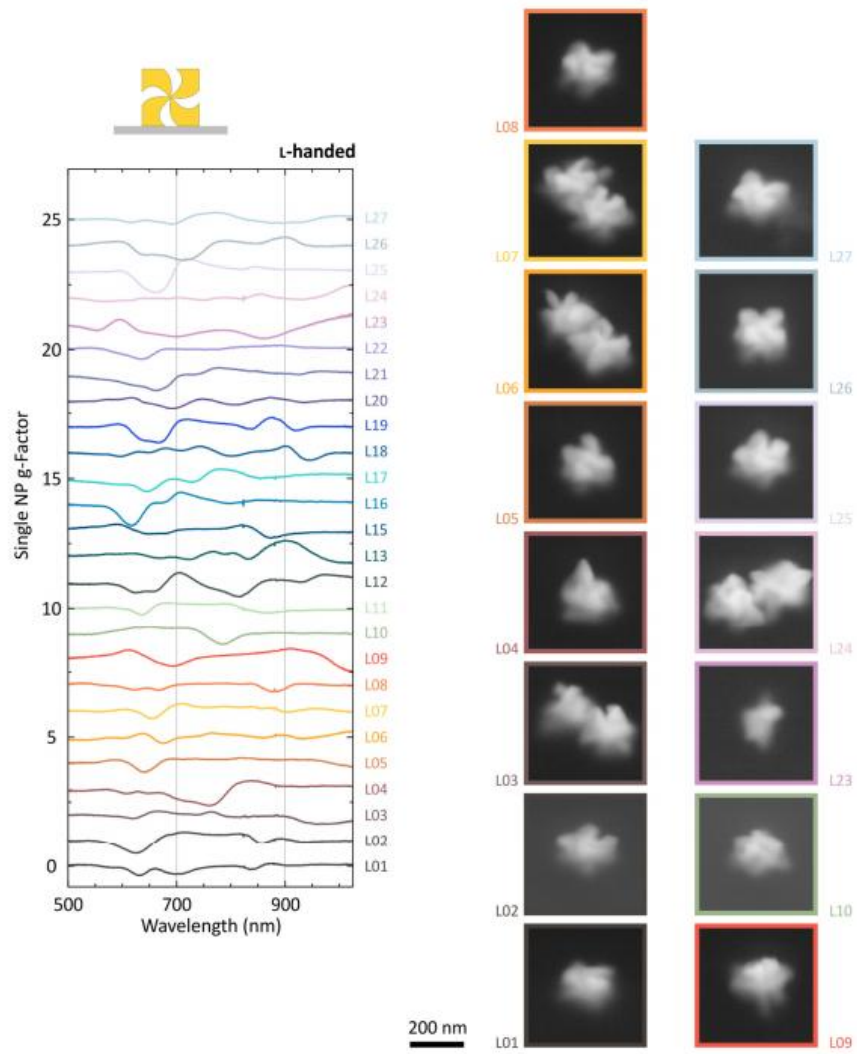


Figure 4. 7 g-factor of total 26 single  $L$ -handed helicoid nanoparticles and some of the correlated SEM images.

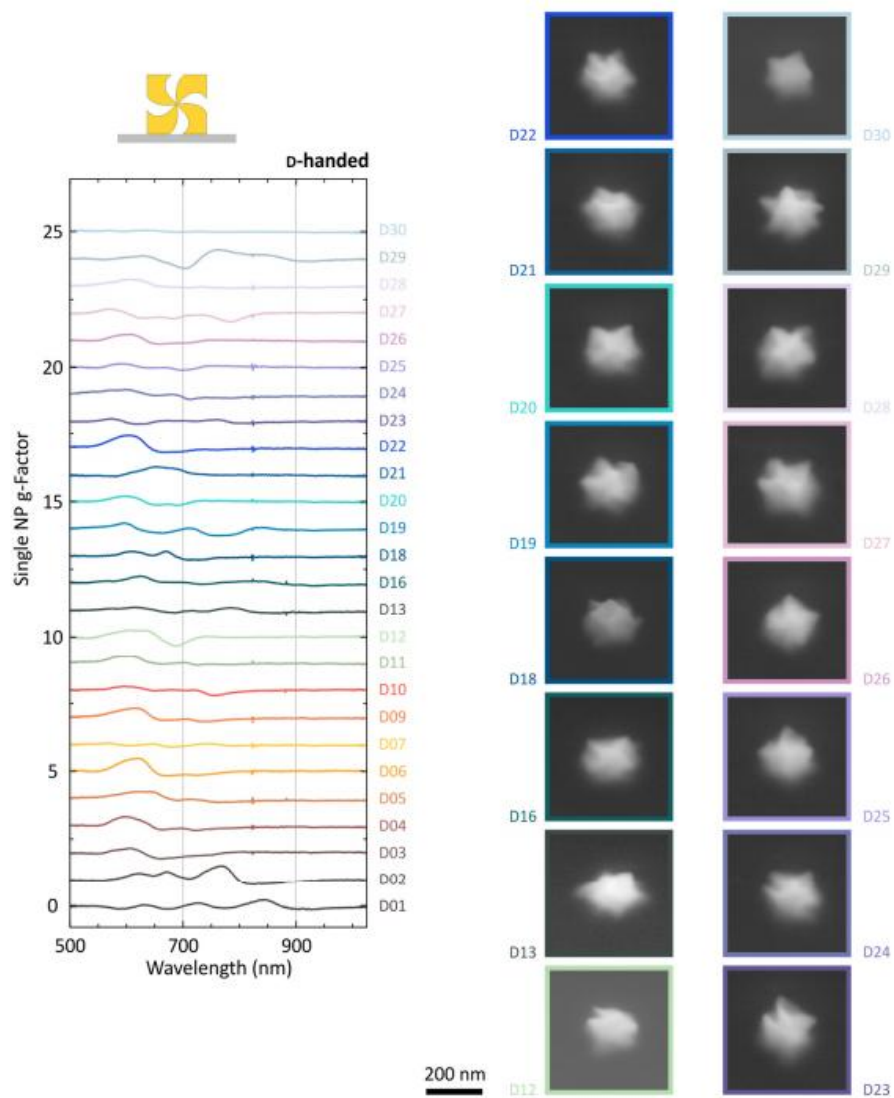


Figure 4. 8 g-factor of total 26 single D-handed helicoid nanoparticles and some of the correlated SEM images.

## 4.5 Conclusion

In conclusion, we have demonstrated a quantitative comparison of the single nanoparticle scale chiroptical responses of chiral gold nanoparticle synthesized by aqueous based chemical synthesis method. We used in-house devised single particle level chiral scatterometry technique based on dark-field scatterometry with collaborative morphology analysis using scanning electron microscopy for the detailed understanding and direct relation of the structural differences and chiroptic response of the individual chiral gold nanoparticles. The differential scattering spectra of each individual left-handed and right-handed gold nanoparticles showed a wide deviation from one another in terms of chiroptic peak position, maximum intensity, and spectral shape, while the achiral nanoparticle showing close to zero chiroptic response and illumination of nanoparticle from front- and back side confirmed the measurement consistency. Since the single nanoparticles have been polymer coated to ensure the uniform refractive index, for the detailed structural analysis of 432 helicoid nanoparticles, focused ion beam milling process was conducted. Individual nanoparticles, as shown in spectral deviations, showed various morphological differences in terms of an under and over developed chiral arm and gap structures. This structural deviation significantly affected the chiroptic response of single nanoparticle. However, when we averaged g-factor converted single NP scattering spectrum, it showed interesting behavior. The averaged single nanoparticle g-factor measured from scattering spectrum resulted in almost identical g-factor spectra in terms of intensity and shape compared to that of ensemble chiroptic response measured in solution. More interestingly, some of the measured individual nanoparticles, the highest g-factor of 432 helicoid III was up to  $g = 0.8$ . This value is 4 times larger than the averaged g-factor from scattering spectrum and from solution ensemble measurement. Our results clearly indicate that there exists large room for potential improvement of chiroptic response in helicoid nanoparticle in ensemble solution from an

appropriate refinement or modification of synthesis for more uniform nanoparticle. Consequently, the presented experimental result has significant engineering value as it indicates that single nanoparticle chiral scatterometry could immediately implicate the quality of nanoparticle synthesis and provide a detailed feedback of the synthesis quality. In addition, our findings can provide general understanding and limitations of chemical nanostructuring methods and allow us to pay attention to develop refinement methods which ensures uniformity of particle morphology and optical response.

## 4.6 Bibliography

- (1) Shemer, G.; Krichevski, O.; Markovich, G.; Molotsky, T.; Lubitz, I.; Kotlyar, A. B. Chirality of Silver Nanoparticles Synthesized on DNA. *J. Am. Chem. Soc.* **2006**, *128* (34), 11006–11007. <https://doi.org/10.1021/ja063702i>.
- (2) Frank, B.; Yin, X.; Schäferling, M.; Zhao, J.; Hein, S. M.; Braun, P. V.; Giessen, H. Large-Area 3D Chiral Plasmonic Structures. *ACS Nano* **2013**, *7* (7), 6321–6329. <https://doi.org/10.1021/nn402370x>.
- (3) Guerrero-Martínez, A.; Alonso-Gómez, J. L.; Auguie, B.; Cid, M. M.; Liz-Marzán, L. M. From Individual to Collective Chirality in Metal Nanoparticles. *Nano Today* **2011**, *6* (4), 381–400. <https://doi.org/10.1016/j.nantod.2011.06.003>.
- (4) Shen, X.; Asenjo-Garcia, A.; Liu, Q.; Jiang, Q.; García De Abajo, F. J.; Liu, N.; Ding, B. Three-Dimensional Plasmonic Chiral Tetramers Assembled by DNA Origami. *Nano Lett.* **2013**, *13* (5), 2128–2133. <https://doi.org/10.1021/nl400538y>.
- (5) Gansel, J. K.; Thiel, M.; Rill, M. S.; Decker, M.; Bade, K.; Saile, V.; Von Freymann, G.; Linden, S.; Wegener, M. Gold Helix Photonic Metamaterial as Broadband Circular Polarizer. *Science* (80-. ). **2009**, *325* (5947), 1513–1515. <https://doi.org/10.1126/science.1177031>.
- (6) Cheng, J.; Le Saux, G.; Gao, J.; Buffeteau, T.; Battie, Y.; Barois, P.; Ponsinet, V.; Delville, M. H.; Ersen, O.; Pouget, E.; et al. GoldHelix: Gold Nanoparticles Forming 3D Helical Superstructures with Controlled Morphology and Strong Chiroptical Property. *ACS Nano* **2017**, *11* (4), 3806–3818. <https://doi.org/10.1021/acsnano.6b08723>.
- (7) Xie, Y.; Kocaefer, D.; Chen, C.; Kocaefer, Y. Review of Research on Template

Methods in Preparation of Nanomaterials. *J. Nanomater.* **2016**, *2016*, 1–10. <https://doi.org/10.1155/2016/2302595>.

- (8) Hentschel, M.; Schäferling, M.; Weiss, T.; Liu, N.; Giessen, H. Three-Dimensional Chiral Plasmonic Oligomers. *Nano Lett.* **2012**, *12* (5), 2542–2547. <https://doi.org/10.1021/nl300769x>.
- (9) Mohammadi, E.; Tsakmakidis, K. L.; Askarpour, A. N.; Dehkhoda, P.; Tavakoli, A.; Altug, H. Nanophotonic Platforms for Enhanced Chiral Sensing. *ACS Photonics* **2018**, *5* (7), 2669–2675. <https://doi.org/10.1021/acsphotonics.8b00270>.
- (10) Radke, A.; Gissibl, T.; Klotzbücher, T.; Braun, P. V.; Giessen, H. Three-Dimensional Bichiral Plasmonic Crystals Fabricated by Direct Laser Writing and Electroless Silver Plating. *Adv. Mater.* **2011**, *23* (27), 3018–3021. <https://doi.org/10.1002/adma.201100543>.
- (11) Liu, Q.; Kuzyk, A.; Endo, M.; Smalyukh, I. I. Colloidal Plasmonic DNA-Origami with Photo-Switchable Chirality in Liquid Crystals. *Opt. Lett.* **2019**, *44* (11), 2831. <https://doi.org/10.1364/ol.44.002831>.
- (12) Chen, W.; Bian, A.; Agarwal, A.; Liu, L.; Shen, H.; Wang, L.; Xu, C.; Kotov, N. A. Nanoparticle Superstructures Made by Polymerase Chain Reaction: Collective Interactions of Nanoparticles and a New Principle for Chiral Materials. *Nano Lett.* **2009**, *9* (5), 2153–2159. <https://doi.org/10.1021/nl900726s>.
- (13) Zhou, C.; Duan, X.; Liu, N. DNA-Nanotechnology-Enabled Chiral Plasmonics: From Static to Dynamic. *Acc. Chem. Res.* **2017**, *50* (12), 2906–2914. <https://doi.org/10.1021/acs.accounts.7b00389>.
- (14) Hentschel, M.; Schäferling, M.; Duan, X.; Giessen, H.; Liu, N. Chiral Plasmonics. *Sci. Adv.* **2017**, *3* (5), 1–13. <https://doi.org/10.1126/sciadv.1602735>.

- (15) Fu, X.; Wang, Y.; Huang, L.; Sha, Y.; Gui, L.; Lai, L.; Tang, Y. Assemblies of Metal Nanoparticles and Self-Assembled Peptide Fibrils - Formation of Double Helical and Single-Chain Arrays of Metal Nanoparticles. *Adv. Mater.* **2003**, *15* (11), 902–906. <https://doi.org/10.1002/adma.200304624>.
- (16) Hou, S.; Zhang, H.; Yan, J.; Ji, Y.; Wen, T.; Liu, W.; Hu, Z.; Wu, X. Plasmonic Circular Dichroism in Side-by-Side Oligomers of Gold Nanorods: The Influence of Chiral Molecule Location and Interparticle Distance. *Phys. Chem. Chem. Phys.* **2015**, *17* (12), 8187–8193. <https://doi.org/10.1039/c4cp06029f>.
- (17) Dietrich, K.; Lehr, D.; Helgert, C.; Tünnermann, A.; Kley, E. B. Circular Dichroism from Chiral Nanomaterial Fabricated by On-Edge Lithography. *Adv. Mater.* **2012**, *24* (44), 321–325. <https://doi.org/10.1002/adma.201203424>.
- (18) Lee, H.-E.; Ahn, H.-Y.; Mun, J.; Lee, Y. Y.; Kim, M.; Cho, N. H.; Chang, K.; Kim, W. S.; Rho, J.; Nam, K. T. Amino-Acid- and Peptide-Directed Synthesis of Chiral Plasmonic Gold Nanoparticles. *Nature* **2018**, *556* (7701), 360–365. <https://doi.org/10.1038/s41586-018-0034-1>.
- (19) Cho, N. H.; Lee, H. E.; Ahn, H. Y.; Lee, Y. Y.; Im, S. W.; Kim, H.; Nam, K. T. Cysteine Induced Chiral Morphology in Palladium Nanoparticle. *Part. Part. Syst. Charact.* **2019**, *36* (5), 1–5. <https://doi.org/10.1002/ppsc.201900062>.
- (20) Li, T.; Wu, X.; Liu, F.; Li, N. Analytical Methods Based on the Light-Scattering of Plasmonic Nanoparticles at the Single Particle Level with Dark-Field Microscopy Imaging. *Analyst* **2017**, *142* (2), 248–256. <https://doi.org/10.1039/C6AN02384C>.
- (21) Hill, C. M.; Bennett, R.; Zhou, C.; Street, S.; Zheng, J.; Pan, S. Single Ag Nanoparticle Spectroelectrochemistry via Dark-Field Scattering and Fluorescence Microscopies. *J. Phys. Chem. C* **2015**, *119* (12), 6760–6768.

<https://doi.org/10.1021/jp511637a>.

- (22) Hu, M.; Novo, C.; Funston, A.; Wang, H.; Staleva, H.; Zou, S.; Mulvaney, P.; Xia, Y.; Hartland, G. V. Dark-Field Microscopy Studies of Single Metal Nanoparticles: Understanding the Factors That Influence the Linewidth of the Localized Surface Plasmon Resonance. *J. Mater. Chem.* **2008**, *18* (17), 1949. <https://doi.org/10.1039/b714759g>.
- (23) Ando, J.; Nakamura, A.; Visoosatt, A.; Yamamoto, M.; Song, C.; Murata, K.; Iino, R. Single-Nanoparticle Tracking with Angstrom Localization Precision and Microsecond Time Resolution. *Biophys. J.* **2018**, *115* (12), 2413–2427. <https://doi.org/10.1016/j.bpj.2018.11.016>.
- (24) Pini, V.; Kosaka, P. M.; Ruz, J. J.; Malvar, O.; Encinar, M.; Tamayo, J.; Calleja, M. Spatially Multiplexed Dark-Field Microspectrophotometry for Nanoplasmonics. *Sci. Rep.* **2016**, *6* (1), 22836. <https://doi.org/10.1038/srep22836>.
- (25) Sachs, J.; Günther, J.-P.; Mark, A. G.; Fischer, P. Chiroptical Spectroscopy of a Freely Diffusing Single Nanoparticle. *Nat. Commun.* **2020**, *11* (1), 4513. <https://doi.org/10.1038/s41467-020-18166-5>.
- (26) Smith, K. W.; Link, S.; Chang, W.-S. Optical Characterization of Chiral Plasmonic Nanostructures. *J. Photochem. Photobiol. C Photochem. Rev.* **2017**, *32*, 40–57. <https://doi.org/10.1016/j.jphotochemrev.2017.05.004>.
- (27) Wang, L.-Y.; Smith, K. W.; Dominguez-Medina, S.; Moody, N.; Olson, J. M.; Zhang, H.; Chang, W.-S.; Kotov, N.; Link, S. Circular Differential Scattering of Single Chiral Self-Assembled Gold Nanorod Dimers. *ACS Photonics* **2015**, *2* (11), 1602–1610. <https://doi.org/10.1021/acsp Photonics.5b00395>.
- (28) Karst, J.; Strohsfeldt, N.; Schäferling, M.; Giessen, H.; Hentschel, M. Single

Plasmonic Oligomer Chiral Spectroscopy. *Adv. Opt. Mater.* **2018**, *6* (14), 1800087. <https://doi.org/10.1002/adom.201800087>.

- (29) Banzer, P.; Woźniak, P.; Mick, U.; De Leon, I.; Boyd, R. W. Chiral Optical Response of Planar and Symmetric Nanotrimers Enabled by Heteromaterial Selection. *Nat. Commun.* **2016**, *7* (1), 13117. <https://doi.org/10.1038/ncomms13117>.
- (30) Slaughter, L. S.; Chang, W.-S.; Swanglap, P.; Tcherniak, A.; Khanal, B. P.; Zubarev, E. R.; Link, S. Single-Particle Spectroscopy of Gold Nanorods beyond the Quasi-Static Limit: Varying the Width at Constant Aspect Ratio. *J. Phys. Chem. C* **2010**, *114* (11), 4934–4938. <https://doi.org/10.1021/jp101272w>.

# Chapter 5. Multi-Chirality Evolution Step for Uniform Chiral Gap Structures

## 5.1 Introduction

Generation of chiral plasmonic structures have opened up new avenues for nanophotonics applications such as negative refractive index and enantiomeric sensing. These applications require not only well controlled chiral morphologies but also the high chiroptic response. With the interest in constructing artificial chiral nanostructures, various attempts to generate novel chiral nanomaterials with exceptional chiroptic response have been conducted. Many attempts, as explained in earlier sections, have used methods such as lithography based technologies, glanced angle deposition, direct laser writing, or template based bottom-up methods.<sup>1-13</sup> However, these methods are known to have limitations in terms of fabrication complexity and limited resolution of chiral morphology control. Therefore, researches continue to find a facile but more industrially applicable materials for chiral nanomaterials.

Recently, a novel aqueous based chemical seed-mediated synthesis method for three-dimensional chiral metal nanoparticles has been presented.<sup>14</sup> For the plasmonic nanoparticle synthesis, seed mediated method have been used for long time due to its precise morphological and optical property control.<sup>15-23</sup> In addition to this well-known synthesis system, thiol containing peptide, such as cysteine or glutathione molecules, has been introduced as chiral shape modifying additives. Addition of these chiral molecules with thiol functional groups showed enantioselective interaction molecules and the intrinsic chiral high-Miller-index surfaces ( $\{hkl\}$ ,  $h \neq k \neq l \neq 0$ ), where the thiol group functioned as the stable anchoring site due to a strong Au-S bonding. This enantioselective binding, where a chiral molecule more preferentially interacts with a specific chiral surface,

promoted an asymmetric growth of plasmonic nanostructures in 100nm scale with strong chiroptical response at visible wavelength. Based on this synthetic method, chiral morphology was generated respect to the input chirality of the used amino-acid or peptide and further tuning and modification of chiral morphology was possible through change in seed morphology and chiral molecule type. Due to its unique 432 point-group symmetry, the nanoparticle has been named as 432 helicoid series. Among synthesized helicoid nanoparticles, 432 helicoid III nanoparticle synthesized with octahedron seed and glutathione molecule exhibit exceptional Kuhn's dis-symmetry factor (g-factor) up to  $g=0.20$  at visible wavelength.

While this g-factor value of 0.20 is already a meaningful chiroptical response, for more versatile and effective application of chiral nanomaterials, increasing the overall optical response is important. In order to do so, accurate analysis and quantification of currently synthesized nanoparticle is required along with detailed synthetic parameter study and growth mechanism study. Single nanoparticle dark-field chiral scatterometry of 432 helicoid III nanoparticle revealed that full potential of its chiroptic response could reach the g-factor of 0.8, which is 4 times larger than the ensemble optical response measured in nanoparticle solution. In more detail, the differential scattering spectra of 26 achiral hexoctahedral, 26 left-handed, and 26 right-handed helicoids III nanoparticles have been measured and was converted to g-factor in order to quantitatively compare it with absorption based circular dichroism measurement technique which has conventionally been conducted to analyze optical response of nanoparticle solution. After the optical measurement, spectra have been analyzed by Scanning Electron Microscopy (SEM) to directly relate the individual nanoparticle morphology and responding chiroptic signal. The most part of this observation is comparison between g-factor of single nanoparticle measured and the averaged optical response of those individual nanoparticles. For chiral

nanoparticle dark field scattering spectra, they showed wide variations in the sense of chiroptical peak positions, intensities, and spectral shape. However, once these individual nanoparticle spectra were collectively averaged, chiroptic response was very much similar to the g-factor spectrum of the same nanoparticle measured in solution state by circular dichroism. After careful matching of the individual nanoparticle morphology and the chiroptic response, we were able to conclude that deformation of chiral gap structures induce significantly lower or deviated response respect to representative optical response. This clearly indicates that chiroptic response of the 432 helicoid III solution holds much potential to be increased if uniform chiral gap structures are able to be formed during nanoparticle synthesis.<sup>14</sup> Considering that our previous simulation data have shown that chirality of 432 helicoid III is significantly affected by the geometry of chiral gap structures, this clearly propose that the potential improvement of 432 helicoid III chiroptic response could be achieved by ensuring particle uniformity, especially chiral gap uniformity.

Therefore, in this chapter, we show the devised kinetic programmed multi-chirality-evolution step based on seed mediated method to significantly enhance particle uniformity and resulting chiroptical response of the 432 helicoid III. In order to sophisticatedly program the growth kinetic and establish the synthetic design principles for 432 helicoid, detailed time variant study and reaction parameter interrelationship study was conducted. Based on this understanding, a kinetic programmed multi-chirality-evolution step applies specifically and individually the growth condition required for effective chirality evolution environment to each growth steps for improved uniformity and chiroptic response.

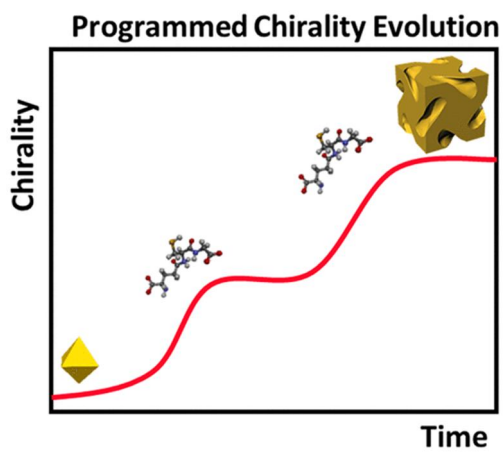


Figure 5. 1 Schematic description of enhancement of chiroptic response through multi-chirality-evolution step in 432 helicoid III synthesis.

## 5.2 Effect of Synthetic Parameters on Chirality Evolution

Kinetic programming for effective chirality evolution during each multi-chirality-evolution-step processes require detailed understanding development process of 432 helicoid and how synthetic conditions affect the chiral growth. In this context, 432 development of chirality in 432 helicoid III growth process was analyzed in detail through synthetic parameter control. Synthetic parameter control enabled the understanding on relationship between growth kinetic modifier and growth direction modifier for chirality evolution.

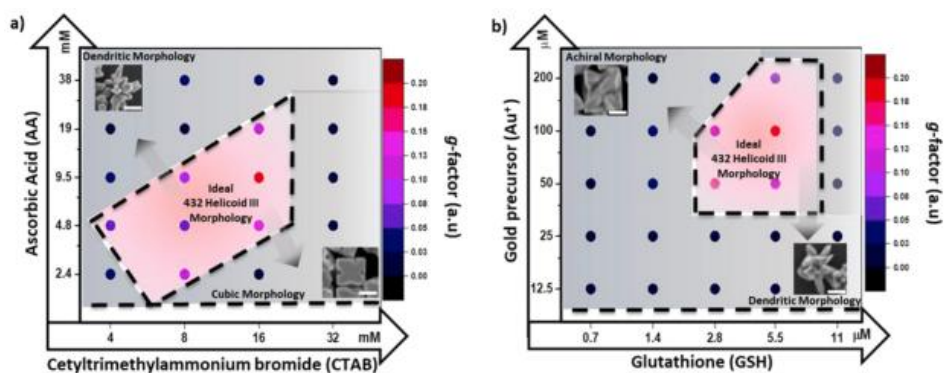


Figure 5. 2 Dissymmetric factor diagram with respect to change in synthetic parameters during a conventional single chiral growth step of 432 helicoid III synthesis. The effective chirality evolution region is highlighted in pale pink. A) Change in dissymmetric factor with respect to change in reducing agent concentration and surfactant capping agent concentration. B) Change in dissymmetric factor with respect to change in Au precursor concentration and chiral peptide concentration. (scale bar = 100nm)

For the precise morphology directing and chirality evolution of 432 helicoid III, fully understanding the inter-relationship between reacting reagents and chiral growth are critical. In previous section, where seed-mediated method

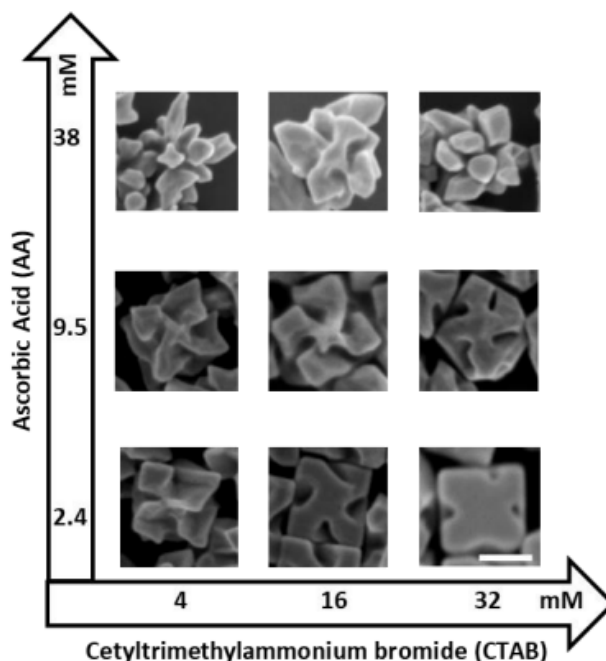


Figure 5. 3 Extended chiral morphology diagram respect to change in Ascorbic acid and CTAB concentration during 432 helicoid III synthesis.

has been introduced, the importance of kinetic driven growth and thermodynamic growth for nanoparticle morphology control has been explained. In the 432 helicoid III synthesis system, ascorbic acid (AA) as reducing agent and cetyltrimethylammonium bromide (CTAB) as surfactant are used. Also, gold chloride trihydrate ( $\text{HAuCl}_4$ ) and  $L,D$ -glutathione ( $L,D$ -GSH) molecules are used as metal source and a chiral inducing molecule. Based on the above mentioned category of reaction parameters during conventional single-step 432 helicoid III synthesis, we constructed two correlation diagram of chirality evolution as shown in figure 5.2. This diagram is to help us precisely determine the collective influence of two co-related synthetic parameters: AA-CTAB correlations figure 5.2 a) and Au-GSH correlation figure 5.2 b).

Correlations of AA and CTAB on chirality evolution of 432 helicoid III is shown in figure 5.2 a). In a previously reported work, we have constructed a morphology diagram for various gold nanoparticle morphology control respect to change in AA and CTAB surfactant concentrations.<sup>15,22</sup> In chemical seed mediated method, relative AA and CTAB ratio participates as a major determinant for the nanoparticle shape, which resulting in various morphology control from gold nanorods, cuboctahedra, cubes and rhombic dodecahedra. Similar to this case, AA and CTAB ratio influenced the chirality evolution critically for 432 helicoid synthesis. The pale pink colored region where ideal 432 helicoid III morphology was synthesized, the effective chirality evolution occurs under very specific ratio between reducing agent and the surfactant concentration. Conventionally during seed-mediated synthesis methods, increase in reducing agent concentration are known to increase the growth kinetic which results in generation of thermodynamically unstable high-index facets.<sup>15,18,21-23</sup> Morphology change respect to the change in synthetic parameter of AA and CTAB is shown in Figure 5.3. For the 432 helicoid III nanoparticle synthesis, further increase of AA concentration resulted in dendritic morphology with various high-index facets, but irregularity of synthesized nanoparticle morphology deteriorated the chiroptic response. On the contrary, increase in the CTAB concentration, which is known to mitigate nanoparticle growth by selectively interacting with {100} facet of gold nanoparticle to promote a thermodynamic stable cubic morphology resulted an opposite result. When the CTAB concentration during 432 helicoid III synthesis was further increased, more cubic boundary structures with significantly enhanced particle uniformity was observed, but shallower or less developed chiral gap structures was observed. Due to underdevelopment of chiral gap structures in terms of depth and curvature, the overall chiroptical response was significantly decreased. As shown, AA and CTAB clearly exhibits the opposite growth tendency towards general nanoparticle synthesis and also chirality development.

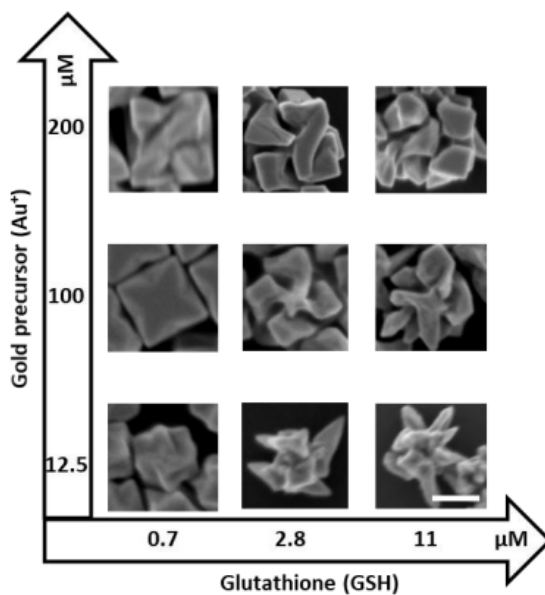


Figure 5. 4 Extended chiral morphology diagram respect to change in gold precursor and GSH concentration during 432 helicoid III synthesis

Relative relationship between chiral GSH molecules and Au metal precursor on chirality evolution of 432 helicoid III is shown in figure 5.2 b) and the respective morphology diagram is shown in Figure 5.4. Chiral GSH molecule is used as the chirality inducer and  $\text{HAuCl}_4$  served the role as metal ion source during the chirality evolution. Chiral molecules, GSH in this case, are known to enantio-selectively interact with R or S plane of high-index planes respect to a matching molecular chirality. Therefore, this enantioselective interaction controls the selective deposition of gold on a specific plane. When GSH concentration is further increased during 432 helicoid synthesis, extensive passivation of a certain facet promotes accelerated asymmetric growth to result in dendritic growth with decreased uniformity. As far as to our understanding, GSH molecules control the growth directionality, Au metal ion precursor concentration affects the absolute amount of gold being deposited to grow the starting seed nanoparticle. This absolute amount of gold being deposited directly affects the growth kinetic and

final size of nanoparticles during the seed mediated method. In both circumstances of increase or decrease in Au precursor amount, achiral high-index nanoparticle was observed. Interestingly, similar with the case of AA and CTAB relationship, a specific ratio of GSH and Au precursor concentration exists for effective chirality evolution, which has been highlighted on the g-factor diagram figure 5.2 b). When the Au-GSH ratio to 36:1 was maintained, control of the 432 helicoids size while preserving its representative chiral spectrum shape was possible. As shown in figure 5.4, decrease of Au precursor amount while maintaining the Au:GSH ratio to 36:1 resulted in 432 helicoid III with smaller size and distinguishably blue shifted chiroptic resonance. Knowing this specific relationship between size and precursor amount, precise generation of intermediate chiral morphology along the growth pathway is possible. Therefore, by segmenting the chiral growth steps and applying kinetically and thermodynamically required growth condition to each steps, another dimension of synthetic capability for chirality evolution is possible.

### 5.3 Time-Variant Analysis of Chirality Evolution

In order to fully understand the process of chirality evolution, it is crucial to study the detailed growth mechanism and its growth pathway of 432 helicoid III respect to reaction time. Time-variant CD measurement allows observation of chirality evolution in terms of chiroptic response and with correlation of this change in optical response to corresponding SEM images could significantly expand our understanding on nanoparticle growth pathway. Temporal CD spectra of 432 helicoid III measured every 5 minutes for total of 2 hours of reaction are shown in Figure 5.5.

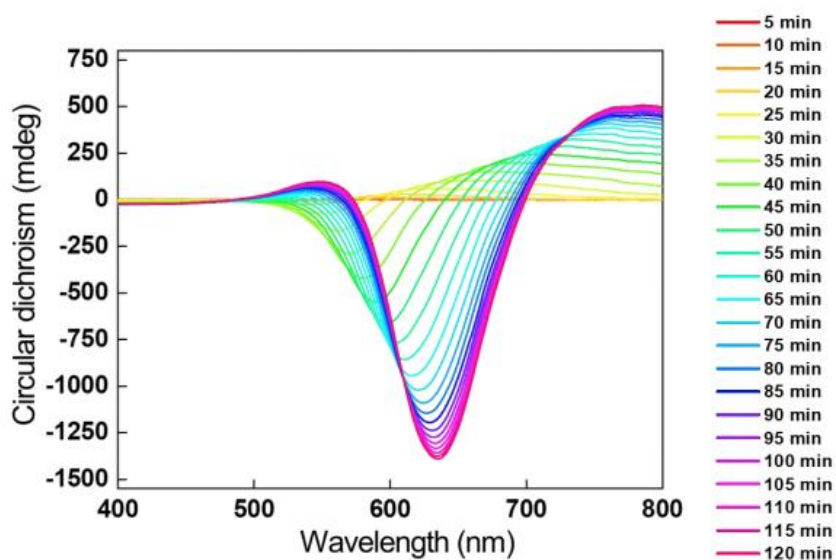


Figure 5. 5 Time-variant CD measurement of 432 helicoid III nanoparticle during its growth process. Chirality progressively increases with shift of resonance to larger wavelength. For this in-situ time-variant CD measurement, the synthesis was conducted in a quartz cuvette while time-interval CD measurement was conducted. The synthesis condition has been kept constant as conventional synthesis method.

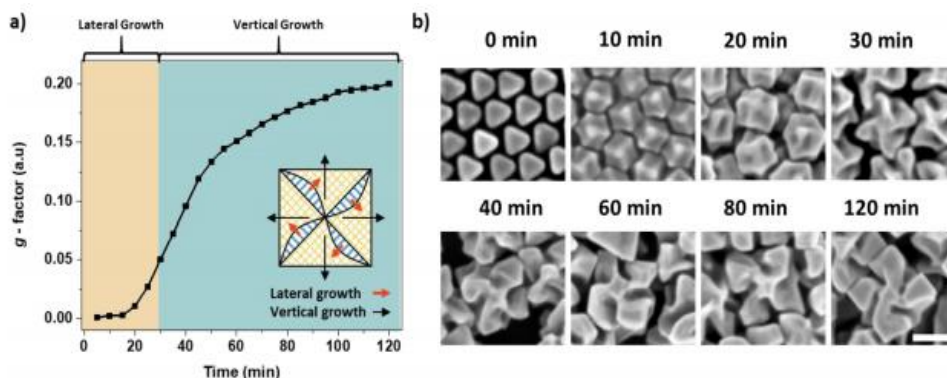


Figure 5. 6 Time-variant study of conventional single chirality evolution step 432 helicoid synthesis. A) Temporal change in dissymmetric factor of 432 helicoid III. Each recorded dissymmetric factor has been recorded with maximum g-factor intensity regardless of peak positions. Schematic description of the lateral growth and vertical growth directions from the  $\{100\}$  perspective. B) SEM images of temporal chiral structure evolution of 432 helicoid III. (Scale bar = 100nm)

Time-variant CD measurement shown in figure 5.5 shows a progressive enhancement of CD response as the reaction proceeds, while the main chiroptic peak red-shifts toward larger wavelengths which is expected to be from the increase of nanoparticles size. This progressive increase of chiroptic response is more clearly shown in figure 5.6 where changes in the maximum g-factor value is marked with possible comparison of morphology with g-factor as well. The progressive chirality evolution process shown in figure 5.7 during 432 helicoid III synthesis could be distinctly divided into two growth regimes.

As noted on the schematic, the first growth regime is specifically dedicated to the lateral growth which formation of high-index facets and tilting of those generated high-index edges are occurring. This can be more visualized when taking a look at the time variant g-factor diagram and the corresponding SEM images together. In the initial 30 min of reaction time, chiral nanoparticles show

the gradual increase in chiroptical response while the representative pinwheel-like chiral motif becomes more distinctly visible. It is believed that the sketch of the major chiral motif of 432 helicoid III is established at this stage of growth to decide the final morphology. Therefore, establishing a stable and uniform high-index generation and edge-tilting growth environment is critical for the chiral development. As the reaction time passes beyond 30 min point, the second growth regime is referred to the vertical growth regime which shows defined chiral gap structure generation along with the cubic outline of nanoparticle formation, which results in a steep incline of chiroptical response. For this vertical growth regime, the SEM images from 40 to 120 min of the reaction shows stabilization of {100} facets while the definition of chiral gap is formed. This experimental result is in accordance with our previously conducted simulation data, that the geometry of the chiral gaps affects the chirality more significantly. The fact that there exist two very distinct growth regimes for chirality evolution indicates that each growth steps requires much different chirality evolution environment. For the lateral growth regime, uniform high-index generation condition and an effective edge-tilting environment is required, and for the vertical growth regime, it requires stable cubical boundary formation for defined chiral gap formation.

## 5.4 Multi-Chirality Evolution Step

For uniform development of chiral gap structures in 432 helicoid III nanoparticle, a multi-chirality-evolution step has been devised and implemented in this work. The general schematic description of the experimental procedure of the multi-chirality-evolution step is shown in Figure 5.7. The as explained in the previous section, the 432 helicoid has two distinct growth regime and devised multi-chirality-evolution step is therefore divided into two discrete growth steps designed based on a detailed 432 helicoid growth mechanism study. During the conventional single-chiral-growth step of 432 helicoid III synthesis, initial control of the growth environment was provided to dictate chiral growth of nanoparticles.

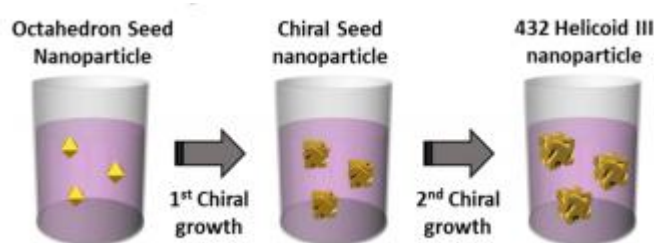


Figure 5. 7 Schematic synthesis steps of devised multi-chirality-evolution step of 432 helicoid III. Steps are segmented to control the synthesis of chiral seed nanoparticle from octahedron seed nanoparticles, followed by uniform growth of 432 helicoid III from synthesized chiral seed nanoparticles.

When a specific growth condition is provided, optimum enantioselective interaction between  $\gamma$ -L-glutathione and chiral high-index facets promote asymmetric growth of a certain plane with surface chirality more preferentially than the opposite chiral surface. Ultimately, this asymmetric growth of a plane induce mirror and inversion symmetry break for the 432 point-group symmetry and growth into overall chiral morphology with the representative pinwheel-like structures of a 432 helicoid III nanoparticle. During the multi-chirality-evolution

synthesis of 432 helicoid III, uniform-sized gold octahedral seed nanoparticles bounded by {111} facet were used and glutathione molecules were used as chiral molecules for the synthesis of small chiral seed nanoparticles. Then, the second chiral growth step was applied to promote more outer boundary controlled and uniform 432 helicoid III with improved chiroptic response. By segmenting the growth steps into two discrete regimes, a specific growth condition could be individually applied to each synthesis step based on the rational design for uniform chiral gap development.

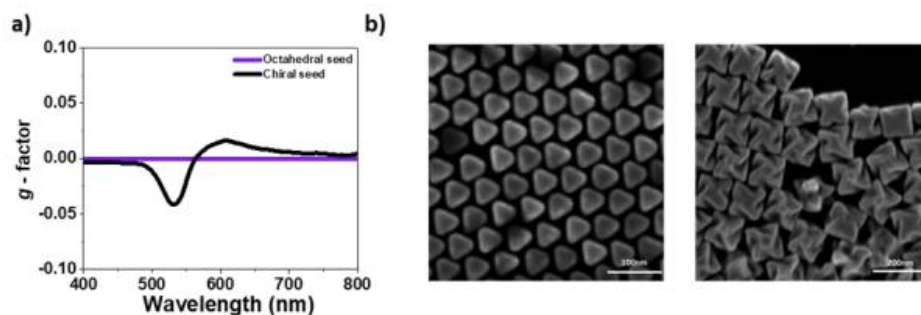


Figure 5. 8 Chiroptic response and SEM images of chiral seed nanoparticles. A) Chiroptic response of octahedral seed nanoparticles and intermediate chiral seed nanoparticles. B) Corresponding SEM images of octahedral seed nanoparticles chiral seed nanoparticles.

Based on the lessons from synthetic parameter control, we were able to learn that it is possible to control the chirality evolution direction as desired. Also, based on the temporal nanoparticle growth study, we were able to learn that each growth regime requires a different chiral growth environment where the lateral growth regime requires construction of growth condition for a uniform high-index and edge-tilting environment while the vertical growth regime requires construction of cubic boundary formation for uniformly defined chiral gap structures. Herein, we segmented the conventional single-step chiral growth into

multiple chiral evolution steps for synthesis of more uniform 432 helicoid III synthesis with higher chiroptic response.

For the first chiral growth step, we synthesized chiral seed nanoparticle from octahedron seed nanoparticle. Starting seed nanoparticles and intermediate chiral seed nanoparticle optical response and morphology are shown in Figure 5.8 a) and b). For both of the chirality evolution steps, a constant Au:GSH ratio of 36:1 has been applied while the amount of gold metal ion precursor was decreased to 50% of the conventional one-step synthesis method. During the lateral growth regime, chiral nanoparticle growth from octahedron seed to chiral seed nanoparticle, the key to uniform synthesis was providing stable and uniform high-index generation condition for effective chiral motif generation. If nanoparticle uniformity is not secured at this stage of chirality evolution, it is difficult to achieve high chiroptic response from finally synthesized 432 helicoid III nanoparticle. Therefore, in the effort to achieve enhanced uniformity while providing sufficient kinetic driving force for high-index generation, the CTAB:Au<sup>+</sup> ratio was doubled to 160:1 respect to conventional synthesis condition. The synthesized chiral seed nanoparticle, as shown in figure 5.8, contains high uniformity with clearly defined chiral motif generation. Here synthesized chiral seed nanoparticle has an average edge length of around 100 nm with a g-factor of 0.05 at around 540 nm. A further modification of reducing agent concentration, decrease or increase in AA concentration, showed shallower gap formation or irregular nanoparticle formation, which deteriorated the chiroptic response of the final nanoparticles. During the vertical growth regime for the chirality evolution, providing a synthesis condition fit for formation of a cubical boundary is important in order to develop a defined chiral gap structure. Therefore, reduced concentration of kinetic parameter, ascorbic acid concentration, with higher CTAB concentration was applied to prevent abnormal gold nanoparticle growth while promoting cubical boundary formation for enhanced nanoparticle uniformity. The AA:Au<sup>+</sup>

concentration ratio was reduced to 9.5:1 from original ratio of 47.5:1, while the CTAB:Au<sup>+</sup> ratio was again maintained at increased ratio of 160:1. In the vertical growth regime of multi-chirality-evolution, a further decrease of the ascorbic acid concentration yields a deteriorated chiroptic response due to underdevelopment of chiral gap formation while decrease in CTAB concentration resulted in morphological deformation and decreased chiroptic response. Finally, uniformity of synthesized nanoparticles was further enhanced through flocculation-based centrifugation process.<sup>24,25</sup>

## 5.5 Quantification of Synthetic Uniformity

Synthesized nanoparticle by the kinetic programmed multi-chirality-evolution step method is shown in Figure 5.9 a) and 5.9 b). The low-magnification SEM image of the newly synthesized 432 helicoid III nanoparticles exhibit exceptional structural uniformity. The multi-chirality-evolution step synthesized nanoparticles show visibly enhanced particle uniformity since nanoparticle shows increased packing ability due to more cubical outer boundary formed as desired. Looking at the high magnification image in Figure 5.9 b) more clearly distinguishes the improved uniformity while the distinct 432 helicoid III chiral morphology of four highly curved chiral arms on each of six cubic faces and pinwheel-like chiral motif are well reserved. Furthermore, while it contains a similar chiral motif, the newly synthesized 432 helicoid III with high uniformity shows more cubical outer boundaries, chiral gap angle, and flat center planes. Figure 5.10 distinguishes these geometrical differences through the graphical modeling of the synthesized 432 helicoid III with high uniformity and some of its representative geometrical parameters. First of all, the most noticeable structural change is the cubical outer boundary formation where the effective edge length of newly synthesized 432 helicoid III shows much narrower distribution. This quantitative analysis of edge length distribution was conducted through binary imaging of the SEM image. The binary converted SEM image was statistically analyzed in terms of the nanoparticle edge length as shown in figure 5.9 c). The statistical distributions of individual nanoparticles edge lengths are compared between conventional 432 helicoid III to multi-chirality-evolution step synthesized 432 helicoid III. For the statistically accurate data, a total of 100 nanoparticles of each types were analyzed. For each nanoparticle images, we set the threshold range and converted them into binary images to separate the particles from the background image. The following extracted

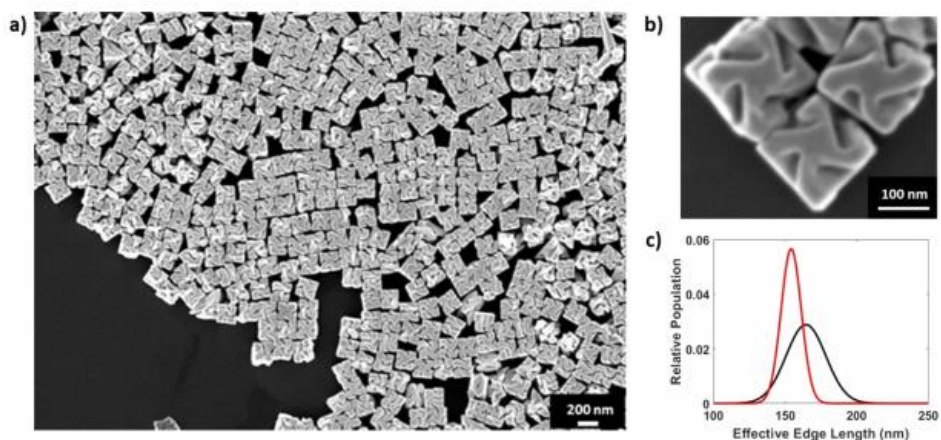


Figure 5. 9 (a) Low-magnification SEM image of newly synthesized 432 helicoid III nanoparticles. (b) High-magnification SEM image of a 432 helicoid III nanoparticle. The representative chiral motif is well preserved with cubical outer boundaries. (c) Particle edge length distribution data of SEM image analysis.

particle images are further analyzed to find the effective edge length of nanoparticles. As shown in Figure 5.9 c), the normal distribution of multi-chirality-evolution step synthesized 432 helicoid nanoparticles shows narrower distribution with standard deviations of the edge length being improved from 13.85 nm to 7.04 nm. This decreased standard deviation of edge length and narrower size distribution spectrum is a clear indication of improved synthetic uniformity. Additionally, the newly synthesized 432 helicoid III with improved uniformity shows relatively decreased chiral gap angle compared to the conventional method synthesized 432 helicoid III, which changes from  $51.5^\circ$  to  $40.9^\circ$  upon measuring 50 nanoparticles for statistical accuracy. This change in the chiral gap angle in newly synthesized 432 helicoid III induces generation of a flat surface at the center of the nanoparticle.

This increase in the morphological uniformity of the synthesized nanoparticles could also be quantitatively observed in its chiroptic spectrum. The

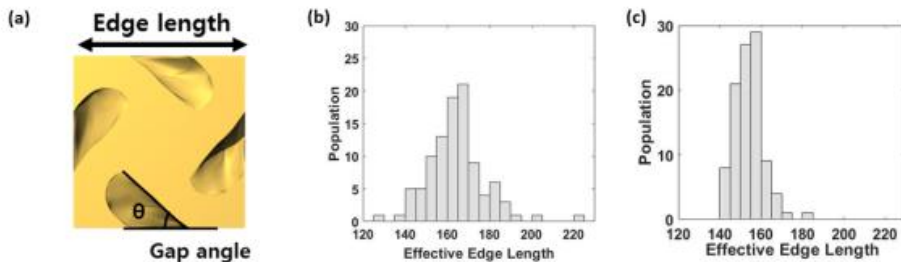


Figure 5. 10 Graphical modelling and size distributions of 432 helicoid III. a) Graphical modelling of 432 helicoid III with high uniformity viewed from direction. Geometrical parameters of chiral components in uniform 432 helicoid III model are indicated. Effective edge length distribution results of 100 particles synthesized via (b) single-step method and (c) multi-chirality-evolution step method

chiroptic g-factor conventional 432 helicoid nanoparticle and the newly synthesized multi-chirality-evolution step are compared in Figure 5.11. The full-width-half-maximum values (FWHM) of the optical responses are used as a tool to understand overall uniformity of synthesized nanoparticles.<sup>26</sup> While the chiroptic response shows retained peak position at around 640 nm for both nanoparticles, the newly synthesized 432 helicoid nanoparticle with improved uniformity shows overall g-factor of  $g = 0.31$  which is increase of 50% compared to conventional 432 helicoid optical response. While the overall g-factor was noticeably enhanced, the FWHM length of the newly synthesized 432 helicoid III g-factor spectrum shows decrease from 74.45 nm to 56.50 ( $\pm 2.27$ ) nm which is a 24.12% decrease. The overall spectrum shape has been maintained which indicates the major chiral component of 432 helicoid has been same for both synthesis method as shown in SEM structural analysis.

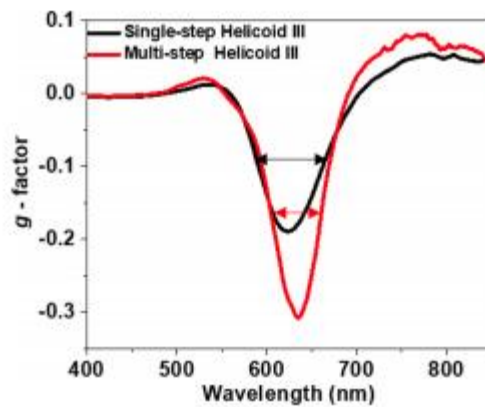


Figure 5. 11 g-Factor spectrum of previous single-step 432 helicoid III (black) and synthesized multi-chirality-evolution step 432 helicoid III (red). The fwhm of each spectrum is indicated with the double-sided arrow in respective spectrum colors.

## 5.6 Conclusion

In conclusion, newly devised multi-chirality-evolution synthesis to systematically enhance overall chiroptic response of 432 helicoid III has been demonstrated. Based on the detailed time-variant mechanistic study of the nanoparticle growth mechanism and understanding inter-relationship between reaction parameters, the conventional single-step chirality evolution has been segmented in two very specific growth regimes. Therefore, in order to systematically control the chirality evolution depending on the growth regime, a specific growth kinetic environment was applied to each growth regime based on the proposed design constraints. The newly synthesized 432 helicoid III with higher uniformity showed significantly enhanced morphological uniformity which has been accompanied with a 55% increase in chiroptic g-factor, reaching  $g = 0.31$ . The increase of g-factor was attributed to the increase of morphological uniformity from a quantitative uniformity analysis, which shows FWHM value being decreased by 24% while increase g-factor and decreased distribution of effective edge length from binary image analysis. From this results, we believe that the newly devised multi-chirality-evolution step could be applied as a general method for aqueous-based nanocrystal morphology control especially for controlling complex nanostructures such as chiral nanomaterials at a very sophisticated level. This presented synthesis method and approach of an idea, to our opinion, provides an efficient platform for uniform and reproducible metamaterial synthesis with highly enhanced optical properties.

## 5.7 Bibliography

- (1) Kneer, L. M.; Roller, E.-M.; Besteiro, L. V.; Schreiber, R.; Govorov, A. O.; Liedl, T. Circular Dichroism of Chiral Molecules in DNA-Assembled Plasmonic Hotspots. *ACS Nano* **2018**, *12* (9), 9110–9115. <https://doi.org/10.1021/acsnano.8b03146>.
- (2) Schreiber, R.; Luong, N.; Fan, Z.; Kuzyk, A.; Nickels, P. C.; Zhang, T.; Smith, D. M.; Yurke, B.; Kuang, W.; Govorov, A. O.; et al. Chiral Plasmonic DNA Nanostructures with Switchable Circular Dichroism. *Nat. Commun.* **2013**, *4*, 1–6. <https://doi.org/10.1038/ncomms3948>.
- (3) Yin, X.; Schäferling, M.; Michel, A. K. U.; Tittl, A.; Wuttig, M.; Taubner, T.; Giessen, H. Active Chiral Plasmonics. *Nano Lett.* **2015**, *15* (7), 4255–4260. <https://doi.org/10.1021/nl5042325>.
- (4) Yeom, B.; Zhang, H.; Zhang, H.; Park, J. Il; Kim, K.; Govorov, A. O.; Kotov, N. A. Chiral Plasmonic Nanostructures on Achiral Nanopillars. *Nano Lett.* **2013**, *13* (11), 5277–5283. <https://doi.org/10.1021/nl402782d>.
- (5) Gansel, J. K.; Thiel, M.; Rill, M. S.; Decker, M.; Bade, K.; Saile, V.; Von Freymann, G.; Linden, S.; Wegener, M. Gold Helix Photonic Metamaterial as Broadband Circular Polarizer. *Science* (80-. ). **2009**, *325* (5947), 1513–1515. <https://doi.org/10.1126/science.1177031>.
- (6) Smith, K. W.; Zhao, H.; Zhang, H.; Sánchez-Iglesias, A.; Grzelczak, M.; Wang, Y.; Chang, W. S.; Nordlander, P.; Liz-Marzán, L. M.; Link, S. Chiral and Achiral Nanodumbbell Dimers: The Effect of Geometry on Plasmonic Properties. *ACS Nano* **2016**, *10* (6), 6180–6188. <https://doi.org/10.1021/acsnano.6b02194>.
- (7) Hentschel, M.; Schäferling, M.; Weiss, T.; Liu, N.; Giessen, H. Three-Dimensional Chiral Plasmonic Oligomers. *Nano Lett.* **2012**, *12* (5), 2542–2547. <https://doi.org/10.1021/nl300769x>.

- (8) Guerrero-Martínez, A.; Auguié, B.; Alonso-Gómez, J. L.; Džolič, Z.; Gómez-Graña, S.; Žinić, M.; Cid, M. M.; Liz-Marzán, L. M. Intense Optical Activity from Three-Dimensional Chiral Ordering of Plasmonic Nanoantennas. *Angew. Chemie - Int. Ed.* **2011**, *50* (24), 5499–5503. <https://doi.org/10.1002/anie.201007536>.
- (9) Ma, W.; Kuang, H.; Wang, L.; Xu, L.; Chang, W. S.; Zhang, H.; Sun, M.; Zhu, Y.; Zhao, Y.; Liu, L.; et al. Chiral Plasmonics of Self-Assembled Nanorod Dimers. *Sci. Rep.* **2013**, *3*, 1–6. <https://doi.org/10.1038/srep01934>.
- (10) Frank, B.; Yin, X.; Schäferling, M.; Zhao, J.; Hein, S. M.; Braun, P. V.; Giessen, H. Large-Area 3D Chiral Plasmonic Structures. *ACS Nano* **2013**, *7* (7), 6321–6329. <https://doi.org/10.1021/nn402370x>.
- (11) Yan, W.; Xu, L.; Xu, C.; Ma, W.; Kuang, H.; Wang, L.; Kotov, N. A. Self-Assembly of Chiral Nanoparticle Pyramids with Strong R/S Optical Activity. *J. Am. Chem. Soc.* **2012**, *134* (36), 15114–15121. <https://doi.org/10.1021/ja3066336>.
- (12) Dietrich, K.; Lehr, D.; Helgert, C.; Tünnermann, A.; Kley, E. B. Circular Dichroism from Chiral Nanomaterial Fabricated by On-Edge Lithography. *Adv. Mater.* **2012**, *24* (44), 321–325. <https://doi.org/10.1002/adma.201203424>.
- (13) Helgert, C.; Pshenay-Severin, E.; Falkner, M.; Menzel, C.; Rockstuhl, C.; Kley, E. B.; Tünnermann, A.; Lederer, F.; Pertsch, T. Chiral Metamaterial Composed of Three-Dimensional Plasmonic Nanostructures. *Nano Lett.* **2011**, *11* (10), 4400–4404. <https://doi.org/10.1021/nl202565e>.
- (14) Lee, H.-E.; Ahn, H.-Y.; Mun, J.; Lee, Y. Y.; Kim, M.; Cho, N. H.; Chang, K.; Kim, W. S.; Rho, J.; Nam, K. T. Amino-Acid- and Peptide-Directed Synthesis of Chiral Plasmonic Gold Nanoparticles. *Nature* **2018**, *556* (7701), 360–365. <https://doi.org/10.1038/s41586-018-0034-1>.
- (15) Ahn, H. Y.; Lee, H. E.; Jin, K.; Nam, K. T. Extended Gold Nano-Morphology Diagram: Synthesis of Rhombic Dodecahedra Using CTAB and Ascorbic Acid. *J. Mater. Chem. C*

2013, *I* (41), 6861–6868. <https://doi.org/10.1039/c3tc31135j>.

- (16) Poerwoprajitno, A. R.; Gloag, L.; Cheong, S.; Gooding, J. J.; Tilley, R. D. Synthesis of Low- and High-Index Faceted Metal (Pt, Pd, Ru, Ir, Rh) Nanoparticles for Improved Activity and Stability in Electrocatalysis. *Nanoscale* **2019**, 18995–19011. <https://doi.org/10.1039/c9nr05802h>.
- (17) Hong, J. W.; Lee, S. U.; Lee, Y. W.; Han, S. W. Hexoctahedral Au Nanocrystals with High-Index Facets and Their Optical and Surface-Enhanced Raman Scattering Properties. *J. Am. Chem. Soc.* **2012**, *134* (10), 4565–4568. <https://doi.org/10.1021/ja300598u>.
- (18) Langille, M. R.; Personick, M. L.; Zhang, J.; Mirkin, C. A. Defining Rules for the Shape Evolution of Gold Nanoparticles. *J. Am. Chem. Soc.* **2012**, *134* (35), 14542–14554. <https://doi.org/10.1021/ja305245g>.
- (19) Lee, H.; Habas, S. E.; Kwekin, S.; Butcher, D.; Somorjai, G. A.; Yang, P. Morphological Control of Catalytically Active Platinum Nanocrystals. *Angew. Chemie* **2006**, *118* (46), 7988–7992. <https://doi.org/10.1002/ange.200603068>.
- (20) You, H.; Fang, J. Particle-Mediated Nucleation and Growth of Solution-Synthesized Metal Nanocrystals: A New Story beyond the LaMer Curve. *Nano Today* **2016**, *11* (2), 145–167. <https://doi.org/10.1016/j.nantod.2016.04.003>.
- (21) Lee, Y. W.; Kim, D.; Hong, J. W.; Kang, S. W.; Lee, S. B.; Han, S. W. Kinetically Controlled Growth of Polyhedral Bimetallic Alloy Nanocrystals Exclusively Bound by High-Index Facets: Au-Pd Hexoctahedra. *Small* **2013**, *9* (5), 660–665. <https://doi.org/10.1002/sml.201201813>.
- (22) Grzelczak, M.; Pérez-Juste, J.; Mulvaney, P.; Liz-Marzán, L. M. Shape Control in Gold Nanoparticle Synthesis. *Chem. Soc. Rev.* **2008**, *37* (9), 1783–1791. <https://doi.org/10.1039/b711490g>.
- (23) Huo, D.; Cao, Z.; Li, J.; Xie, M.; Tao, J.; Xia, Y. Seed-Mediated Growth of Au Nanospheres

into Hexagonal Stars and the Emergence of a Hexagonal Close-Packed Phase. *Nano Lett.* **2019**, *19* (5), 3115–3121. <https://doi.org/10.1021/acs.nanolett.9b00534>.

- (24) Park, J. E.; Lee, Y.; Nam, J. M. Precisely Shaped, Uniformly Formed Gold Nanocubes with Ultrahigh Reproducibility in Single-Particle Scattering and Surface-Enhanced Raman Scattering. *Nano Lett.* **2018**, *18* (10), 6475–6482. <https://doi.org/10.1021/acs.nanolett.8b02973>.
- (25) Park, K.; Koerner, H.; Vaia, R. A. Depletion-Induced Shape and Size Selection of Gold Nanoparticles. *Nano Lett.* **2010**, *10* (4), 1433–1439. <https://doi.org/10.1021/nl100345u>.
- (26) Badr, Y.; Wahed, M. G. A. El; Mahmoud, M. A. On 308 Nm Photofragmentation of the Silver Nanoparticles. *Appl. Surf. Sci.* **2006**, *253* (5), 2502–2507. <https://doi.org/10.1016/j.apsusc.2006.05.021>.

## Part II. Expansion of Chiral Nanoparticle Synthesis Method for More Versatile Applications

In this part of thesis, it is our goal to establish a fundamental understanding of seed-mediated method using different experimental parameters which could allow potential expansion of chiral nanomaterial applications. Previously, we have experimentally demonstrated and theoretically understood chirality transfer from small chiral molecules such as amino acids or short peptides to plasmonic gold metal. Furthermore, we have synthetically programmed each growth step of multi-chirality-evolution step to selectively tune chiral nanoparticle morphology and uniformity for enhanced optical response. Based on these lessons learned experimentally and theoretically, in the following part, two approaches to examine potential expandability of our synthesis method has conducted: 1) use of longer sequence programmable oligomer for chiral nanoparticle synthesis, 2) use of alternative metal source besides gold for more versatile applications of chiral nanomaterials.

### **Chapter 6. Expansion of Chiral Inducing Agent**

#### **6.1 Introduction**

For generating various chiral nanostructures and optical responses, it is a great advantage to utilize amino acid and peptide as there exists numerous possible options for peptide selection to control morphology and optical response. However, in the context of programming desired chiroptic response to nanostructures under a specific design principle, using individual amino acids or peptides could show limitations. Therefore, longer biological molecules with possibilities of sequence programming ability could provide a new avenue for chiral nanostructure control.

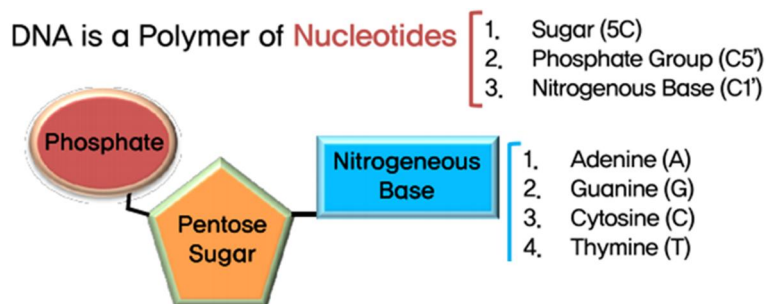


Figure 6. 1 Structures of DNA which contains Phosphate group, sugar group, and nitrogenous base group. Each nitrogenous bases are Adenine, Guanine, Cytosine, and Thymine which differs in its molecular structures.

Deoxynucleic acid, DNA, is a molecule composed of nucleotide chains which have been used as genetic information transporter for millions of years in our biological system. With the sequence programming, genes which contains information in terms of quantity and quality, that can't be fully understood even at our current technology, have been delivered on to next generations. DNA is composed of nucleotides which contains a phosphate group, a sugar group, and a nitrogen base as shown in figure 6.1. The four types of nitrogen bases are Adenine(A), Cytosine(C), Guanine(G), and Thymine(T). The structures of each nucleobase are different from each other as following; 1) Adenine and Guanine have a fused-ring structure of outer frame derived from purine, 2) Cytosine and thymine is derived from pyrimidine. In this research, only the 4 nucleobases found in DNA are used for the experiment and Uracil found in RNA are not considered. Purine bases are characterized by their single amino group at a carbon which the exact position differs between adenine and guanine. Also, similarly, pyrimidine bases show amine containing bases in different positions as well for Cytosine and Thymine. Adenine are known to form base complements with Thymine, while Guanine are known to form base complements with cytosine. This base complements are the key to formation of helical structures of double-stranded DNA

which is expected to be from dimensional constraints. With the specific combinations and ordering of these bases, DNA sequence forms genes which tells cells to make proteins. Recent research revealed that about two-thirds of cancer mutations in cells are originated from random mistakes in DNA.<sup>1,2</sup> Therefore, there has been numerous efforts to program or modify the DNA sequences as desired for biological applications.<sup>3-7</sup> In this regard, DNA sequencing is the technology which allows us to utilize and program the order of bases in a DNA sequence. With the recent advancement of gene editing technologies, design of a specific DNA sequence is becoming more facile in terms of accuracy, complexity, and economical feasibility. Therefore, the idea of using DNA as a tool to program information has been continuously increasing. One of the representative example for utilization of programmability of DNA is using DNA as a new digital data storage method.<sup>8-11</sup> Inspired from DNA induced information encryption and transportation found in biological systems, researchers utilized sequencing of DNA nitrogenous bases to represent bits in digital data information which could be later decoded back to digital data. Also, in 2017, DNA was used as a code for pixels in a movie which encoded data in the form of DNA was used to make a short video.<sup>12</sup> The lessons to be taken from these examples are that DNA is a useful tool for programming information which could be utilized in our case for programming specific chirality into plasmonic nanomaterials to meet the demands of various applications.

## 6.2 Gold-DNA Surface Interaction

As explained in previous section, DNA has potential programmability of information which is controlled by the ordering of nucleobases. Nucleobases structures are all distinct from each other which induces binding affinity difference with metal surface respect to the nucleobase type. Therefore, multiple researches have been conducted to understand interactions between material surface and DNA nucleobases.<sup>13-16</sup> Especially in the nanoparticle research, interface of DNAs and nanoparticles combine the advantages of utilizing both materials. While utilizing much of nanoparticles unique physical and chemical properties, relatively large surface area of nanoparticles compared to the bulk material provide sufficient binding sites for high-density loading of DNA. Due to the preservation of DNA functions after the adsorption on nanomaterials, addition of DNA to different shapes and sizes of nanoparticles have been demonstrated.<sup>17-21</sup> Furthermore, due to the stable anchoring platform of nanoparticles for nucleobases, DNA stability has been significantly improved.

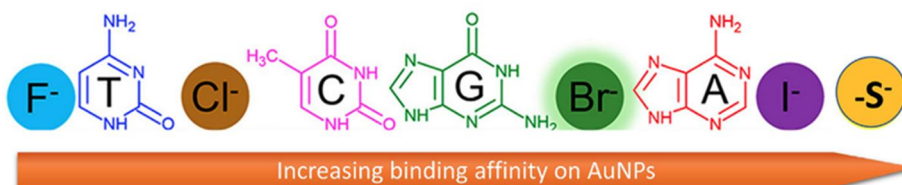


Figure 6. 2 Comparison of the binding affinity of halide ions and nucleotides on gold nanoparticles. the measurement has been conducted through colorimetric and Raman assay.

With the ease of controlling the nano-morphologies and its facile biological applicability, gold nanoparticles have been often used as the platform for DNA-nanoparticle conjugated system.<sup>22-27</sup> There are three representative ways

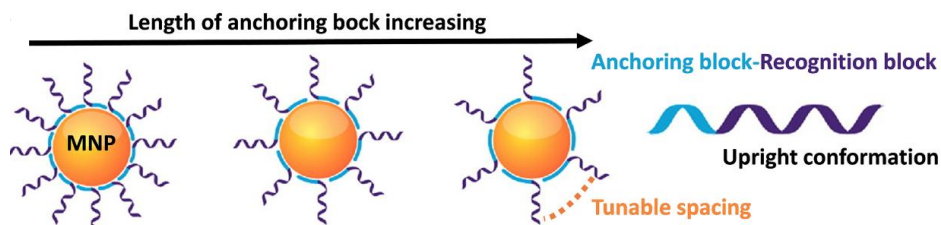


Figure 6. 3 DNA conformation and surface density control by change in length of anchoring block. Increase in the anchoring block induced lower density of DNA on gold nanoparticles.

to create an interface between DNA and metal surfaces: DNA adsorption by end terminal thiolation, Phosphorothioate modification, or consecutive nucleotides for anchoring. As previous sections already established the strong Au-S binding affinity, thiolated at the end chain of a DNA sequence or phosphorothioate modification can provide facile approaches to form an interface with gold nanoparticle surface. As this method is a facile approach to adsorb DNA to gold nanoparticle, it holds limitation in density control and limited conformation.<sup>28,29</sup> However, for nucleobase dependent adsorption base study, it is more clear to observe the changes in binding affinity by applying consecutive nucleotides for anchoring on gold nanoparticle due to direct interaction of nucleobases with gold surfaces.<sup>30</sup> Based on the colorimetric and Raman assays, the binding affinity of each nucleobases are compared with halide ions. As shown in figure 6.2, the binding affinity on gold nanoparticle follows the order of  $I^- > A > Br^- \approx G > C > Cl^- \approx T > F^-$ . These nucleobases dependent adsorption mechanism is due to the difference between the energetic stability of chemisorption via the keto and imino groups on DNA nucleobases.<sup>31</sup> Further studies of binding affinity differences of nucleobases to gold nanoparticle are conducted through Raman and FT-IR measurement which shows similar trend of binding affinity as shown in figure 6.2.<sup>16</sup>

For using consecutive nucleotides for anchoring on gold nanoparticle, there have been attempts to control the nucleobase density and conformation on gold nanoparticles. Representatively, Fan's group designed diblock DNA sequences which is composed of two separate nucleobase block. These diblock DNA sequences contained two blocks which first consecutive nucleotides served the role of anchoring onto metal nanoparticles while the other consecutive nucleotides with lower binding affinity provided a recognition block with upright conformation for selective DNA hybridization.<sup>32,33</sup> By controlling the anchoring block length, it was possible to precisely control the lateral spacing of the nucleotides at the metal surface as shown in figure 6.3.<sup>33-35</sup> Furthermore, increasing the poly A anchoring block length systematically decreased the surface densities of the ssDNAs. However, due to the strong adsorption affinity of Adenine onto gold surface, anchoring block in diblock DNAs tend to wrap around the metal nanoparticles instead of an upright conformation. In order to resolve this issue, Liu et al. decreased the conjugation solution pH to induce absorption of nonthiolated DNAs on gold nanoparticles in an desired orientation.<sup>36</sup> With the use of the low pH, adenine ( $pK_a = 3.5$ ) is protonated to promote the formation of hydrogen bond between the exocyclic amino group in one adenosine and the heterocyclic ring nitrogen atom (N7) in another. This generation of hydrogen bond results in the formation of  $AH^+ - H^+A$  base pair, which is known as A-motif. Due to the very specific method of folding structure present with A-motif, it is less favorable to the hybridization reaction but more susceptible to the selective adsorption of the adenine consecutive ends to the gold nanoparticles by electrostatic attraction.<sup>30</sup> Furthermore, Liu's group proposed conformation control of the diblock DNAs to gold nanoparticle by applying a lower affinity showing nucleotides, such as poly T, to AuNPs with DNA anchored with poly A sequences for upright conformation control.

### 6.3 DNA directed Nanoparticle Synthesis

Morphology control of metal nanoparticles can manipulate the surface properties, optical properties, and chemical properties, which provides much of applicability to areas such as optical applications, catalysis applications, sensing applications, and biomedical applications. In the introduction section, chiral nanostructures from bottom-up method have briefly discussed the chiral morphology control using DNA as the starting platform.<sup>37-45</sup> From multiple examples of DNA origami to DNA based hybridization for chiral nanostructure generation, various chiral nanostructures have been generated with some of structures exhibiting active chiral plasmonic applications to sequence based morphology control. One of the critical advantage of the DNA based nanostructuring was its potential controllability of sequence length and nucleobases which upon selective hybridization, induces magnificent nanostructures. Therefore, applying DNA directly to the synthesis of nanoparticles have been demonstrated. While there has been no chiral nanoparticle reported using DNA as morphology controller, various high-index nanoparticle morphology was generated.<sup>46-49</sup>

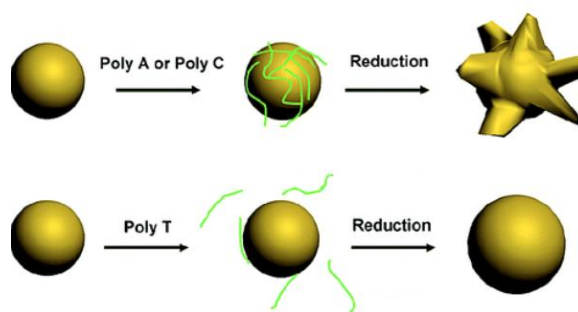


Figure 6. 4 Morphology development ability of nucleotide oligomers for gold nanoparticles starting from spherical seed morphology.

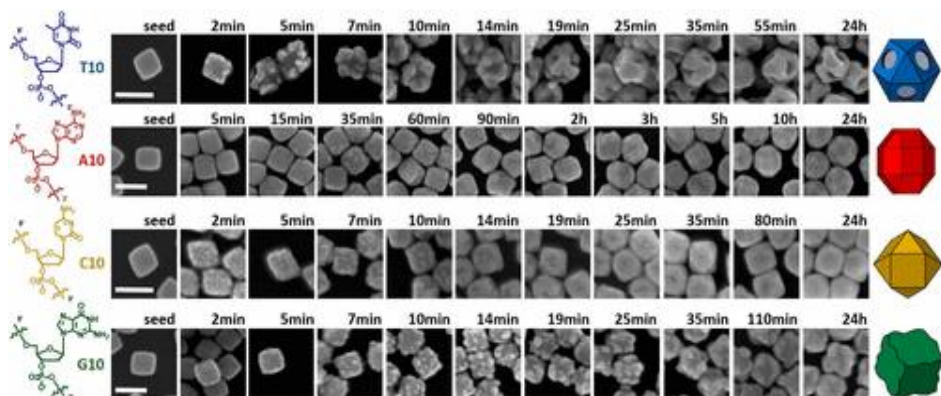


Figure 6. 5 DNA nucleobases directed nanoparticle morphology control from low-index cubic nano-seed under co-reduction of gold and palladium.

Yi Lu group reported the control of nanoparticle morphology using the nucleotide oligomer starting from the spherical seed nanoparticle. As shown in the figure 6.4, 30-merpoly A or poly C induced the flower-shaped high-index nanoparticle morphology while introduction of Poly T induces larger sized spherical nanoparticle.<sup>46</sup> The Detailed mechanistic studies show that the difference in the binding affinity of nucleobases play a major role in construction of different nanoparticle morphology. These DNA-functionalized flower shaped nanoparticles show cell uptake ability which is confirmed by dark-field microscopy. In 2016, Yi Lu group conducted DNA-mediated nanoparticle synthesis with different morphologies under palladium and gold co-reduction system as shown in figure 6.5.<sup>47</sup> The presence of different nucleobases in the growth solution induced 4 distinct morphologies which is confirmed from SEM. By taking the time-variant morphology analysis, each distinct morphologies are generated as reaction time increases. This data shows potential programmable control of metallic nanoparticle shape and properties for more complex applications. Furthermore, while the previous work utilized the low-index facet seed nanoparticles, seeds that are enclosed by high-energy facets are known to provide a facile deposition site

during nanoparticle growth. In Figure 6.6, starting from a concave palladium nano-cube seed, 10-mer DNA molecules using Adenine, Cytosine, Guanine, and Thymine. Again in this case, each nucleobase has different binding affinities as Adenine has the highest affinity.

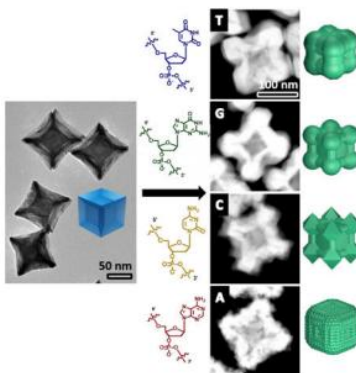


Figure 6. 6 DNA driven morphology control of concave cubic palladium seed nanoparticle.

## 6.4 Effect of ssDNA Oligomer on Chirality Evolution during 432 Helicoid II Synthesis

From the previous reported data on nanoparticle morphology control using single-stranded DNA (ssDNA) molecules, we were able to find out that DNA can serve a role during nanoparticle morphology control along with other surfactants and capping agents. Therefore, it was our goal to find out how ssDNA could affect the chirality evolution during 432 helicoid nanoparticle synthesis. In this reason, we have introduced Thymine oligomer (20-mer T) during 432 helicoid II synthesis which uses cubic seed nanoparticle and glutathione molecule as chirality inducer as shown in figure 6.7. All synthesis condition was maintained constant except the additional introduction of T20mer. For detailed understanding of effect induced by T20mer, time variant study, morphology study, and CD analysis was conducted.

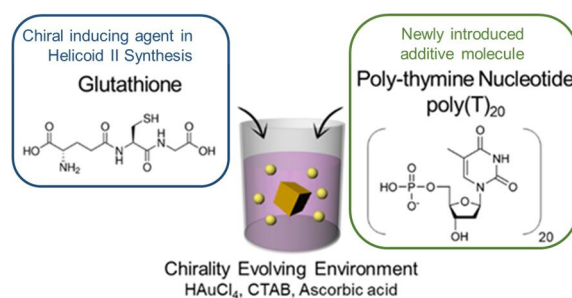


Figure 6. 7 Experimental schematic of Thymine oligomer assisted 432 helicoid II synthesis method.

For the synthesis of 432 helicoid II, chiral glutathione molecules are used as chirality inducing agent. During this process, T20mer was additionally introduced to the growth solution. As shown in figure 6.8, the conventional 432 helicoid II shows the g-factor of 0.04 at near 600nm wavelength. However, T20mer added 432 helicoid II shows the g-factor of 0.08 which is about 2 times

larger than that of the conventional 432 helicoid II. Interestingly, under the same synthesis condition with only using thymine oligomer as the chirality inducing agent, no chiroptic response has been observed. This indicates the thymine oligomer does not induce chirality but in a way helps the development of chirality during helicoid nanoparticle synthesis. One of the expected reason of this is shown in the below SEM images. While 432 helicoid II synthesized with glutathione and T20mer shows more defined chiral features compared to the 432 helicoid II synthesized only using glutathione, nanoparticles synthesized with only using T20 showed very definite high-index generation. This can be understood that the T20mer is involved in the high-index facet generation process which these high-index facets provide a platform for enantioselective interaction between chiral surfaces and chiral molecules.

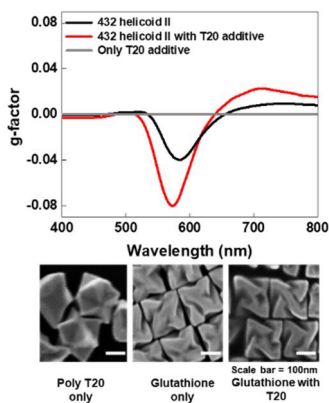


Figure 6. 8 Chiroptic response and corresponding SEM images of 432 helicoid II, 432 helicoid II with T20 introduced, and nanoparticle synthesized using only T20mer.

Time-variant analysis of 432 helicoid II with T20 added supports our understanding on how T20mer affects the chirality evolution. T20 oligomer has been introduced on 0 minute, 40minutes and 80 minutes of the reaction time in

order to find how insertion time of T20mer affects the chirality evolution. From the time variant graph, we were able to find out that introduction of T20 oligomer from the beginning of the reaction has the largest effect on chirality evolution, which indicates that it is mostly related with the earlier stage of the growth. This data is in accordance with the conclusion that T20 aids the high-index formation obtained from the SEM based morphology analysis. From this data, we were able to conclude that ssDNA oligomers are able to participate in a form of organic shape modifier during gold nanoparticle synthesis, especially chirality evolution process of 432 helicoid series.

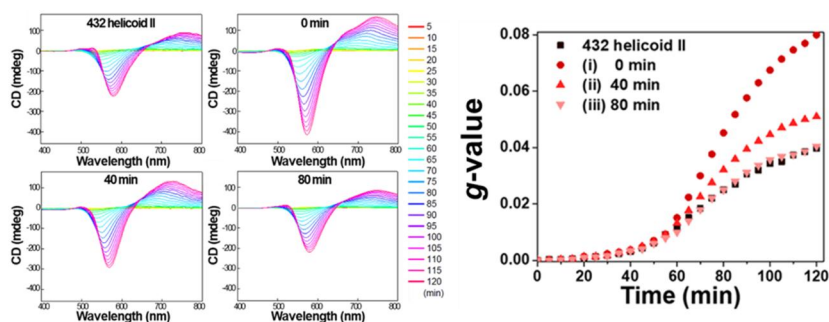


Figure 6. 9 T20 oligomer insertion time control during 432 helicoid II nanoparticle synthesis. Depending on the insertion time, chiroptic response change has been changed.

## 6.5 Single-Stranded DNA induced Chiral Nanoparticle

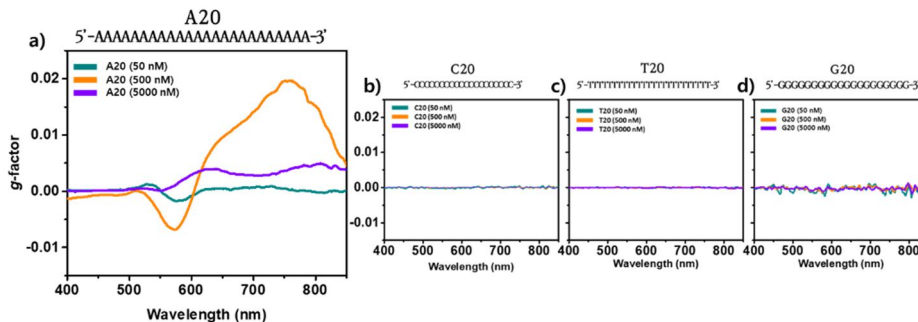


Figure 6. 10 Chiroptic response of DNA induced chiral nanoparticle. G-factor diagram of a) Adenine-20mer induced nanoparticle, b) Cytosine-20mer induced nanoparticle, c) Thymine-20mer induced nanoparticle, and d) Guanine-20mer induced nanoparticles.

In order to find possibilities of inducing chirality using only ssDNA, each nucleobases, Adenine, Cytosine, Guanine, and Thymine, have been used for chiral nanoparticle synthesis. Detailed synthesis protocol has been provided in chapter 3, experimental sections. Briefly explaining, for the synthesis of DNA induced chiral nanoparticle, CTAB as surfactant, ascorbic acid as reducing agent, gold octahedron nanoparticle as seed nanoparticle, and  $\text{HAuCl}_4$  as metal ion precursor were used. For the chirality inducing agent, each nucleobase has been purchased and used without further purification. In order to test the possibility of chirality generation using ssDNA, 20-mer oligomer of each nucleobase has been used for chiral nanoparticle synthesis. Interestingly, Adenine 20-mer oligomer specifically shows chirality evolution behavior. Among the wide concentration range of 50nM, 500nM and 5000nM, Adenine induced chiroptic response from all of these concentration ranges as shown in figure 6.10 a). This is clearly distinguished from nanoparticles synthesized with other nucleobases as shown in figure 6.10 b), c), and d). For all nucleobase such as Cytosine 20-mer, Thymine-20mer, and Guanine

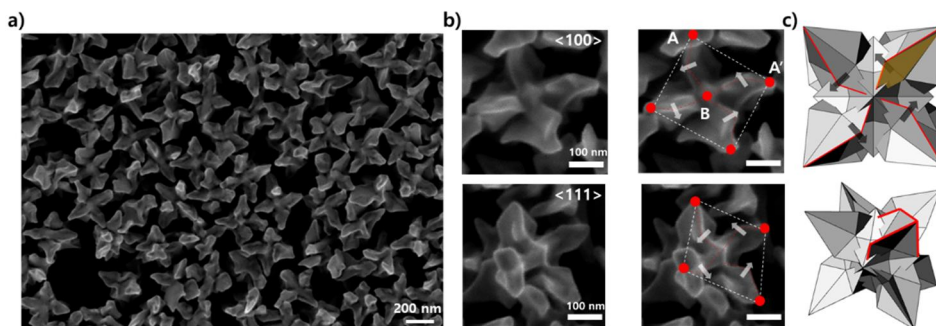


Figure 6.11 SEM images of DNA induced chiral nanoparticles. a) low-magnification SEM images of nanoparticles showing uniform structures. b) High-magnification SEM images of DNA induced chiral nanoparticle with its chiral rotation highlighted with red dots and lines. c) schematic image of synthesized DNA induced chiral nanoparticle.

20-mer, overall all ranges of concentrations, no chiroptic response has been observed. This clearly indicates that Adenine nucleobase serves a specific role during chirality evolution during DNA induced chiral nanoparticle synthesis.

In order to further understand the chiral nanoparticle induced by adenine oligomer, subsequent morphology analysis was conducted. As shown in figure 6.11 a), uniform nanoparticle with average edge length of around 200nm has been synthesized. For more detailed analysis of morphology, we could focus on the high-magnification SEM images show in figure 6.11 b) and schematic shown in figure 6.11 c). Figure 6.11 b) is a SEM images of DNA induced chiral gold nanoparticle viewed from  $\langle 100 \rangle$  direction and  $\langle 111 \rangle$  direction. From the image, we could notice that there exists four distinct chiral arm generation view from  $\langle 100 \rangle$  perspective. Also, a protruded center point on each face of the cubical boundary exists. As for the chiral feature analysis, looking at figure 6.11 b), the AB boundary noted with red line shows counter-clockwise rotation round the protruded center point. This is more easily visualized on the figure 6.11 c) schematic. From this

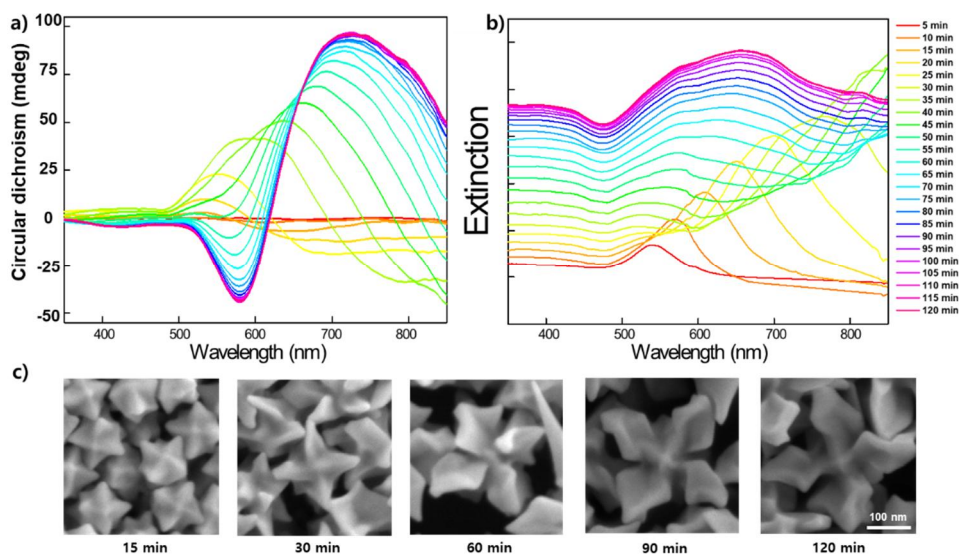


Figure 6.12 Time-variant chiroptic response and morphology analysis of DNA induced chiral gold nanoparticle.

morphology analysis, we were able to find out that nanoparticle shows a fairly uniform chiral arm structures with counter-clockwise motif generation.

In order to find out the development of chirality during DNA induced nanoparticle, nanoparticle synthesis have been analyzed respect to reaction time in terms of CD response and SEM measured morphology. Figure 6.12 a) and b) shows the progressive generation of CD response and absorption spectra measured every 5 minutes of the reaction. For the time-variant measurement of CD, growth solution was prepared in quartz cuvette and reaction was proceeded inside the CD measurement set-up. For SEM analysis shown in figure 6.12 c), each nanoparticle growth solution was prepared and the reaction was stopped at each noted reaction time for further characterization by SEM. As shown, CD response shows inversion after the 30 minutes of the growth while absorption spectra continue to shift in longer wave length as nanoparticle size increases. The development of DNA

induced nanoparticle is more clearly visible from SEM morphology analysis. As shown in figure 6.12 c), morphology analyzed for 15 minutes, 30 minutes, 60 minutes, 90 minutes and 120minutes of the reaction time shows gradual development of chiral morphology. From the start of the reaction to 30 minutes of the synthesis, high-index generation and partial chiral edge tilting is observed. However, from 60 minutes of the nanoparticle synthesis, chiral arm generation is clearly visible with chiral gap formed in-between chiral arms. As reaction time increases, nanoparticle size increases with chiral arm structures become more clearly visible. It is difficult to directly relate the spectral inversion with the chiral morphology change without simulation, it is expected morphology change such as chiral gap formation influences resulting chiroptic response.

## 6.6 Enantiospecific Interaction of Nucleobases and Gold Chiral Surface

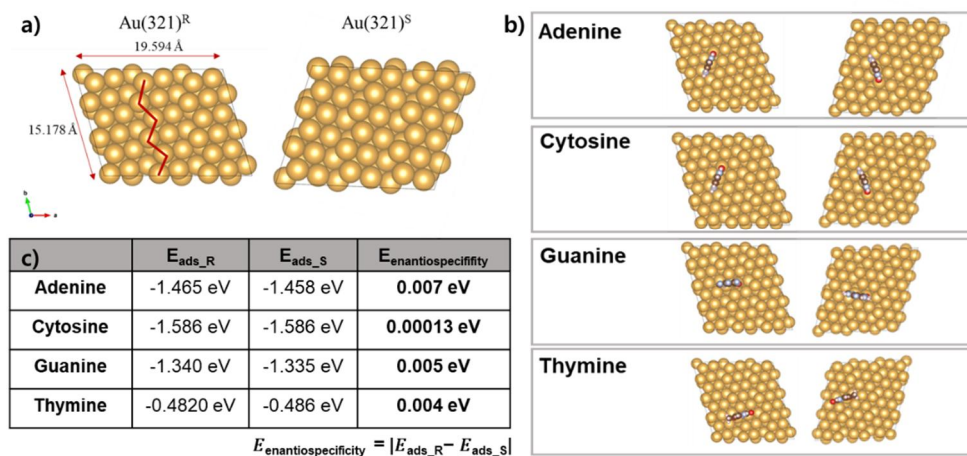


Figure 6. 13 DFT simulation of nucleobase interaction with chiral gold surface. a) generated chiral high-index gold surface, b) each nucleobase introduced to the unit cell of high-index chiral surface, and c) energy calculation upon introduction of nucleobase to unit cells.

For more clear understanding of the reason why Adenine serves a special role of generating chirality among others, we have conducted DFT simulation. For the simulation, we have generated  $\text{Au}(321)^R$  and  $\text{Au}(321)^S$  surface and introduced nucleobases as shown in figure 6.13 a) and b). For the quantified understanding of chirality inducing mechanism, upon addition of a nucleobase, we measured the adsorption energy on each surfaces and the relative energy differences to find out enantiospecificity.  $E_{\text{enantiospecificity}}$  was defined as following.

$$E_{\text{enantiospecificity}} = |E_{\text{ads}_R} - E_{\text{ads}_S}|$$

Progressively, in a same manner, by increasing the number of introduced

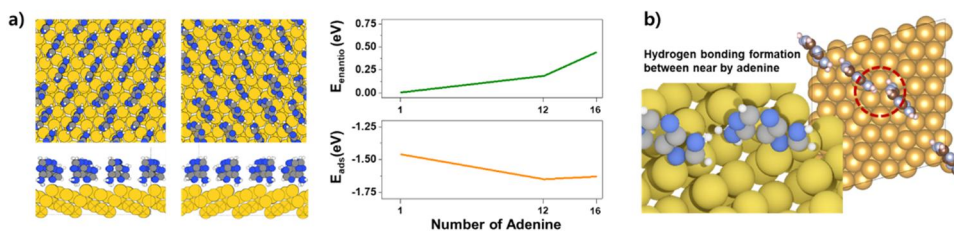


Figure 6. 14 Interaction of chiral gold surface and Adenine respect to increase in number of Adenine. a) Energetically stable orientation of Adenine and b) schematic of hydrogen bonding formation between neighboring Adenine

nucleobase, oligomer scale calculation was further conducted to understand interaction between each nucleobase and gold surface.

As shown in figure 6.13 c), Adenine shows the highest  $E_{\text{enantiomericity}}$  among all other nucleobases. However, the differences are no significant and it is difficult to understand the entire behavior of nucleobases on chiral gold surface. Therefore, number of nucleobase in a unit cell of generated chiral high-index surface has been increased. As shown in figure 6.14 a), by increase of number of Adenine introduced to the chiral gold surface,  $E_{\text{enantiomericity}}$  increases while the binding affinity increases as well. Also, surface interacting Adenine energetically favors a unidirectional alignment when each nucleobase being placed at the kink cite of the surface. As shown in figure 6.14 b), this alignment is in orientation which each nucleobase forms hydrogen bonding with each other creating a chain of adenine to induce overall chirality. However, Cytosine and Guanine cases both shows decreases in binding affinity to gold despite guanine showing  $E_{\text{enantiomericity}}$  increase as shown in figure 6.15 a) b) and c). Also, the orientation of the nucleobase on gold chiral surface is different for each nucleobase. In the case of Thymine, the orientation of nucleobases are not as aligned as Adenine and no significant increase of  $E_{\text{enantiomericity}}$  or adsorption tendency was observed. On the other hand, alignment of nucleobases can be observed in the case of Cytosine but

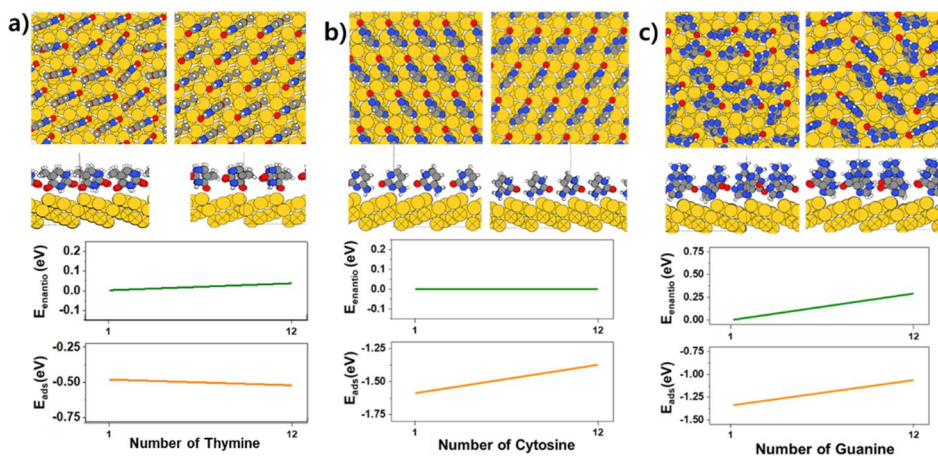


Figure 6. 15 Energetically stable orientation and adsorption energy calculation respect to increase in nucleobase number introduced to the system in the case of a) Thymine, b) Cytosine, and c) Guanine

$E_{\text{enantiio}}$  does not show significant increase and adsorption energy shows decreasing trend as number of nucleobases in the unit cell of gold surface increases. It is assumed that due to interaction between nearby nucleobases, the interaction between nucleobase and gold surface decreases. In the case of Guanine, there are no formation of this alignment which is believed to be the key aspect for chirality development. Therefore, from this result, we can learn that hydrogen bonding in between neighboring Adenine induces chiral interaction between oligomer and chiral gold surface, directing the nanoparticle growth in an asymmetric manner.

## 6.7 Sequence Pattern Dependent Chirality Evolution

One of the most intriguing aspect of using DNA as shape modifier is that its sequence can be controlled as wanted with ease. Therefore, we have tested modification of the sequence structures and composition for chirality inducing ability. For the modification of the sequence, sequence length and sequence composition has been controlled while Adenine, which is a key component in inducing chirality, was used at all times in various forms. Therefore, the modification was demonstrated in two approaches: 1) Adenine based sequence length control from 10-mer Adenine oligomers to 50-mer Adenine oligomers and 2) Adenine and Cytosine based sequence pattern control using 12-mer oligomer for most versatile patterns.

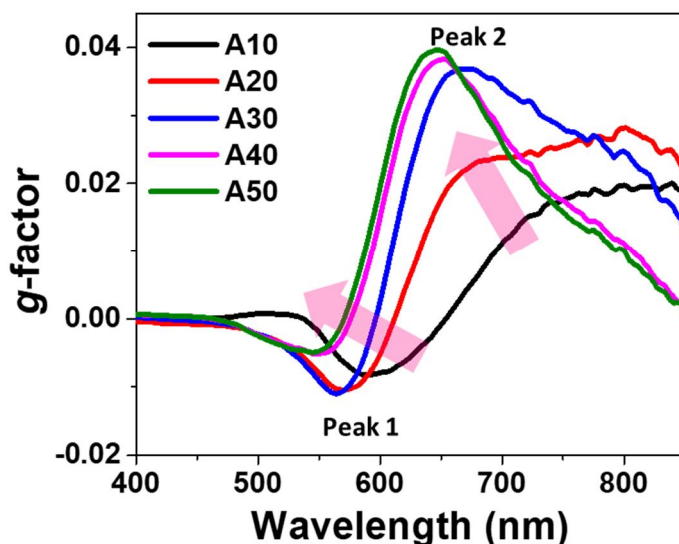


Figure 6. 16 Change in chiroptic response respect to change in Adenine oligomer sequence length. Peak 1 and Peak 2 notify each distinct chiroptic peaks while each arrows denote the tendency respect to increase in Adenine oligomer length.

Sequence length dependent chirality control has been demonstrated. As shown in figure 6.16, Adenine sequence has been controlled from A10mer to A50mer. For the single nucleobase oligomer, it was only possible to synthesize maximum of 50-mer oligomer, therefore, further increase of Adenine oligomer length for nanoparticle synthesis was not conducted. For the synthesis of the nanoparticle, synthesis condition was maintained constant for all experiments except the oligomer length. As shown, as the length of Adenine oligomer increases, the maximum chiroptic response increases while the overall spectrum shifts to shorter wavelength.

In more detail, it is possible to distinguish two chiroptic peaks which is denoted as peak 1 and peak 2. Peak 1 is down-ward shaped chiroptic response while peak 2 is up-ward spectrum. As Adenine oligomer length increases, peak 1

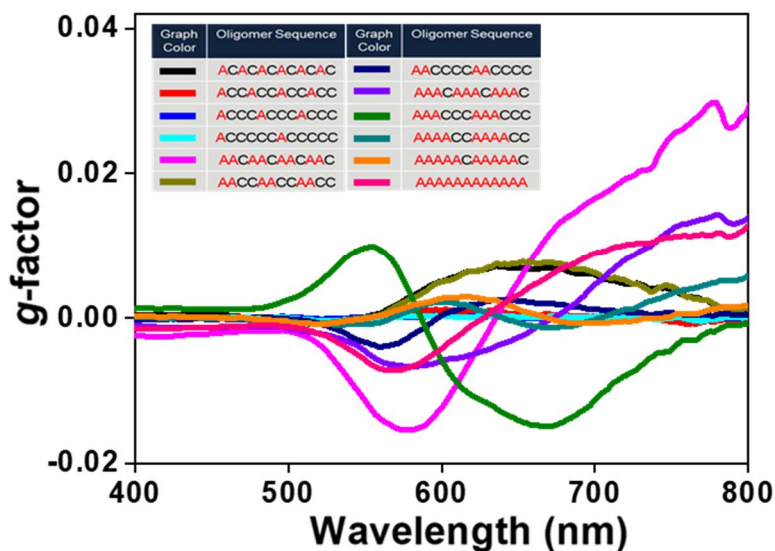


Figure 6. 17 Change in sequence pattern of Adenine and Cytosine based 12-mer oligomer.

gradually diminishes as peak to chiroptic signal is increasing. This indicates that by the modulation of the oligomer length, it is possible to control the chiroptic response.

Furthermore, sequence pattern was changed by altering composition and relative orders of Adenine and Cytosine nucleobase in an oligomer. For the convenient testing of various possible combinations, 12-mer oligomer consisting of Adenine and Cytosine only has been tested. As shown in figure 6.17, change in Adenine and Cytosine combination induced various chiroptic response. While it is at difficulty to fully understand how this chirality is induced and how to control it as desired, we have preliminarily provided a basic design principle under the guideline of sequence pattern generating highest chiroptic response regardless of peak positions or spectral shape. While the number of consecutive Adenine is same, with the increasing number of Adenine in the entire sequence yields higher chiroptic response. This can be inferred from the fact that Adenine serves a critical role in chirality evolution. Also, while the number of consecutive Adenine is same, with the decreasing spacing between Adenine, it appears the highest chiroptic response. This is expected to be from the fact that chirality has a close relationship with hydrogen bonding formation between neighboring atoms, therefore, introducing a spacer between Adenine will affect this hydrogen bonding formation mechanism. While these guidelines are not sufficient enough to truly program desired properties in to chiral nanoparticles, yet, this could provide a starting platform for DNA based programmable chirality evolution.

## 6.8 Surface Chemistry: CTAB vs Adenine

While these Adenine based oligomers are interacting at the surface of gold nanoparticle while chiral growth, there also exists CTAB surfactant present at the growth solution and the nanoparticle surface. Therefore, in the seed-mediated based morphology control, understanding interaction between surface present chemicals. Therefore, in order to establish further understanding on how CTAB and DNA oligomers are co-existing near gold nanoparticle surface while chirality evolution, synthesis was conducted by varying concentrations of Adenine and CTAB individually.

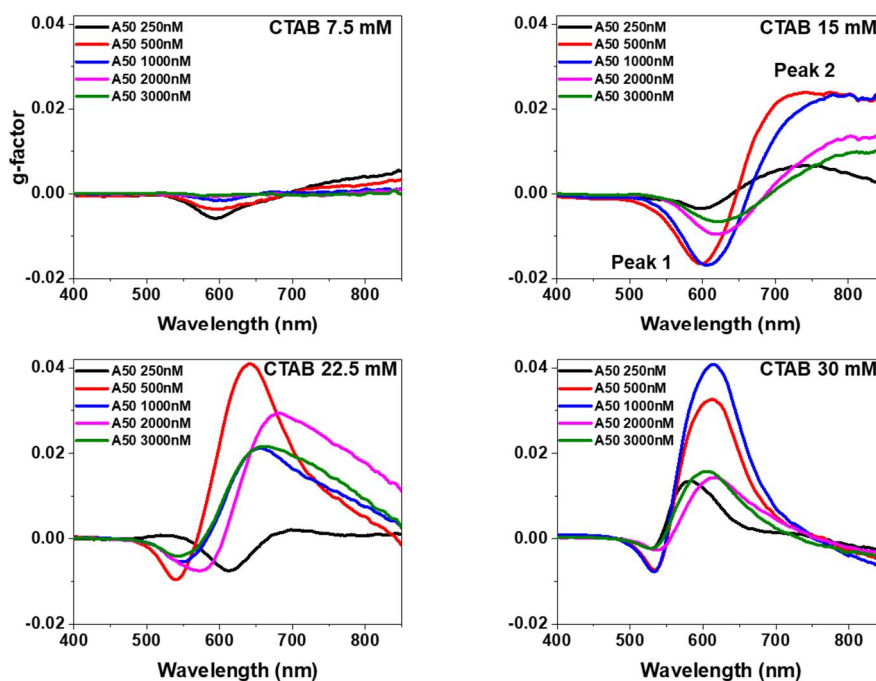


Figure 6. 18 Chiroptic response diagram respect to CTAB and A50mer oligomer concentration during chiral nanoparticle synthesis.

As shown in figure 6.18, CTAB concentration strongly affects the spectral shape and maximum chiroptic response. For low CTAB concentrations, A50mer oligomer did not induce significant chiroptic response while most of optical response was present as peak 1. However, with the increase of CTAB concentrations, overall max chiroptic response have increased and peak 2 gradually become more dominant. This interesting behavior is more clearly visible when maximum g-factor of peak 1 and peak 2 are plotted respect to synthesis conditions in a g-factor diagram. As shown in figure 6.19, peak 1 and peak 2 maximum g-factor regardless of peak positions are displayed. From this diagram, we could clearly see that highest chiroptic response measured region differs between peak 1 and peak 2. For peak 1, lower CTAB regions shows highest chiroptic response while peak 2 shows a preferential development of chirality at higher CTAB concentrations. Also, each red boxes indicate the max chiroptic response at given CTAB concentrations. From this, we could observe that there exists a slight linear relationship which with the increase of CTAB concentration used during the nanoparticle synthesis, higher Adenine concentration is required for most efficient chirality evolution. This indicate that there exists a competing

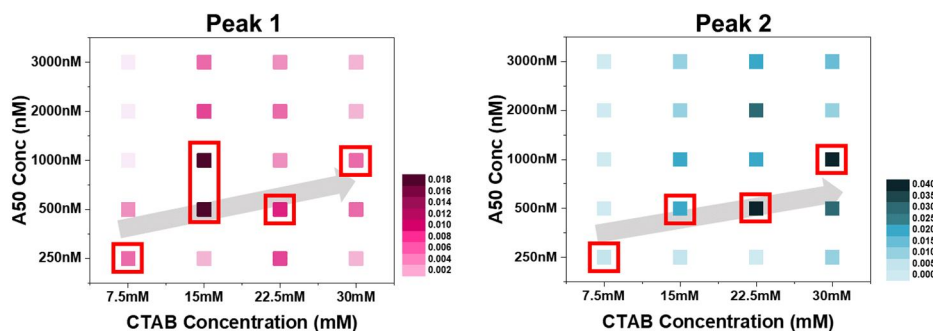


Figure 6. 19 G-factor diagram of CTAB vs Adenine concentration during DNA induced chiral nanoparticle synthesis. Each red boxes indicate the highest g-factor regardless of peak positions at each CTAB concentrations.

relationship between CTAB and Adenine oligomer which has been observed in previous chirality evolution based on seed-mediated method.

## 6.9 Conclusion

For more versatile application of chiral nanomaterials, it is required to generate chiroptic responses to meet the demand of each application. Therefore, finding possibilities of programming chirality as desired to nanomaterials could be a new step-up for chiral nanomaterials generation. As we have previously demonstrated chirality transfer from organic to inorganic in single amino acids or tri-peptide level, inducing chirality at longer and sequence programmable oligomer could widen our synthesis platform to another level. In the context of sequence programmable oligomer, DNA has been used for millions of years in nature for its excellent controllability and programmability. With the technological development, nowadays, we also have feasibility to easily and economically program DNA sequence as desired. Due to each nucleobase having a distinct surface interaction with metals, potential chirality evolution ability of ssDNA oligomer has been tested. At first, thymine oligomer has been added to 432 helicoid II synthesis which conventionally use glutathione molecule as chirality inducer. Interestingly, upon the addition of thymine oligomer to assist 432 helicoid II synthesis, significant enhancement of chiroptic response was observed while introducing only Thymine oligomer did not show any chirality evolution. From this result, it was possible to conclude that ssDNA could participate during nanoparticle morphology control. Furthermore, chirality evolution using various ssDNA oligomer nucleobases was tested while the DNA was the only source of chirality during the nanoparticle synthesis. Interestingly, Adenine oligomer showed chirality evolution capability at wide ranges of concentrations, other nucleobases did not show any chiral development. To understand this adenine specific chirality evolution, DFT calculation was conducted, which shows enantiospecific binding affinity of Adenine oligomer shows increasing trend by forming hydrogen bonding with each other. This behavior was not observed for other bases which supports our experimental data of only Adenine showing

chirality evolution. For further modulation and the experimentally demonstrate potential programmability of DNA based chiral nanoparticle synthesis, DNA sequence control was conducted. Modulation of chirality evolution by changing sequence length and pattern was observed while relative surfactant concentration also showed effects on chirality evolution. Based on this results, we were able construct a general rule of thumb for using ssDNA as chirality inducer which we believe could provide a platform for chirality programmable DNA based chiral nanomaterial synthesis.

## 6.10 Bibliography

- (1) Tomasetti, C.; Li, L.; Vogelstein, B. Stem Cell Divisions, Somatic Mutations, Cancer Etiology, and Cancer Prevention. *Science* (80-. ). **2017**, *355* (6331), 1330–1334. <https://doi.org/10.1126/science.aaf9011>.
- (2) Basu, A. DNA Damage, Mutagenesis and Cancer. *Int. J. Mol. Sci.* **2018**, *19* (4), 970. <https://doi.org/10.3390/ijms19040970>.
- (3) Li, H.; Yang, Y.; Hong, W.; Huang, M.; Wu, M.; Zhao, X. Applications of Genome Editing Technology in the Targeted Therapy of Human Diseases: Mechanisms, Advances and Prospects. *Signal Transduct. Target. Ther.* **2020**, *5* (1), 1. <https://doi.org/10.1038/s41392-019-0089-y>.
- (4) Li, Q.; Qin, Z.; Wang, Q.; Xu, T.; Yang, Y.; He, Z. Applications of Genome Editing Technology in Animal Disease Modeling and Gene Therapy. *Comput. Struct. Biotechnol. J.* **2019**, *17*, 689–698. <https://doi.org/10.1016/j.csbj.2019.05.006>.
- (5) Ma, D.; Liu, F. Genome Editing and Its Applications in Model Organisms. *Genomics. Proteomics Bioinformatics* **2015**, *13* (6), 336–344. <https://doi.org/10.1016/j.gpb.2015.12.001>.
- (6) Gaj, T.; Sirk, S. J.; Shui, S.; Liu, J. Genome-Editing Technologies: Principles and Applications. *Cold Spring Harb. Perspect. Biol.* **2016**, *8* (12), a023754. <https://doi.org/10.1101/cshperspect.a023754>.
- (7) Hsu, P. D.; Lander, E. S.; Zhang, F. Development and Applications of CRISPR-Cas9 for Genome Engineering. *Cell* **2014**, *157* (6), 1262–1278. <https://doi.org/10.1016/j.cell.2014.05.010>.

- (8) Ceze, L.; Nivala, J.; Strauss, K. Molecular Digital Data Storage Using DNA. *Nat. Rev. Genet.* **2019**, *20* (8), 456–466.  
<https://doi.org/10.1038/s41576-019-0125-3>.
- (9) Wang, Y.; Noor-A-Rahim, M.; Zhang, J.; Gunawan, E.; Guan, Y. L.; Poh, C. L. High Capacity DNA Data Storage with Variable-Length Oligonucleotides Using Repeat Accumulate Code and Hybrid Mapping. *J. Biol. Eng.* **2019**, *13* (1), 89. <https://doi.org/10.1186/s13036-019-0211-2>.
- (10) Choi, Y.; Ryu, T.; Lee, A. C.; Choi, H.; Lee, H.; Park, J.; Song, S.-H.; Kim, S.; Kim, H.; Park, W.; et al. High Information Capacity DNA-Based Data Storage with Augmented Encoding Characters Using Degenerate Bases. *Sci. Rep.* **2019**, *9* (1), 6582. <https://doi.org/10.1038/s41598-019-43105-w>.
- (11) Antkowiak, P. L.; Lietard, J.; Darestani, M. Z.; Somoza, M. M.; Stark, W. J.; Heckel, R.; Grass, R. N. Low Cost DNA Data Storage Using Photolithographic Synthesis and Advanced Information Reconstruction and Error Correction. *Nat. Commun.* **2020**, *11* (1), 5345.  
<https://doi.org/10.1038/s41467-020-19148-3>.
- (12) Shipman, S. L.; Nivala, J.; Macklis, J. D.; Church, G. M. CRISPR–Cas Encoding of a Digital Movie into the Genomes of a Population of Living Bacteria. *Nature* **2017**, *547* (7663), 345–349.  
<https://doi.org/10.1038/nature23017>.
- (13) Carnerero, J. M.; Jimenez-Ruiz, A.; Castillo, P. M.; Prado-Gotor, R. Covalent and Non-Covalent DNA-Gold-Nanoparticle Interactions: New Avenues of Research. *ChemPhysChem* **2017**, *18* (1), 17–33.

<https://doi.org/10.1002/cphc.201601077>.

- (14) Mirau, P. A.; Smith, J. E.; Chávez, J. L.; Hagen, J. A.; Kelley-Loughnane, N.; Naik, R. Structured DNA Aptamer Interactions with Gold Nanoparticles. *Langmuir* **2018**, *34* (5), 2139–2146. <https://doi.org/10.1021/acs.langmuir.7b02449>.
- (15) Cárdenas, M.; Barauskas, J.; Schillén, K.; Brennan, J. L.; Brust, M.; Nylander, T. Thiol-Specific and Nonspecific Interactions between DNA and Gold Nanoparticles. *Langmuir* **2006**, *22* (7), 3294–3299. <https://doi.org/10.1021/la0530438>.
- (16) He, Q.; Wu, Q.; Feng, X.; Liao, Z.; Peng, W.; Liu, Y.; Peng, D.; Liu, Z.; Mo, M. Interfacing DNA with Nanoparticles: Surface Science and Its Applications in Biosensing. *Int. J. Biol. Macromol.* **2020**, *151*, 757–780. <https://doi.org/10.1016/j.ijbiomac.2020.02.217>.
- (17) Jamdagni, P.; Khatri, P.; Rana, J. S. Nanoparticles Based DNA Conjugates for Detection of Pathogenic Microorganisms. *Int. Nano Lett.* **2016**, *6* (3), 139–146. <https://doi.org/10.1007/s40089-015-0177-0>.
- (18) Park, S. DNA Conjugation to Nanoparticles; 2013; pp 9–18. [https://doi.org/10.1007/978-1-62703-462-3\\_2](https://doi.org/10.1007/978-1-62703-462-3_2).
- (19) Deka, J.; Mojumdar, A.; Parisse, P.; Onesti, S.; Casalis, L. DNA-Conjugated Gold Nanoparticles Based Colorimetric Assay to Assess Helicase Activity: A Novel Route to Screen Potential Helicase Inhibitors. *Sci. Rep.* **2017**, *7* (1), 44358. <https://doi.org/10.1038/srep44358>.
- (20) Zhao, W.; Lin, L.; Hsing, I.-M. Rapid Synthesis of DNA-Functionalized Gold Nanoparticles in Salt Solution Using Mononucleotide-Mediated

- Conjugation. *Bioconjug. Chem.* **2009**, *20* (6), 1218–1222.  
<https://doi.org/10.1021/bc900080p>.
- (21) Wang, C.; Zhang, H.; Zeng, D.; San, L.; Mi, X. DNA Nanotechnology Mediated Gold Nanoparticle Conjugates and Their Applications in Biomedicine. *Chinese J. Chem.* **2016**, *34* (3), 299–307.  
<https://doi.org/10.1002/cjoc.201500839>.
- (22) Abu-Salah, K. M.; Ansari, A. A.; Alrokayan, S. A. DNA-Based Applications in Nanobiotechnology. *J. Biomed. Biotechnol.* **2010**, *2010*, 1–15. <https://doi.org/10.1155/2010/715295>.
- (23) Lee, A. J.; Wälti, C. DNA Nanostructures: A Versatile Lab-Bench for Interrogating Biological Reactions. *Comput. Struct. Biotechnol. J.* **2019**, *17*, 832–842. <https://doi.org/10.1016/j.csbj.2019.06.013>.
- (24) Tam, D. Y.; Lo, P. K. Multifunctional DNA Nanomaterials for Biomedical Applications. *J. Nanomater.* **2015**, *2015*, 1–21.  
<https://doi.org/10.1155/2015/765492>.
- (25) Bujold, K. E.; Lacroix, A.; Sleiman, H. F. DNA Nanostructures at the Interface with Biology. *Chem* **2018**, *4* (3), 495–521.  
<https://doi.org/10.1016/j.chempr.2018.02.005>.
- (26) Baig, M. M. F. A.; Lai, W.-F.; Akhtar, M. F.; Saleem, A.; Ahmed, S. A.; Xia, X.-H. DNA Nanotechnology as a Tool to Develop Molecular Tension Probes for Bio-Sensing and Bio-Imaging Applications: An up-to-Date Review. *Nano-Structures & Nano-Objects* **2020**, *23*, 100523.  
<https://doi.org/10.1016/j.nanoso.2020.100523>.
- (27) Chandrasekaran, A. R.; Anderson, N.; Kizer, M.; Halvorsen, K.; Wang,

- X. Beyond the Fold: Emerging Biological Applications of DNA Origami. *ChemBioChem* **2016**, *17* (12), 1081–1089.  
<https://doi.org/10.1002/cbic.201600038>.
- (28) Liu, B.; Liu, J. Freezing-Driven DNA Adsorption on Gold Nanoparticles: Tolerating Extremely Low Salt Concentration but Requiring High DNA Concentration. *Langmuir* **2019**, *35* (19), 6476–6482.  
<https://doi.org/10.1021/acs.langmuir.9b00746>.
- (29) Xu, Y.; Huang, K.; Lopez, A.; Xu, W.; Liu, J. Freezing Promoted Hybridization of Very Short DNA Oligonucleotides. *Chem. Commun.* **2019**, *55* (69), 10300–10303. <https://doi.org/10.1039/C9CC04608A>.
- (30) Wu, R.; Jiang, L.-P.; Zhu, J.-J.; Liu, J. Effects of Small Molecules on DNA Adsorption by Gold Nanoparticles and a Case Study of Tris(2-Carboxyethyl)Phosphine (TCEP). *Langmuir* **2019**, *35* (41), 13461–13468.  
<https://doi.org/10.1021/acs.langmuir.9b02652>.
- (31) Yang, J.; Pong, B.-K.; Lee, J. Y.; Too, H.-P. Dissociation of Double-Stranded DNA by Small Metal Nanoparticles. *J. Inorg. Biochem.* **2007**, *101* (5), 824–830. <https://doi.org/10.1016/j.jinorgbio.2007.01.014>.
- (32) Pei, H.; Li, F.; Wan, Y.; Wei, M.; Liu, H.; Su, Y.; Chen, N.; Huang, Q.; Fan, C. Designed Diblock Oligonucleotide for the Synthesis of Spatially Isolated and Highly Hybridizable Functionalization of DNA–Gold Nanoparticle Nanoconjugates. *J. Am. Chem. Soc.* **2012**, *134* (29), 11876–11879. <https://doi.org/10.1021/ja304118z>.
- (33) Zhu, D.; Chao, J.; Pei, H.; Zuo, X.; Huang, Q.; Wang, L.; Huang, W.; Fan, C. Coordination-Mediated Programmable Assembly of Unmodified

Oligonucleotides on Plasmonic Silver Nanoparticles. *ACS Appl. Mater. Interfaces* **2015**, *7* (20), 11047–11052.  
<https://doi.org/10.1021/acsami.5b03066>.

- (34) Zhu, D.; Song, P.; Shen, J.; Su, S.; Chao, J.; Aldalbahi, A.; Zhou, Z.; Song, S.; Fan, C.; Zuo, X.; et al. PolyA-Mediated DNA Assembly on Gold Nanoparticles for Thermodynamically Favorable and Rapid Hybridization Analysis. *Anal. Chem.* **2016**, *88* (9), 4949–4954.  
<https://doi.org/10.1021/acs.analchem.6b00891>.
- (35) Lu, W.; Wang, L.; Li, J.; Zhao, Y.; Zhou, Z.; Shi, J.; Zuo, X.; Pan, D. Quantitative Investigation of the Poly-Adenine DNA Dissociation from the Surface of Gold Nanoparticles. *Sci. Rep.* **2015**, *5* (1), 10158.  
<https://doi.org/10.1038/srep10158>.
- (36) Huang, Z.; Liu, B.; Liu, J. Parallel Polyadenine Duplex Formation at Low PH Facilitates DNA Conjugation onto Gold Nanoparticles. *Langmuir* **2016**, *32* (45), 11986–11992.  
<https://doi.org/10.1021/acs.langmuir.6b03253>.
- (37) Kuzyk, A.; Schreiber, R.; Fan, Z.; Pardatscher, G.; Roller, E.-M.; Högele, A.; Simmel, F. C.; Govorov, A. O.; Liedl, T. DNA-Based Self-Assembly of Chiral Plasmonic Nanostructures with Tailored Optical Response. *Nature* **2012**, *483* (7389), 311–314. <https://doi.org/10.1038/nature10889>.
- (38) Schreiber, R.; Luong, N.; Fan, Z.; Kuzyk, A.; Nickels, P. C.; Zhang, T.; Smith, D. M.; Yurke, B.; Kuang, W.; Govorov, A. O.; et al. Chiral Plasmonic DNA Nanostructures with Switchable Circular Dichroism. *Nat. Commun.* **2013**, *4* (1), 2948. <https://doi.org/10.1038/ncomms3948>.

- (39) Lan, X.; Zhou, X.; McCarthy, L. A.; Govorov, A. O.; Liu, Y.; Link, S. DNA-Enabled Chiral Gold Nanoparticle–Chromophore Hybrid Structure with Resonant Plasmon–Exciton Coupling Gives Unusual and Strong Circular Dichroism. *J. Am. Chem. Soc.* **2019**, *141* (49), 19336–19341. <https://doi.org/10.1021/jacs.9b08797>.
- (40) Lin, C.; Ke, Y.; Li, Z.; Wang, J. H.; Liu, Y.; Yan, H. Mirror Image DNA Nanostructures for Chiral Supramolecular Assemblies. *Nano Lett.* **2009**, *9* (1), 433–436. <https://doi.org/10.1021/nl803328v>.
- (41) Nguyen, L.; Dass, M.; Ober, M. F.; Besteiro, L. V.; Wang, Z. M.; Nickel, B.; Govorov, A. O.; Liedl, T.; Heuer-Jungemann, A. Chiral Assembly of Gold–Silver Core–Shell Plasmonic Nanorods on DNA Origami with Strong Optical Activity. *ACS Nano* **2020**, *14* (6), 7454–7461. <https://doi.org/10.1021/acsnano.0c03127>.
- (42) Cao, Y.; Duan, Y.; Han, L.; Che, S. Hierarchical Chirality Transfer in the Formation of Chiral Silica Fibres with DNA–Porphyrin Co-Templates. *Chem. Commun.* **2017**, *53* (41), 5641–5644. <https://doi.org/10.1039/C7CC02382K>.
- (43) Ma, W.; Kuang, H.; Xu, L.; Ding, L.; Xu, C.; Wang, L.; Kotov, N. A. Attomolar DNA Detection with Chiral Nanorod Assemblies. *Nat. Commun.* **2013**, *4* (1), 2689. <https://doi.org/10.1038/ncomms3689>.
- (44) Chen, W.; Bian, A.; Agarwal, A.; Liu, L.; Shen, H.; Wang, L.; Xu, C.; Kotov, N. A. Nanoparticle Superstructures Made by Polymerase Chain Reaction: Collective Interactions of Nanoparticles and a New Principle for Chiral Materials. *Nano Lett.* **2009**, *9* (5), 2153–2159. <https://doi.org/10.1021/nl900726s>.

- (45) Zhao, Y.; Xu, L.; Kuang, H.; Wang, L.; Xu, C. Asymmetric and Symmetric PCR of Gold Nanoparticles: A Pathway to Scaled-up Self-Assembly with Tunable Chirality. *J. Mater. Chem.* **2012**, *22* (12), 5574. <https://doi.org/10.1039/c2jm15800k>.
- (46) Wang, Z.; Zhang, J.; Ekman, J. M.; Kenis, P. J. A.; Lu, Y. DNA-Mediated Control of Metal Nanoparticle Shape: One-Pot Synthesis and Cellular Uptake of Highly Stable and Functional Gold Nanoflowers. *Nano Lett.* **2010**, *10* (5), 1886–1891. <https://doi.org/10.1021/nl100675p>.
- (47) Satyavolu, N. S. R.; Tan, L. H.; Lu, Y. DNA-Mediated Morphological Control of Pd–Au Bimetallic Nanoparticles. *J. Am. Chem. Soc.* **2016**, *138* (50), 16542–16548. <https://doi.org/10.1021/jacs.6b10983>.
- (48) Satyavolu, N. S. R.; Pishvaresfahani, N.; Tan, L. H.; Lu, Y. DNA-Encoded Morphological Evolution of Bimetallic Pd@Au Core-Shell Nanoparticles from a High-Indexed Core. *Nano Res.* **2018**, *11* (9), 4549–4561. <https://doi.org/10.1007/s12274-018-2035-7>.
- (49) Satyavolu, N. S. R.; Loh, K. Y.; Tan, L. H.; Lu, Y. Discovery of and Insights into DNA “Codes” for Tunable Morphologies of Metal Nanoparticles. *Small* **2019**, *15* (26), 1900975. <https://doi.org/10.1002/sml.201900975>.

# **Chapter 7. Expansion of Material Selection for Seed-mediated Chiral Nanoparticle Synthesis**

## **7.1 Introduction**

In the context of synthesizing chiral nanomaterials in a way to meet the desired requirements for various application, expansion of material selection for chiral nanomaterials synthesis is crucial. Amino acid and peptide induce nanoparticle synthesis method deals with chirality transfer from organic molecules to inorganic materials. However, the synthesis method has only been demonstrated using plasmonic gold as the material for nanoparticle synthesis. In this sense, expanding the significance of our synthesis method, transfer of naturally occurring chirality and optical behavior of organic molecules into inorganic nanocrystals, finding an appropriate material for other applications is necessary. Therefore, we explore the potential application of the demonstrated synthesis method using other metal for shape controlled nanoparticle synthesis and investigate the role of involved chiral molecules by comparison with the previous reported synthesis of chiral gold nanoparticle.

In terms of wider application of catalytic material, chiral catalysis and enantiomeric sensing are huge areas of research. In many previous studies, people have tried to perform an effective asymmetric catalysis for enantiomeric pure chemical or pharmaceutical product.<sup>1-4</sup> Enantiomers of identical chemicals often show much different biological activity.<sup>5,6</sup> Especially since the case of Thalidomide, finding enantio-pure chemical or pharmaceutical product has significantly highlighted. For this process, it is inevitable for an efficient catalysis or nanostructure development. Developing palladium based chiral structures could provide a solution to this problem. Palladium has significant advantages in its spectrum of potential applications. The high catalytic activity of palladium could

significantly enhance the current level of technology in asymmetric organic catalysis and enantioselective sensing with wide versatility.<sup>4-11</sup> While importance of chirality control is steadily increasing, current state of chirality control using palladium nanoparticle is limited to cases where they use chiral ligands to induce chirality in product. However, intrinsic and morphologically chiral palladium platform is necessary as catalytic and sensing applications using nanoparticle are closely related with the exposed facet control.

Another reason for choosing palladium as an alternative source is due to the ease of applying palladium source in to the already existing synthetic platform of aqueous based seed mediated method. In the previous researches, palladium nanoparticle morphology and exposed facet control based on the seed-mediated method has been extensively studied due to the ease of control. Shao et al. reported the synthesis of palladium nanocrystals in the form of concave nanocubes to right bipyramid structures by controlling the reduction kinetic.<sup>12</sup> Yang et al. experimentally demonstrated the control of nanoparticle morphology during gold@palladium core-shell nanoparticle in the form of octahedral shape to truncated and concave cubic structures.<sup>13</sup> Addition to these representative examples, there have been number of studies reported for seed-mediated method on palladium nanoparticles, but to our knowledge, no chiral structures have been reported.<sup>13-16</sup>

For the chirality determination of the chiral palladium nanoparticles, since palladium does not show strong optical properties, morphology analysis was solely conducted. CD measurement of the chiral palladium nanoparticle synthesized showed a very small but broad chiroptic response but was not sufficient enough for quantifiable chirality determination.

## 7.2 Synthesis of Chiral Palladium Nanoparticle

Most of the experimental procedures for of chiral palladium nanoparticle synthesis are similar to that of previous reported 432 helicoid nanoparticle synthesis.<sup>17</sup> Detailed experimental procedures are explained in chapter 3, experimental procedures, with all of the information on chemicals and synthetic conditions listed. During seed-mediated method, as explained multiple times in previous sections, reducing agent and surfactant concentrations collectively affect the nanoparticle morphology and exposed facet. During the conventional chiral gold nanoparticle synthesis, CTAB surfactant and cysteine molecule was used to control the chiral morphology of 432 helicoid nanoparticle. For the reducing agent, L-ascorbic acid (AA), was used to control the growth kinetic of nanoparticle. Similarly, in the chiral palladium nanoparticle synthesis, all reagents have been used

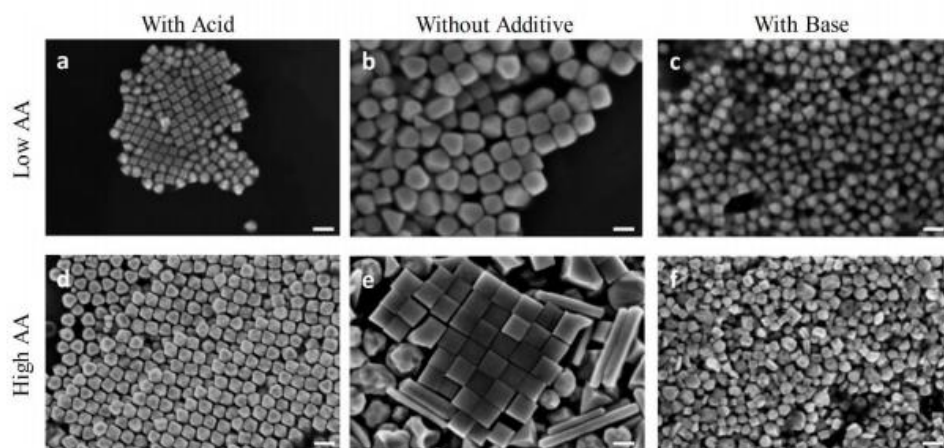


Figure 7. 1 SEM images of palladium nanoparticle synthesized by pH control. pH was adjusted to 1.7 with acid and 4.5 using base, while no additive shows pH around 3.1. Ascorbic acid was controlled as High AA having 12 times higher concentrations than low AA.

similar to that used in the chiral gold nanoparticle synthesis with replacement of  $\text{H}_2\text{PdCl}_4$  metal source instead of  $\text{HAuCl}_4$  and  $\text{H}_2\text{SO}_4$  as acid source for kinetic control. Chiral palladium nanoparticle synthesis was started by introducing  $\approx 45$  nm sized gold cubic seed nanoparticle into the prepared growth solution composed of palladium metal precursor. After 3 hours of the reaction, the final nanostructure was collected and centrifuged for further characterization.

Compared to chiral gold nanoparticle synthesis, experimental condition for chiral palladium nanoparticle synthesis was changed accordingly respect to material selection. During the conventional chiral gold nanoparticle synthesis and other examples of high-index generation during plasmonic nanoparticles, it is required to provide a relatively fast reducing kinetic for promotion of thermodynamically unstable morphology while controlling the uniformity.<sup>17-26</sup> In chiral palladium nanoparticle synthesis, we were able to learn the lesson that at a conventional condition of gold high-index generation, the nanoparticle uniformity was not obtainable. Therefore, in order to further reduce the kinetic of the nanoparticle growth, addition of acid into growth solution was applied which played critical role to stable morphology generation. The reason for this slower kinetic respect to lower pH is related with the proton concentration equilibrium. Proton concentration of the growth solution strongly affect the reducing kinetic during seed-mediated method as it affects the effective kinetic of the reducing agents. In Figure 7.1, variation of reducing agent concentration and solution pH is shown. While only the metal precursor was replaced in the conventional chiral gold nanoparticle synthesis conditions, uneven distribution of cubic, tetrahedron, rod, and undefined morphologies are shown. Simply lower concentration of AA applied to test controllability of this particle irregularity issue, but resulting particle still showed slight deviation in morphology and insufficient nanoparticle growth. However, with addition of acid, particle uniformity was ensured even in the range of high ascorbic acid concentration applied. Also, control experiment was

conducted by adding base into growth solution, which showed only self-nucleated small nanoparticles. These effect of pH controlled nanoparticle morphology are in well agreement with other previous reported data.<sup>27-29</sup>

### 7.3 Structural Analysis of Chiral Palladium Nanoparticle

Following SEM images shown in figure 7.2 is shows truly three-dimensional chiral morphology with distinct spiral features showing on each 6 faces of palladium nanoparticle. The chiral morphology was synthesized by addition of chiral cysteine molecule as the chirality inducer during seed-mediated method. As shown in the figure 7.2 which shows low magnification and also high magnification images of chiral palladium nanoparticles shows clockwise and counterclockwise rotational spiral structures synthesized with l-cysteine and d- cysteine, respectively.

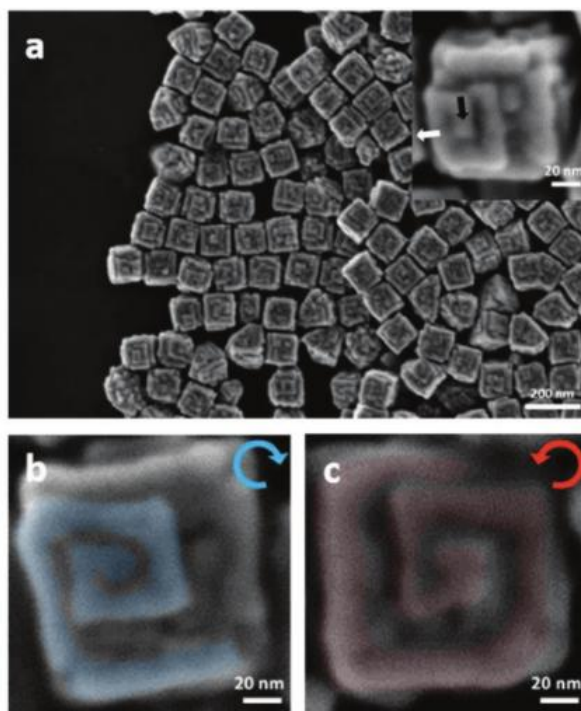


Figure 7. 2 SEM image of chiral palladium nanoparticle controlled by cysteine molecule. As shown, the spiral chiral features show either clockwise or counterclockwise rotation. The direction of rotation has been determined by the input chirality of the molecule introduced during the growth process.

Synthesized nanoparticle shows average edge length of around 100 nm in each edge of cubic based structures. Also, as shown in the magnified image in figure 7.2 a), spiral structures are distinctly evolved which rotates in the inward direction toward the cube plane center, marked with black arrow, while the entire features protruding out from the surface to out which is denoted with white arrow. Interesting part is that the rotational direction of these spiral features in one synthesis batch could take either direction of clockwise or counterclockwise rotation. In the case of chiral gold nanoparticle with strong optical response due to plasmonic property of gold, chirality was measured through circular dichroism (CD). As, chiral palladium intrinsically shows low optical response and due to limited yield of chiral morphologies, statistical analysis of scanning electron microscopy (SEM) images of nanoparticles has been conducted to quantitatively define chirality induced by input chiral molecules.

For the quantitative understanding of chirality evolution, statistical analysis combined with detailed morphology analysis was conducted. This combinational analysis revealed that the spiral structures on chiral palladium nanoparticle have rotational direction preference respect to chirality of the input cysteine molecules. For the accurate and unbiased analysis, we only counted and analyzed visibly definable spiral structures with unidirectional rotation within a single nanoparticle. Recording each rotational direction of the chiral component in a nanoparticle, yield of visibly definable chiral nanoparticles was close to 42.8% and further analysis of 1170 nanoparticles in similar manner yield around 30% of chiral nanoparticles among synthesized nanoparticles. Among chiral nanoparticles with distinguishable spiral structures, *L*-cysteine molecule more preferentially induced clockwise spiral structures in 1.86:1 ratio respect to counterclockwise rotation. On the contrary, *D*-cysteine molecule induced counterclockwise spiral features with 1.76:1 ratio respect to clockwise rotation. It is truly interesting statistically proven chiral bias as our previous chiral gold nanoparticle synthesis

yielded above 80% of chiral nanoparticle from one synthesis batch. Interestingly, chiral palladium nanoparticle synthesis showed lower yield of definable chiral structures with both chirality coexisting in one synthesis batch but with rotational direction difference. At this stage of research, we believe that this difference is due to either relatively weaker interaction between thiol and palladium surface<sup>30,31</sup> or less defined enantio-specific interaction of additional binding site, N-terminal of cysteine, with high-index palladium surfaces.

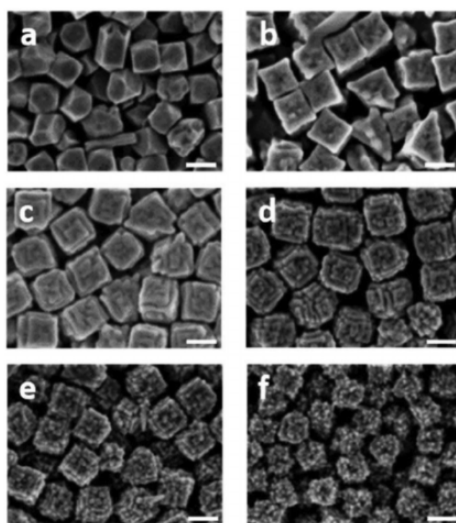


Figure 7. 3 Change in morphology of chiral palladium nanoparticle synthesis respect to change in cysteine concentration in the growth solution. From images of a to f, increasing cysteine concentration was applied with c showing the optimum concentration of 1000 nM.

Direct role of cysteine molecule during chiral palladium nanoparticle synthesis and its effective range for chirality evolution was studied by morphology analysis respect to the input cysteine concentration. Figure 7.3 a to f shows the difference in nanoparticle morphology resulted by changing input cysteine concentration. It is possible to observe a progressive growth of chiral features as

cysteine concentration increases and when it exceeds the effective range, dendritic morphology was observed. Synthesized nanoparticles shown in figure 7.3 b) shows nanoparticle synthesized with input of  $0.5 \times 10^{-6}$  M cysteine concentration. This nanoparticle only shows partial and selective growth at the edges of nanoparticle without any sign of spiral growth. As the input cysteine concentration exceeds beyond  $1 \times 10^{-6}$  M as shown in figure 5.3 d, extensive spiral structure formed progressively grows into dendritic shape with the increase of cysteine concentration. On the other hand, at the cysteine concentration around  $1 \times 10^{-6}$  M which is in the similar range with chiral gold nanoparticle synthesis.<sup>17,19,20</sup> Interestingly, specifically at cysteine concentration of  $1 \times 10^{-6}$  M which is shown in figure 7.3 c), spiral structures were clearly distinguishable. The fact that a specific cysteine concentration exists for spiral morphology generation is in accordance with our previous result which has a very close relationship with the co-existing surfactant concentration.

In the middle of nanoparticle growth, the surface of the nanoparticle contains two components interacting with the surface; cysteine and CTAB. CTAB molecule, used as a surfactant and a capping agent during this synthesis method is known to stabilize {100} facet during palladium nanoparticle synthesis. Furthermore, undisturbed growth of this condition and further growing the nanoparticle is known to form cuboctahedron and eventually {111} facet bound octahedron. Under the situation when cysteine molecule is introduced into the growth solution, the nanoparticle surface will have a preference of the optimum range of surfactant concentration which cysteine could show its maximum ability to influence the nanoparticle growth and chirality inducing. Figure 7.4 shows a specific relationship between surfactant concentration and cysteine concentration during chiral palladium nanoparticle synthesis. When the  $50 \times 10^{-3}$  M CTAB concentration was applied, regardless of cysteine concentration, octahedron shaped nanoparticles are observed. This indicates that as the CTAB concentration is dominant, cysteine fails

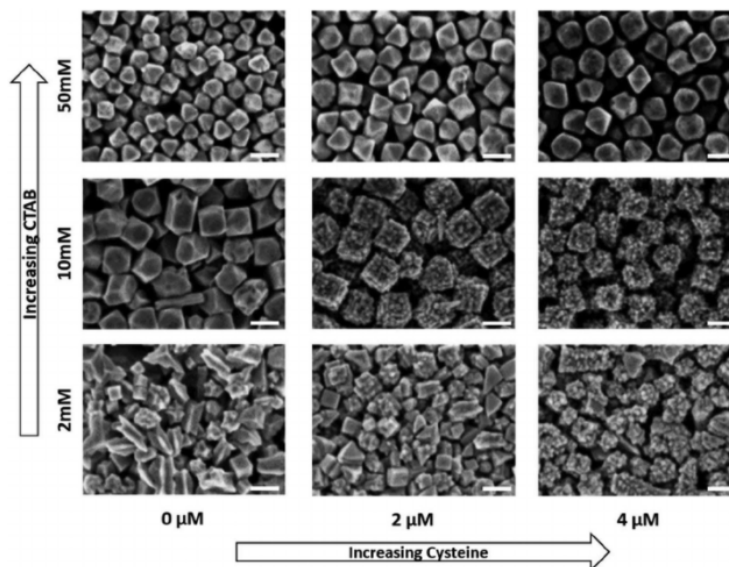


Figure 7. 4 Morphology diagram of CTAB vs cysteine concentration. The concentration range mentioned on each axis refers to the final concentration of each reagent. Besides surfactant concentration and the cysteine concentration, all other synthetic conditions have been kept constant.

to show its influence of morphology directing. In the range of  $2 \times 10^{-3}$  M CTAB concentration, cysteine induced morphology directing shows an effective influence on the overall morphology but due to lack of the surfactant and capping agent, large aggregates and irregular nanostructures are formed. At the specific concentration of  $10 \times 10^{-3}$  M CTAB in chiral palladium growth solution, cysteine most effectively shows its ability to uniformly control nanocrystal structures which shows the importance of competitive relationship between chirality inducing agent and surfactant. This  $10 \times 10^{-3}$  M concentration of CTAB is in the range which is very similar with that of chiral gold nanoparticle synthesis which is  $15 \times 10^{-3}$  M. We could conclude from this that chiral nanoparticle synthesis using amino acid and peptide functions in a very similar range of surface chemistry in the case of palladium and gold.

## 7.4 Temporal Evolution of Chiral Palladium Nanoparticle

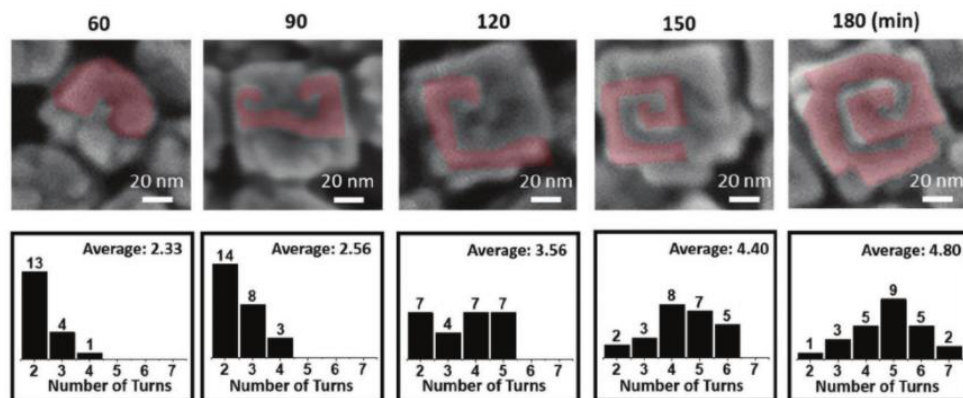


Figure 7. 5 Time variant morphology analysis of chiral palladium synthesis. For the statistical analysis, multiple nanoparticles have been analyzed and the average number of turns have been calculated to show progressive growth of chiral features.

Understanding how the features grow and quantitatively observing them is an important part in the study of chirality development mechanism. As the reaction proceeds, chiral nanoparticles increase in size and progressively show distinguishable chiral features. In order to further study, the morphology evolution during chiral palladium nanoparticle synthesis was further conducted. Figure 7.5 shows the time-dependent morphology evolution of chiral palladium nanoparticles, which shows the average number of turns each spiral feature shows. SEM images in Figure 7.5 clearly show that chiral spiral nanostructures progressively grow into longer and more definable spiral structures as reaction time proceeds from 60 to 180 min. Instead of simply observing the morphology, we have more quantitatively analyzed spiral structures as we manually counted the number of turns each chiral feature takes on chiral palladium nanoparticles as reaction time increases. The most distinguishable and representative spiral structure was selected from each nanoparticle for the statistical analysis. During the early stage of chiral palladium

nanoparticle synthesis, only limited number of definable spiral structures existed and those nanoparticles with distinguishable structures had average turn of 2.33 times. Between the synthesis time of 90 and 150 min, the number of turns on spiral features most significantly increase from 2.56 times to 4.40 times. This let us know that most vigorous chiral growth of spiral structures are occurring in this stage of nanoparticle growth. As reaction time proceeds, average number of turn increases up to 4.8 turns at 180 min. This clearly shows that chiral features continue to grow in a single direction as the reaction proceeds.

## 7.5 Conclusion

In conclusion, we have successfully demonstrated the synthesis of chiral palladium nanoparticles using aqueous based seed-mediated method. The chiral morphology of here synthesized palladium nanoparticle can be directly modulated by controlling the cysteine molecule concentration. Synthesized nanoparticle shows the spiral structure as its unique chiral features with rotational direction preference which is determined by the input cysteine molecular chirality. For uniform control of nanoparticle morphology, acid was introduced during the synthesis to control reduction kinetic. Effective chirality evolution during the chiral palladium nanoparticle synthesis occurs under a specific relationship between cysteine concentration and surfactant CTAB concentration. This competitive relationship is in a well agreement with our lessons found from chiral gold nanoparticle synthesis. By again establishing that this relationship exists for other metal nanoparticle synthesis using amino acid or peptide as chirality inducer, it could provide a strong foundation for applying this generalized two step seed-mediated method using chiral biomolecules into synthesis of other face-centered cubic metal or metal oxide nanoparticles. For more detailed observation of chirality development, the progressive evolution of spiral morphology was studied through time variant synthesis. From this time-variant study, average number of turns that each spiral structure show was quantitatively analyzed and it shows increase as reaction time increase. As far as our understanding goes, it is the first experimental demonstration of three-dimensional chirality generation, controlled by organic additive, in palladium nanoparticle synthesis. Based on this understanding, this chiral palladium nanoparticle synthesis can potentially be developed into chiral catalyst synthesis for asymmetric synthesis or enantioselective sensing applications.

## 7.6 Bibliography

- (1) Yasukawa, T.; Suzuki, A.; Miyamura, H.; Nishino, K.; Kobayashi, S. Chiral Metal Nanoparticle Systems as Heterogeneous Catalysts beyond Homogeneous Metal Complex Catalysts for Asymmetric Addition of Arylboronic Acids to  $\alpha,\beta$ -Unsaturated Carbonyl Compounds. *J. Am. Chem. Soc.* **2015**, *137* (20), 6616–6623. <https://doi.org/10.1021/jacs.5b02213>.
- (2) Blaser, H.-U. Enantioselective Synthesis Using Chiral Heterogeneous Catalysts. *Tetrahedron: Asymmetry* **1991**, *2* (9), 843–866. [https://doi.org/10.1016/S0957-4166\(00\)82195-3](https://doi.org/10.1016/S0957-4166(00)82195-3).
- (3) Yasukawa, T.; Masuda, R.; Kobayashi, S. Development of Heterogeneous Catalyst Systems for the Continuous Synthesis of Chiral Amines via Asymmetric Hydrogenation. *Nat. Catal.* **2019**, *2* (12), 1088–1092. <https://doi.org/10.1038/s41929-019-0371-y>.
- (4) Jin Bae, S.; Moon Kim, B.; Kim, S.-W.; Hyeon, T. New Chiral Heterogeneous Catalysts Based on Mesoporous Silica: Asymmetric Diethylzinc Addition to Benzaldehyde. *Chem. Commun.* **2000**, No. 1, 31–32. <https://doi.org/10.1039/a908967e>.
- (5) Sun, H.; Zhang, H.; Ang, E. L.; Zhao, H. Biocatalysis for the Synthesis of Pharmaceuticals and Pharmaceutical Intermediates. *Bioorg. Med. Chem.* **2018**, *26* (7), 1275–1284. <https://doi.org/10.1016/j.bmc.2017.06.043>.
- (6) Nguyen, L. A.; He, H.; Pham-Huy, C. Chiral Drugs: An Overview. *Int. J. Biomed. Sci.* **2006**, *2* (2), 85–100.
- (7) Yasukawa, T.; Miyamura, H.; Kobayashi, S. Chiral Metal Nanoparticle-Catalyzed

Asymmetric C–C Bond Formation Reactions. *Chem. Soc. Rev.* **2014**, *43* (5), 1450–1461. <https://doi.org/10.1039/C3CS60298B>.

- (8) Tamura, M.; Fujihara, H. Chiral Bisphosphine BINAP-Stabilized Gold and Palladium Nanoparticles with Small Size and Their Palladium Nanoparticle-Catalyzed Asymmetric Reaction. *J. Am. Chem. Soc.* **2003**, *125* (51), 15742–15743. <https://doi.org/10.1021/ja0369055>.
- (9) Phan, T. T. V.; Huynh, T.-C.; Manivasagan, P.; Mondal, S.; Oh, J. An Up-To-Date Review on Biomedical Applications of Palladium Nanoparticles. *Nanomaterials* **2019**, *10* (1), 66. <https://doi.org/10.3390/nano10010066>.
- (10) Beletskaya, I. P.; Cheprakov, A. V. The Heck Reaction as a Sharpening Stone of Palladium Catalysis. *Chem. Rev.* **2000**, *100* (8), 3009–3066. <https://doi.org/10.1021/cr9903048>.
- (11) Muñiz, K. High-Oxidation-State Palladium Catalysis: New Reactivity for Organic Synthesis. *Angew. Chemie Int. Ed.* **2009**, *48* (50), 9412–9423. <https://doi.org/10.1002/anie.200903671>.
- (12) Shao, Z.; Zhu, W.; Wang, H.; Yang, Q.; Yang, S.; Liu, X.; Wang, G. Controllable Synthesis of Concave Nanocubes, Right Bipyramids, and 5-Fold Twinned Nanorods of Palladium and Their Enhanced Electrocatalytic Performance. *J. Phys. Chem. C* **2013**, *117* (27), 14289–14294. <https://doi.org/10.1021/jp402519u>.
- (13) Yang, C.-W.; Chanda, K.; Lin, P.-H.; Wang, Y.-N.; Liao, C.-W.; Huang, M. H. Fabrication of Au–Pd Core–Shell Heterostructures with Systematic Shape Evolution Using Octahedral Nanocrystal Cores and Their Catalytic Activity. *J. Am. Chem. Soc.* **2011**, *133* (49), 19993–20000. <https://doi.org/10.1021/ja209121x>.
- (14) Niu, W.; Li, Z. Y.; Shi, L.; Liu, X.; Li, H.; Han, S.; Chen, J.; Xu, G. Seed-

Mediated Growth of Nearly Monodisperse Palladium Nanocubes with Controllable Sizes. *Cryst. Growth Des.* **2008**, *8* (12), 4440–4444. <https://doi.org/10.1021/cg8002433>.

- (15) Xie, X.; Gao, G.; Pan, Z.; Wang, T.; Meng, X.; Cai, L. Large-Scale Synthesis of Palladium Concave Nanocubes with High-Index Facets for Sustainable Enhanced Catalytic Performance. *Sci. Rep.* **2015**, *5* (1), 8515. <https://doi.org/10.1038/srep08515>.
- (16) DeSantis, C. J.; Sue, A. C.; Bower, M. M.; Skrabalak, S. E. Seed-Mediated Co-Reduction: A Versatile Route to Architecturally Controlled Bimetallic Nanostructures. *ACS Nano* **2012**, *6* (3), 2617–2628. <https://doi.org/10.1021/nn2051168>.
- (17) Lee, H.-E.; Ahn, H.-Y.; Mun, J.; Lee, Y. Y.; Kim, M.; Cho, N. H.; Chang, K.; Kim, W. S.; Rho, J.; Nam, K. T. Amino-Acid- and Peptide-Directed Synthesis of Chiral Plasmonic Gold Nanoparticles. *Nature* **2018**, *556* (7701), 360–365. <https://doi.org/10.1038/s41586-018-0034-1>.
- (18) Kim, H.; Im, S. W.; Cho, N. H.; Seo, D. H.; Kim, R. M.; Lim, Y.; Lee, H.; Ahn, H.; Nam, K. T.  $\Gamma$ -Glutamylcysteine- and Cysteinylglycine-Directed Growth of Chiral Gold Nanoparticles and Their Crystallographic Analysis. *Angew. Chemie Int. Ed.* **2020**, *59* (31), 12976–12983. <https://doi.org/10.1002/anie.202003760>.
- (19) Lee, H.-E.; Kim, R. M.; Ahn, H.-Y.; Lee, Y. Y.; Byun, G. H.; Im, S. W.; Mun, J.; Rho, J.; Nam, K. T. Cysteine-Encoded Chirality Evolution in Plasmonic Rhombic Dodecahedral Gold Nanoparticles. *Nat. Commun.* **2020**, *11* (1), 263. <https://doi.org/10.1038/s41467-019-14117-x>.
- (20) Cho, N. H.; Byun, G. H.; Lim, Y.-C.; Im, S. W.; Kim, H.; Lee, H.-E.; Ahn, H.-Y.;

Nam, K. T. Uniform Chiral Gap Synthesis for High Dissymmetry Factor in Single Plasmonic Gold Nanoparticle. *ACS Nano* **2020**, *14* (3), 3595–3602.  
<https://doi.org/10.1021/acsnano.9b10094>.

- (21) Xia, Y.; Gilroy, K. D.; Peng, H. C.; Xia, X. Seed-Mediated Growth of Colloidal Metal Nanocrystals. *Angew. Chemie - Int. Ed.* **2017**, *56* (1), 60–95.  
<https://doi.org/10.1002/anie.201604731>.
- (22) Lee, H. E.; Yang, K. D.; Yoon, S. M.; Ahn, H. Y.; Lee, Y. Y.; Chang, H.; Jeong, D. H.; Lee, Y. S.; Kim, M. Y.; Nam, K. T. Concave Rhombic Dodecahedral Au Nanocatalyst with Multiple High-Index Facets for CO<sub>2</sub> Reduction. *ACS Nano* **2015**, *9* (8), 8384–8393. <https://doi.org/10.1021/acsnano.5b03065>.
- (23) Personick, M. L.; Mirkin, C. A. Making Sense of the Mayhem behind Shape Control in the Synthesis of Gold Nanoparticles. *J. Am. Chem. Soc.* **2013**, *135* (49), 18238–18247. <https://doi.org/10.1021/ja408645b>.
- (24) Park, J. E.; Lee, Y.; Nam, J. M. Precisely Shaped, Uniformly Formed Gold Nanocubes with Ultrahigh Reproducibility in Single-Particle Scattering and Surface-Enhanced Raman Scattering. *Nano Lett.* **2018**, *18* (10), 6475–6482.  
<https://doi.org/10.1021/acs.nanolett.8b02973>.
- (25) Johnson, C. J.; Dujardin, E.; Davis, S. A.; Murphy, C. J.; Mann, S. Growth and Form of Gold Nanorods Prepared by Seed-Mediated, Surfactant-Directed Synthesis. *J. Mater. Chem.* **2002**, *12* (6), 1765–1770.  
<https://doi.org/10.1039/b200953f>.
- (26) Jana, N. R.; Gearheart, L.; Murphy, C. J. Seed-Mediated Growth Approach for Shape-Controlled Synthesis of Spheroidal and Rod-like Gold Nanoparticles Using a Surfactant Template. *Adv. Mater.* **2002**, *13* (18), 1389–1393.

[https://doi.org/10.1002/1521-4095\(200109\)13:18<1389::aid-adma1389>3.0.co;2-f](https://doi.org/10.1002/1521-4095(200109)13:18<1389::aid-adma1389>3.0.co;2-f).

- (27) Tyagi, H.; Kushwaha, A.; Kumar, A.; Aslam, M. A Facile PH Controlled Citrate-Based Reduction Method for Gold Nanoparticle Synthesis at Room Temperature. *Nanoscale Res. Lett.* **2016**, *11* (1), 362. <https://doi.org/10.1186/s11671-016-1576-5>.
- (28) Patungwasa, W.; Hodak, J. H. PH Tunable Morphology of the Gold Nanoparticles Produced by Citrate Reduction. *Mater. Chem. Phys.* **2008**, *108* (1), 45–54. <https://doi.org/10.1016/j.matchemphys.2007.09.001>.
- (29) Thambi, V.; Kar, A.; Ghosh, P.; Paital, D.; Gautam, A. R. S.; Khatua, S. Synthesis of Complex Nanoparticle Geometries via PH-Controlled Overgrowth of Gold Nanorods. *ACS Omega* **2019**, *4* (9), 13733–13739. <https://doi.org/10.1021/acsomega.9b01119>.
- (30) Majumder, C. Adsorption of Thiols on the Pd(111) Surface: A First Principles Study. *Langmuir* **2008**, *24* (19), 10838–10842. <https://doi.org/10.1021/la801439q>.
- (31) Gan, L.-Y.; Zhang, Y.-X.; Zhao, Y.-J. Comparison of S Poisoning Effects on CO Adsorption on Pd, Au, and Bimetallic PdAu (111) Surfaces. *J. Phys. Chem. C* **2010**, *114* (2), 996–1003. <https://doi.org/10.1021/jp905957f>.

## Chapter 8. Concluding Remarks

Nano-sized chirality control holds much engineering and scientific value especially when realized in inorganic materials. Chirality, purely geometric property found in nature in many cases, refer to the mirror images of a molecular or geometrical structure being non-superimposable to each other. With this geometric property, many fascinating phenomenon or biological behaviors were possible. Utilizing this prevalent biological property and applying this to inorganic materials such as metals in nanoscale could generate a fascinating physical, chemical, and biological phenomena which was originally limited to nanomaterials with symmetric structures. There are numerous methods to generate chiral nanomaterials such as top-down and bottom-up methods. Among many methods, aqueous based chemical seed-mediated synthesis method contains significant advantages. First advantage is that it is relatively easier to scale-up the synthesis process for large-scale production in a relatively environmental-friendly method. Secondly, it is possible to control the nanoscale chiral features while forming a truly three-dimensional structure which other methods have difficulty with. Thirdly, the introduced method has been proven to show a very strong chiroptic response at visible wavelength due to subwavelength control of chiral morphology. Therefore, in order to meet the needs of widely increasing versatile potential applications of chiral nanomaterials, ground stone study and fundamental understanding of the seed-mediated based chiral nanomaterial synthesis need to be conducted. Furthermore, based on this study, establishment of design principle for expansion of synthesis method is necessary for generation of chiral nanostructure for various specific applications. The devised aqueous chemical seed-mediated chiral nanoparticle synthesis holds its uniqueness with utilization of the enantioselective interaction between chiral molecule and chiral metal surface. From this study, we specifically focus to study the underlying mechanism and influential factors of chirality evolution for establishment of systematic

enhancement of chiroptic response. Furthermore, based on the understanding of chirality evolution, we intend to apply the synthetic principle for successful expansion of chirality inducing agent and material selection for more wide application.

In the context of utilizing chiral plasmonic nanomaterials in optical applications, enhancement of absolute intensity of chiroptical response is very important. For the increase of chiroptic response, synthesized 432 helicoid nanoparticle was quantitatively analyzed in order to understand and assess the full potential of current synthesis method. Therefore, assessment of synthetic quality and optical response of a single nanoparticle itself has been measured through single nanoparticle level dark-field scattering analysis. Current chiroptic response of 432 helicoid III, which is often compared by the dissymmetric factor, g-factor, shows around 0.2 which is among one of the highest reported value. Current chiroptic response of 432 helicoid is observed by the solution ensemble stage, which is should contain average information of morphology, size, and CPL irradiation angle variation. Therefore, this average optical response does not entirely show the true potential of 432 helicoid nanoparticles. Single nanoparticle scattering data was compared to CD based measurement of same nanoparticle solution. From the comparison, we were able to conclude that single nanoparticle level 432 helicoid g-factor shows up to 0.8 which far exceeds the averaged solution based measured values of 0.2. Furthermore, we learned that the overall g-factor is diminished by averaging of well-defined chiral nanoparticles and deformed nanoparticles. Therefore, we were able to make a conclusion that in order to further enhance chiroptic response of 432 helicoid, we need to ensure the synthetic uniformity, especially the uniformity of chiral gap structures.

For the systematic control of the chirality development and ensure the homogeneity of the synthesized nanoparticles, it is critical to understand the effect

of each kinetic parameters on chirality evolution and the detailed growth mechanism of 432 helicoid nanoparticles. Kinetic parameters study allows us to understand the effect of individual reagents involved in chiral nanoparticle synthesis and how they influence the evolution of chirality. Time-variant study of chirality evolution mechanism shows how optical and morphological chirality evolve and how they are inter-related. In terms of growth mechanism, we were able to learn that there are two regimes of chiral growth: the lateral growth regime and the vertical growth regime. For each growth regime, the synthetic conditions required are clearly different, since each growth step promotes a different type of chirality evolution. Therefore, instead of only allowing initial control of the chiral growth environment, we systematically segmented two growth steps and applied different synthetic conditions for uniform chiral gap evolution. Here devised multi-chirality evolution step enhances the chiropractic response of the 432 helicoid III by achieving higher homogeneity of the synthesized nanoparticles. The origin of the enhanced chiropractic response is attributed to the increased chiral gap homogeneity which has been experimentally and quantitatively supported by morphological and optical analysis.

In order to apply chiral nanomaterials in more general applications, other than optical applications, providing flexibility of its optical response and intrinsic property is necessary. Especially, versatility of possible chiral nanostructures and expansion of synthesis method to alternative material is crucial. In this regard, based on the fundamental understanding of amino acid and peptide based aqueous seed mediated method, controlled expansion of this method has been established. Expansion of synthesis method has been demonstrated in two large directions. First direction is extension of chiral inducing biomolecules from amino-acid or short peptides to longer sequence programmable oligomer such as ssDNA. Second direction is to use an alternative material such as palladium for catalytic or sensing applications.

Firstly, in the context of sequence programmable oligomer, it is difficult to pass by DNA molecules. As well known to researchers, DNA nucleobase sequence could easily and economically be programmed as desired. Also, each nucleobase has a very distinct surface interaction with not only gold but with metals. In order to observe potential chirality evolution ability of ssDNA oligomer, thymine oligomer has been added to 432 helicoid II synthesis which conventionally use glutathione molecule as chirality inducer. Interestingly, when thymine oligomer was introduced to assist 432 helicoid II synthesis, chiroptic response was doubled while only thymine was introduced to the growth solution, there has been no chirality evolution observed. With this result, we were able to conclude that ssDNA could affect the nanoparticle growth. Therefore, chirality evolution was tested for other ssDNA oligomer nucleobases which this time, only the DNA was used for the nanoparticle synthesis. Interestingly, adenine oligomer specifically showed chirality evolution capability while other nucleobases did not show any chiral development. In the effort to understand this adenine specific chirality evolution, DFT calculation was conducted to understand the enantiospecific binding affinity of nucleobase and gold surface. Adenine oligomer shows increasing enantiospecificity by forming hydrogen bonding with each other according to our simulation while other bases did not show this specific behavior. For further modulation, DNA sequence control was conducted which shows modulation of chirality evolution by changing sequence length and pattern. Based on this results, we were able construct a general rule of thumb for using ssDNA as chirality inducer.

For non-optical applications of chiral nanomaterials such as catalysis or sensing, it was important to test the viability of this synthesis method using different noble metals. The material was selected based on the ease of direct application into currently established synthetic system and palladium has been chosen. Synthesized chiral palladium nanoparticles show a unique spiral structures

protruding outward from the nanoparticle plane. The rotation of spiral structures shows directional preference respect to the chirality of input cysteine molecule. Depending on the input chirality of the chiral molecule, cysteine, chiral palladium nanoparticle showed increase in ratio of clockwise or counter-clockwise spiral structure.

From this research, I believe it was possible to understand the individual and also correlated effect of synthesis parameter during aqueous based seed mediated method for chiral nanoparticle synthesis. Furthermore, based on this understanding, demonstration of systematic control of chirality evolution and establishment of effective expansion of devised method for more versatile application was possible.

## 초 록

나노 구조체의 제작 및 이의 구조 변화는, 물질 자체의 특성을 새롭게 변화시킬 수 있다는 가능성에 과학 및 공학 분야에서 큰 관심을 받아왔다. 특히, 자연계에 존재하는 카이랄성을 나노 구조체에서 구현함으로써, 생체 분자가 가지고 있는 고유의 물리적, 화학적 특성을 무기물에서 구현 및 응용 가능하다는 것이 이미 다년간의 연구를 통해 알려졌다. 특히 빛-물질 간 강한 상호작용을 나타내는 플라즈모닉 재료 군을 기반으로 나노 광학 분야는 크게 발전하였으며, 다양한 구조체와 카이랄 광 반응을 보이는 구조체 제작방법이 보고된 바 있다. 대표적인 예로, 정밀한 리소그래피 기술 또는 분자 자가 조립을 기반으로 한 스캐폴드 기술이 사용이 되었지만, 이러한 기술들은 공정에 있어서 높은 복잡도를 요구하며, 낮은 해상도 및 구조의 안정성 결여라는 한계를 가지고 있다. 따라서, 이러한 한계를 극복하기 위한 새로운 제작/합성 기술의 개발이 중요하다. 본 연구단은 수계에서 씨앗-매개 합성법 기반 카이랄 아미노산 혹은 펩타이드를 사용하는 카이랄 나노 구조체 제작 방법을 보고한 바 있다. 이는, 카이랄 유기물과 고밀러지수의 무기물 표면 간의 카이랄 상호작용을 기반으로, 카이랄 유기 분자의 카이랄성이 무기물에 전달되는 방식이다. 이러한 합성법은 수 나노단위에서 카이랄 구조체 조절이 가능하며, 이를 통해 다양한 구조와 광 특성 변화 및 카이랄성을 정량적으로 평가하는 dissymmetric factor가 0.2라는 높은 카이랄 광 반응성을 달성 할 수 있었다. 나노 구조체가 가지는 특수한 4-fold, 3-fold, 2-fold symmetry에 기인하여 나노구조체는 432 helicoid 라 명명되었다.

제 4장에서는 432 helicoid 나노 입자의 광 특성 합성 적 개선 가능성을 확인하였다. 이미 훌륭한 광 특성을 지닌 432 helicoid 나노입자이지만, 실질적인 카이랄 나노구조체의 산업적 적용에 있어서, 나노구조체의 합성법에 대한 정량적인 평가 및 합성 적 개량을 통한 광 특성 증대는 필수적이라 할 수 있다. 이러한 관점에서, 기존 용액에 분산된 나노 입자의 평균적인 광 특성을

측정하는 Circular Dichroism(CD) 기법이 아닌, 단일 나노 입자 수준에서의 산란 기반의 암시야 분광 법은, 나노 입자의 구조와 광 특성을 집적 적으로 연관시켜 이해를 도우며, 합성된 나노 입자의 상태를 정량적으로 알 수 있다. 이러한 암시야 분광 법을 통해서 432 helicoid 나노 입자를 관찰 할 경우, 기존 관찰되었던 나노 입자의 0.2 라는 dissymmetric factor는 개별적인 나노입자들의 광 특성의 종합적인 평균으로 이루어져 있다는 사실을 알 수 있었다. 이에 따라, 단일 나노 입자의 구조와 해당하는 광 특성을 대조하여 본 결과, 카이랄 갭의 구조가 균일하게 발달 된 경우 dissymmetric factor 가 0.8 까지 측정된 반면, 카이랄 갭의 구조가 아주 미세하게 변함에 따라서 전체적인 dissymmetric factor 가 크게 감소하고, 파장 또한 다르게 측정되었다. 이는, 합성적 관점에서 2가지의 사실을 말해준다. 첫째, 단일 나노 입자가 가지는 가능한 카이랄 광 특성은 훨씬 높으며, 합성 적 개량을 통해 더욱 높은 광특성 달성이 가능하다. 두번째로, 이러한 합성 적 개량을 함에 있어서, 카이랄 갭의 균일도를 조절하는 것이 중요하다는 사실이다.

제 5 장에서는, 이전의 연구 결과에 기인하여, 본 연구를 통해서 432 helicoid 의 합성 조건에 따른 카이랄성 발현과 카이랄성이 발현되는 과정에 대한 정확한 이해를 기반으로, 다단계의 카이랄 성장 과정을 가지는 나노 입자 합성법을 제시하였다. 이는, 균일한 카이랄 갭 구조를 발달시키는 방향으로 초점을 맞추었다. 씨앗-매개 합성에 있어서 열역학적 성장을 유도하는 계면활성제 혹은 유기 첨가물의 조절과 Kinetic 성장을 유도하는 환원제와 금속이온 조절은, 나노 입자의 구조를 제어하는데 필수적인 요소이다. 이러한 조절을 통해 카이랄성 발현이 되는 과정 및 환경을 상세히 이해하였다. 또한, 시간에 따라 432 helicoid 가 성장하는 과정을 광 특성 관점과 구조적 관점에서 보면, 1차적으로 카이랄한 기초 구조와 고 밀리지수 표면이 생성되는 Lateral 성장과 2차적으로 생성된 카이랄 기초 구조에 기반하여 정육면체 형태의 외골격이 형성되며 카이랄 갭이 완성되는 Vertical 성장 과정으로 나눌 수 있다. 이렇게 나누어진 2단계의 성장 단계에서, 합성 조건의 조절을 통해서 카이랄 성장 경로를 제어하였으며, 이는 균일한 카이랄 갭의 구조 발달로 나노 입자 성장을

유도하였다. 합성된 나노 입자는 기존 dissymmetric factor 인 0.2 에서 50% 이상 증가한 0.31을 보였으며, 이러한 광 특성 증대가 나노입자 균일도 증대에서 기인한다는 것을 광 스펙트럼의 Full-Width-Half-Maximum 과 나노입자의 구조적 균일도를 통계적으로 관찰함을 통해 증명하였다.

제 6장에서는 기존 연구들이 씨앗-매개 기반 카이랄 나노 입자 합성에 있어서, 아미노산과 펩타이드를 이용한 유기물의 카이랄성을 무기물로 전이하였다면, 본 연구를 통해서 합성된 나노 입자의 정량적 분석과 합성 적 개량을 통해 광 특성 증대를 달성하였다. 하지만, 더욱 다양한 카이랄 나노 구조의 적용 처에 따른 맞춤형 나노 구조 제작을 위해서는 기존의 틀에서 벗어나는 노력들이 필수적이다. 이러한 관점에서, 2가지의 큰 방법으로 본 연구단의 나노 입자 합성 기술의 확장을 모색하였다. 우선, 기존 작은 크기의 아미노산 혹은 펩타이드 에서 시도되었던 카이랄 나노 구조체의 제작을 더 크고 프로그래밍 가능한 DNA 로 확장하였다. 또한, 광학적 적용 처 이외의 촉매 혹은 센싱 적용처로의 효율적인 확장을 위해 팔라듐 이라는 다른 소재군으로의 확장을 구현하였다.

서열의 조절이 용이하다는 관점에서 DNA 는 굉장히 유용한 유기 분자라 할 수 있다. 이미 DNA는 수만년동안의 생명체 진화에서 세대간의 중요한 유전적 정보를 세세하게 프로그래밍 하여 전달한다는 매개체 역할을 해왔다. 또한 이러한 단일 가닥 DNA들의 염기서열의 경우, 금속 표면과 서로 다른 흡착 특성을 나타냄이 알려져 있다. 이데 따라, 단일 염기서열 DNA를 3차원 카이랄 나노 구조체의 합성에 적용하여 카이랄성 발현에 미치는 영향을 알아보았다. 432 helicoid II 의 합성 과정에서 정육면체 씨앗과 glutathione 분자를 사용하는 합성 과정에 Thymine 유기분자를 첨가하면, dissymmetric factor 가 2배 가까이 증가하는 것을 관찰하였다. 또한, 단일 가닥 DNA 자체만으로 카이랄성 발현이 가능함을 확인하였으며, 아데닌 분자를 사용한 나노 입자 에서 유일하게 카이랄성이 발현됨을 발견하였다. 합성된 나노 입자는 대략 200 nm 정도의 변의 길이를 가지며, 4개의 분명한 카이랄 구조체가 형성되며, 생성

된 구조체는 반시계방향으로 돌아간다는 사실을 알 수 있었다. 아데닌 에서 유일하게 카이랄성이 발현되는 이유를 찾자, DFT를 통해 고 밀리지수 표면에서의 각 염기서열의 카이랄 결합 안정성을 계산하였다. 결과적으로, 아데닌이 금(321)표면에 증착 됨에 따라서 Enantiospecificity 가 증가하며, 열역학적으로 표면에 붙는 아데닌이 서로 수소결합을 이루는 형식으로 배열된다. 이러한 현상은 다른 염기서열에서는 관찰되지 않았다. 프로그래밍 가능한 나노 구조체의 제작 관점에서 아데닌의 서열을 조절해 보았을 때, 아데닌 길이가 늘어남에 따라서 광 특성이 증대됨을 발견하였고, 또한 아데닌과 씨토신의 배열을 조절함에 따라서 다양한 광 특성이 발현 됨을 발견하였다. 추가적으로, 표면에서 작용하는 CTAB 계면활성제와의 경쟁 관계를 관찰함으로써, 카이랄성 발현에 있어 두 인자가 중요하게 작용한 다는 사실을 알 수 있었다. 본 연구에서는, 이러한 실험적 결과들을 기반으로 프로그래밍 가능한 카이랄 나노구조체의 제작의 합성 적 기초를 다질 수 있었다.

제 7장에서는, 광학적 적용이 아닌 촉매 적 혹은 센싱 적 적용을 위해 재료적 확장을 확인하였다. 팔라듐은 현 씨앗-매개 기반 합성법에 적용 용이하며, 뛰어난 촉매 적 특성을 나타내는 것으로 알려져 있다. 이에 따라 정육면체 씨앗 과 Cysteine 분자를 사용하여 카이랄 성을 나타내는 팔라듐 나노 입자를 제작하였다. 팔라듐 자체의 광학적 반응 성이 높지 않은 관계로 SEM 기반 구조분석으로 진행되었다. 합성된 나노 입자는 100nm 정도의 크기를 가지며, 시계방향 혹은 반시계방향으로 꼬이는 Spiral 구조체를 나타내며, 이는 표면에서 멀어지는 방향으로 돌출되게 생성된다. 이러한 구조체의 꼬이는 방향성은 넣어주는 cysteine 분자의 카이랄성에 따라 생성되는 방향성의 비율이 달라지며, 이는 다수의 나노 입자를 분석하여 통계적 처리를 통해 확인되었다. 이를 시간에 따른 성장을 관찰 하였으며, 표면 경쟁하는 CTAB 과 Cysteine 의 관계 또한 확인하였다. 이러한 카이랄 팔라듐 나노 입자 개발은 추후 카이랄 나노구조체의 적용 처를 확장시키는 중요한 기반이 되는 연구라고 생각된다.

본 연구에서 개발된 새로운 방법론들과 더욱 다양한 카이랄 구조체들은, 산업적 적용에 필요한 맞춤형 특성을 합성 적으로 구현하는 기반 기술로 사용될 것이라 생각하며, 카이랄 나노구조체의 적용 가능성을 더욱 확대 해 줄 수 있을 것이라 생각한다.

주요어: 씨앗-매개 합성, 메탈 나노 구조 제어, 유기 분자, 카이랄 나노입자

학번: 2017-36204

## 감사의 글

박사과정을 시작한지 얼마 된 것 같지 않지만, 벌써 4년이라는 시간이 흘렀습니다. 많이 부족했고, 도움이 필요했던 저에게 늘 가르침을 주시고 도움을 주셨던 분들 덕분에, 연구자로서뿐만 아니라 한 사람으로써 발전하고, 성장할 수 있었습니다. 좋은 경험과 성장의 시간을 함께 해주신 많은 분들께 감사의 말씀을 드립니다.

우선 남기태 교수님께 감사인사 드리고 싶습니다. 연구자로서 경험이 부족했던 저에게 과학자로서 성장할 수 있도록 지도해주시고 조언 해주셔서 감사합니다. 교수님 덕분에, 부족하지 않은 지원 아래에서, 하고 싶은 연구를 모두 할 수 있었던 거 같습니다. 언제나 연구에 대한 열정 넘치는 지도로, 제가 연구 적으로 힘들어 할 때, 길을 잡아주시고 다독여 주셔서 감사합니다. 교수님께서 지도해주신 연구 방법, 늘 생각하는 자세, 발표하는 방법 등등 제가 연구자로서 성장할 수 있는 가르침들 되새기며 앞으로 더욱 발전하도록 하겠습니다.

또한 바쁘신 와중에도 귀하신 시간을 내어 저의 학위 심사를 허락해 주시고, 학위 과정과 앞으로 연구자로서 가져야할 조언들 해주신 도준상 교수님, 권민상 교수님, 서지원 교수님 그리고 한정우 교수님 감사합니다. 생물학적 관점에서의 깊은 통찰력과 아이디어를 주시고 늘 격려해 주시며, 따뜻한 말들 해주신 도준상 교수님 감사합니다. 앞으로의 연구 동안 교수님이 해주셨던 조언들 되새기며 더욱 발전하도록 하겠습니다. 제 박사학위 연구에서 생각지 못했던 관점과 새로운 접근의 아이디어 주신 권민상 교수님 감사합니다. 교수님처럼 다양한 관점에서 연구에 대해 열린 생각을 가진 사람이 되도록 노력하겠습니다. 제가 많이 부족한 박

사과정 2학년일때부터 공동연구미팅에서 늘 화학 실험에서 필요한 부분에 대한 세심한 조언과 방대한 화학적 지식으로 방향성을 제시해 주셨던 서지원 교수님 감사합니다. 교수님께서 해주셨던 조언들 덕분에 연구 적 시야를 넓힐 수 있었고, 앞으로도 말씀 기억하면서 더욱 발전하도록 하겠습니다. 바쁘신 와중에도 좋은 디스커션과 연구방향, 그리고 조언들을 해주신 한정우 교수님께 감사드립니다. 교수님께서 제시해준 방향성 덕분에 제 연구분야에 있어서 더욱 깊은 이해를 할 수 있었고, 더욱 좋은 연구자가 될 수 있도록 최선을 다하겠습니다.

제 학위 과정 기간 동안 다양한 추억과 힘이 되어준 남기태 교수님 연구실 선배들, 동기, 그리고 후배들 모두에게 큰 감사를 드리고 싶습니다. 덕분에 소중한 추억과 많은 배움 얻을 수 있었습니다.

먼저, 아무것도 모르던 신입생 시절의 저에게 기본적인 실험부터 생각하는 방법, 논리적으로 자신의 생각을 전달할 수 있는 방법을 알려주신 찬우형에게 감사드립니다. 늘 유쾌하고 재미있게 말씀하셨지만, 많이 답답하셨을 텐데 화 한번 내지 않으시고 많은 것들 알려주셔서 감사합니다. 또한, 제가 처음 골드팀으로 가서 모르는 것이 많을 때, 아낌없는 가르침과 세심한 지도, 그리고 큰 버팀목이 되어 주셨던 혜은 누나와 효용이 형에게 감사드립니다. 정말 제가 도움을 받은 것 밖에 기억나지 않아서 늘 죄송스럽고 누나 와 형 덕분에 이런 훌륭한 주제로 연구하고, 졸업할 수 있음에 깊은 감사의 말씀 드립니다. 세분의 훌륭하신 선배님과 함께 일하고 배울 수 있어서 영광이었고, 앞으로 하시는 모든 일들 모두 다 잘 되셨으면 좋겠습니다.

저희 연구실 분들 한 분 한 분 에게 모두 감사의 말씀 드리고 싶습니다. 모범적인 자세로 늘 귀감과 길잡이가 되어준 승학이, 저와 같이 졸업하

시고 방장으로 오랫동안 수고해 주신 홍민이형, Dr. Bala who has always been kind to me and gave precious research advice, 늘 연구실 사람들을 즐겁게 해주고 적극적으로 도와주신 정석이형, 늘 즐겁게 연구하고 디스커션 임해주는 정도, 같이 축구도 하고 맛집 리스트도 공유하던 많은 추억 안겨준 강희, 연구 적으로 핵심적인 질문을 많이 하고 디스커션을 잘해주던 승우, 모든지 잘하고 동생이지만 배울 점이 많았던 남자다운 현진이, 꾸준히 열심히 그리고 누구보다 즐겁게 연구실 생활하는 정은이, 착하고 열심히 하는 미국에서 잊지 못할 추억 남겨준 중석이 친구 윤호, 항상 형들 잘 챙겨주고 같이 있으면 즐거운 내 기준 세상에서 가장 웃긴 무영이, 늘 위트 있고 재치 있던 똑똑한 옥현이, 조용하지만 열심히 연구실 생활 하는 원일이, 늘 늦게까지 일하면서 항상 밝게 웃고 열심히 하는 창완이, 항상 밝고 즐겁게 많은 일들 해내는 긍정적인 규민이, 너무 열심히 하고 잘하고있는 앞날이 기대되는 영인이, 여기서 언급 드리지는 못했지만 제가 진심으로 감사함을 느끼고 있는 이전 연구실 선배님 후배님들 모두에게 감사의 마음을 전합니다. 앞으로 더 멋진 연구를 통해서 세계 최고 연구자가 되기를 기원합니다.

부족한 팀장 임에도, 늘 저를 아껴주시고 도와주었던 골드팀 멤버들에게 진심으로 감사드립니다. 후배이지만 싹싹하지 못했던 저를 다 받아주시고 졸업할 때 엄청난 집념과 끈기를 보여준 운영 누나 감사합니다. 연구에 많은 도움 주시고, 힘이 되는 말씀 해주신 이종우 박사님 감사합니다. 항상 밝은 모습으로 연구실 생활을 즐겁게 해준 남궁석 박사님, 디스커션 할 때마다 연구 적으로 많은 점 배울 수 있었고, 사적으로도 편하게 대해줘서 너무 감사했습니다. 늘 학문적인 자세와 박학다식함으로 사람들을 놀라게 하고, 과격한 한 언행 속에서 가끔씩 나오는 따듯한 말로 사람들을 감동시키는 상원아, 덕분에 연구실 생활 즐거웠고 연구적으로

도 많이 성장할 수 있었어, 감사합니다. 조용한 듯 하지만 한마디 한마디가 재미있고 힘든 박사과정동안 나에게 많은 힘이 되어준 혜은아, 덕분에 독일 출장도 무사히 다녀올 수 있었고, 어려운 일들도 극복 할 수 있었어, 진심으로 고마워. 지금도 너무 훌륭히 잘 하고 있고, 앞으로도 하고자 하는 일 모두 잘 될 것이라 생각해, 늘 고맙고 진심으로 응원 할게. 후배이지만 늘 놀랍도록 많은 실험 양과 일들을 처리하는 존경스러운 금손 령명아, 너가 실험하고 연구하는 거 보며 많이 자극도 되고 나도 배울 수 있었어. 늘 도움만 받아서 고맙고 미안하고, 떡볶이랑 죽은 이제 그만 좀 먹고 건강 잘 챙겼으면 좋겠고, 하는 일 다 잘 났으면 좋겠어. 항상 밝고 주변 사람들을 기분 좋게 하는 다혜야, 늘 건강했으면 좋겠고 내가 너무 자주 놀려서 미안해. 힘든 시기였을 석사 졸업 이랑 취업 당당하게 하는 거 보면 멋있고, 꼭 그냥님 이랑 결혼하길 기원 할게. 엉뚱하지만 누구보다 똑똑한 예찬아, 어려운 공식들을 당연하 다는 듯 이해하는 널 보면 신기하기도 하고, 멋있기도 한 것 같아. 어떤 문제 이던 다 해결하는 것처럼 앞으로 다가올 많은 일들 다 잘 해치우고 남은 학기 잘 마무리 하고 그 이후 목표들도 다 잘 될 것이라 생각해, 응원 할게. 항상 밝고 열심히 하는 정원아, 1년동안 나랑 일하면서 많이 힘들었을 텐데 정말 고마워. 늘 내가 도움만 받고 많은 도움 못 준거 같아서 미안하고, 누구보다도 잘하고 있고 빠르게 성장하고 있는 거 같아. 정말 고맙고 앞으로 더 도움이 되는 선배 될 수 있도록 노력 할게. 목표 하는 일들 다 이루면 좋겠어. 들어 온지 얼마 안됐지만 빠르게 적응하고 있는 성호야, 늘 밝은 자세로 연구실에 잘 적응해주고, 열심히 하는 모습 고마워. 그리고, 인턴 하며 많이 힘들었을 기현아, 너와 함께 연구할 수 있어서 즐거웠고 꼭 훌륭한 연구자가 될 것 같아. 그리고 이제 곧 입학 할 정현아, 실험 척척 잘해 내는 거 보면, 앞으로도 잘 할 거라 생각하고, 들어와서 더 많은 추억 쌓을 수 있으면 좋겠어. 지난 시간들을 즐거

운 추억으로 채워주었던 골드팀 식구들에게 진심으로 감사드리며, 모두들 원하시는 바를 이루기를 기원합니다.

저의 입학 때부터 함께했던 소중한 동기들 모두 감사드립니다. 늘 밝고 씩씩한 모습으로 오빠들을 이끌어 주었던 미송이, 잘생기고 착하지만 허당미 넘쳤던 강규, 가까운 서울대에 있지만 단 한번도 연락하지 않는 내가 많이 아끼는 탁래, 늘 귀엽고 춤을 사랑했던 중현이 모두 저에게 소중한 추억 만들어주고 성장할 수 있도록 도움을 줘서 고맙습니다. 그리고 박사과정동안 누구보다도 큰 힘이 되어주고 내가 아는 사람 중 가장 똑똑한 어디 내어봐도 부끄러운 준호, 늘 장난스럽게 말하지만 너랑 함께 박사과정 해서 너무 즐거웠고, 너무 감사했고, 앞으로도 좋은 친구로 남으면 좋을 것 같아.

비록 지면에서는 언급하지는 못했지만 제 삶에 늘 힘이 되어 주시고 힘든 순간에 함께해준 친구들, 가족들, 그리고 다른 모든 분들에게 감사의 말씀을 전하고 항상 행복하기를 기원합니다.

무엇보다도 항상 저의 곁에서 응원해 주시고 저를 아껴주신 우리 부모님 감사하고 사랑합니다. 긴 시간 동안 아낌없이 지원해 주시고, 믿어주시고, 응원해주셔서, 부모님의 사랑 없이는 이 긴 학위과정을 마치지 못했을 것입니다. 훌륭한 사람이 되어 꼭 은혜에 보답하겠습니다. 어릴 때 저를 키워주시고 항상 함께해주신 우리 할머니, 너무 감사드리고 늘 건강하셨으면 좋겠습니다. 맨날 버릇없이 말하고 까부는 동생한테 한없이 착하기만 했던 남재형, 그리고 늘 형 편에서 응원해주시는 항상 감사한 형수님, 모두 곁에 있어줘서 고맙고 항상 건강하고 행복하기를 바랍니다.

2021년 2월

조 남 현